UNIVERSITÉ DU QUÉBEC À TROIS-RIVIÈRES

ÉTUDE DES PROPRIÉTÉS D'HYDROGÉNATION DE L'ALLIAGE $Ti_{0.488}Fe_{0.460}Mn_{0.052}$ PRODUIT PAR ATOMISATION

STUDY OF THE HYDROGENATION PROPERTIES OF $Ti_{0.488}Fe_{0.460}Mn_{0.052}$ ALLOY PRODUCED BY ATOMIZATION

THÈSE PRÉSENTÉE
COMME EXIGENCE PARTIELLE DU
DOCTORAT EN SCIENCES DE L'ÉNERGIE ET DES MATÉRIAUX

PAR
SEYEDEH FARANAK HOSSEINI GOURAJOUBI

MARS 2026

UNIVERSITÉ DU QUÉBEC À TROIS-RIVIÈRES

DOCTORAT EN SCIENCES DE L'ÉNERGIE ET DES MATÉRIAUX (PH. D.)

Direction de recherche :

Ph.D. Jacques Huot	Directeur de recherche

Jury d'évaluation de la thèse :

Ph.D. Jacques Huot	Directeur de recherche
Nom du codirecteur de recherche	Codirecteur de recherche
Ph.D. Pierre Bénard	Président de jury
Ph.D. Jean-Louis Bobet	Évaluateur externe
Ph.D. Ricardo Floriano	Évaluateur externe

Thèse soutenue le 11 mars 2026

To Hanna and Lena,

My two little lights who illuminate even my darkest days.

May you grow knowing that your mother never stopped dreaming, learning, and loving you beyond words.

ACKNOWLEDGEMENTS

First and foremost, I would like to express my deepest gratitude to my dear supervisor, Professor Jacques Huot. I will be forever grateful for your kindness, support, and understanding. When I began my PhD, I was going through one of the most challenging times in my life. You understood my situation and allowed me to start slowly. Whenever I faced challenges, your encouragement and hopeful words gave me the strength to persevere. Being your student will always remain one of the greatest honours of my life.

I would also like to thank Dr. Sakine (Elham) Khajavi, who has now become a dear friend. You have played an important role in my academic journey. Your encouragement and motivation always helped me move forward with strength.

I feel blessed to have had such wonderful friends in the lab – Babak, Seifeddine, Molood, Sedigheh, Sibriyana, Priyanka, Daniela, Francia, Salma, Chourouk, Mona, Tanin, Ignacio, Ali, and many others. Thank you for all the beautiful memories we shared. Even sharing a simple cup of tea or coffee, going out for lunch, or celebrating someone's birthday made my days brighter.

My beloved husband, Firooz, thank you for always being by my side. Your presence and unwavering support gave me strength, and this journey would have been unimaginable without you. My precious daughters, Hanna and Lena, I love you. You are the greatest joy and priority of my life.

My dear father, Seyed Fereidoon, who always asked about my work and was my source of strength, and my kind and beautiful mother, Ziba, whose prayers and positive energy have always surrounded me. I love you both so much, and I am proud to be your daughter. My sisters, Neda and Niayesh, I am deeply grateful to you. Although we are far apart, I always knew that just hearing your voices would always calm my heart. Your love has always reminded me of home and safety.

Finally, I would like to thank my dear friends, Neda, Mahsa, Parisa, Nazi, Arefeh, Masoumeh, Nafiseh, Mina, Zeinab, Anne-Mari, Farnaz, Saeed, Reyhaneh, and Samira. Although we are not in the same field, your presence in my life has been invaluable. I am truly grateful to have you all.

RÉSUMÉ

Cette recherche a été réalisée en collaboration avec le GKN Hoeganaes Innovation Centre & Advanced Materials et porte sur l'amélioration du comportement lors de la première hydrogénation de l'alliage $Ti_{0.488}Fe_{0.460}Mn_{0.052}$. L'alliage a été produit par GKN en utilisant la technique d'atomisation gazeuse. Les alliages de type TiFe sont connus pour présenter une première hydrogénation lente en raison de la présence d'oxydes de surface. Dans cette étude, l'atomisation gazeuse a été choisie par notre partenaire industriel afin d'obtenir une microstructure fine. Les vitesses de refroidissement rapides associées à ce procédé conduisant généralement à une microstructure favorable à l'absorption d'hydrogène. L'analyse microstructurale a révélé une microstructure biphasée composée d'une matrice TiFe et de phases secondaires filamenteuses. L'analyse EDS a montré que la composition de la matrice correspond à TiFe et que celle de la phase secondaire est proche de Ti_2Fe.

En plus de l'alliage tel qu'atomisé, un échantillon recuit sous vide, ayant subi un traitement thermique à 1120 °C pendant 1 h après l'atomisation gazeuse, a également été étudié. Après le traitement thermique, la composition chimique s'est rapprochée de la composition nominale et la morphologie de la phase secondaire est passée de filamenteuse à globulaire. L'analyse de la structure cristalline a montré que le recuit augmentait la taille des cristallites de la phase TiFe et réduisait sa microdéformation.

Les échantillons atomisés (AS) et recuits sous vide (VA) ont été soumis à une hydrogénation dans deux conditions : à température ambiante sous 2000 kPa d'hydrogène, et à 90 °C sous 4500 kPa d'hydrogène. Pour les deux échantillons, aucune absorption d'hydrogène n'a été enregistrée dans ces conditions après 24 h, probablement en raison d'une longue exposition à l'air avant l'hydrogénation. Par conséquent, des méthodes d'activation mécanique ont été employées. Après 5

passes de laminage à froid, l'échantillon atomisé a absorbé 1,56 % en masse d'hydrogène à température ambiante et sous 2000 kPa. En revanche, l'échantillon recuit n'a pas pu être activé après 24 h dans les mêmes conditions. Les deux échantillons ont absorbé de l'hydrogène à 90 °C et 4500 kPa. Toutefois, l'échantillon atomisé a présenté une cinétique plus rapide et une capacité plus élevée. Ces résultats indiquent que le recuit après atomisation a un effet néfaste sur le processus d'hydrogénation, probablement en raison de la recristallisation et des modifications microstructurales associées.

Par la suite, différents traitements mécaniques, laminage à froid (5 passes), broyage à billes (10 minutes) et compactage à froid, ont été comparés afin d'étudier leur influence sur le comportement d'hydrogénation de l'alliage atomisé. L'analyse MEB a montré que le laminage à froid et le broyage à billes réduisaient la taille moyenne des particules, produisant des particules fragmentées avec des fissures visibles. Le compactage à froid, en revanche, n'a pas modifié la distribution granulométrique, mais de nombreuses fissures ont été observées sur la surface des particules.

L'affinement Rietveld des diagrammes XRD a montré que les paramètres de maille restaient presque constants pour tous les échantillons. Cependant, le traitement mécanique réduisait la taille des cristallites et augmentait la microdéformation. Parmi les échantillons traités, la poudre broyée présentait la plus petite taille de cristallite et la plus forte microdéformation, tandis que l'échantillon compacté conservait la plus grande taille de cristallite et la plus faible microdéformation.

Le comportement d'absorption de l'hydrogène a été étudié à température ambiante et sous 2000 kPa d'hydrogène. Tous les échantillons ayant subi un traitement mécanique ont absorbé de l'hydrogène. Le compactage à froid a donné la plus grande capacité d'absorption, tandis que l'échantillon broyé a présenté la cinétique la plus rapide, ce qui a été attribué à la plus petite taille de cristallite et,

par conséquent, à la plus forte densité de joints de grains, facilitant la diffusion de l'hydrogène.

Enfin, l'énergie d'activation de la première hydrogénation a été mesurée. L'influence de la température, de la force motrice constante et de la pression d'hydrogène sur la première activation ont été évaluées. Les résultats ont indiqué que la première hydrogénation suit un comportement de type Arrhenius ($k = Ae^{-\frac{E_A}{RT}}$), et que l'énergie d'activation moyenne a été calculée à 71 kJ/mol H_2. Le facteur préexponentiel (A) s'est révélé dépendant de la pression, suivant l'équation $A = A_0 (P/P_0)^{1.8}$, où $A_0 = 2.6 \times 10^6\ s^{-1}$.

Mots-clés: Hydrure métallique, Alliages TiFe, Première hydrogénation, Traitement mécanique, Énergie d'activation.

Seyedehfaranak Hosseinigourajoubi Jacques Huot

ABSTRACT

This research was carried out in collaboration with GKN Hoeganaes Innovation Centre & Advanced Materials and focuses on improving the first hydrogenation behaviour of the $Ti_{0.488}Fe_{0.460}Mn_{0.052}$ alloy. The alloy was produced by gas atomization by GKN. TiFe alloys are known to exhibit sluggish first hydrogenation due to the presence of surface oxides. In this work, gas atomization was chosen by our industrial partner to obtain a fine microstructure, as the rapid cooling rates associated with the process typically yield a fine microstructure favourable for hydrogen absorption. Microstructural analysis revealed a two-phase microstructure consisting of a TiFe matrix and filamentous secondary phases. EDS analysis showed that the composition of the matrix is TiFe and the secondary phase composition is close to Ti_2Fe.

In addition to the as-atomized alloy, a vacuum-annealed sample, which was heat-treated at 1120 °C for 1 h after gas atomization, was also investigated. After heat treatment, the chemical composition was closer to the nominal composition, and the secondary phase morphology changed from filamentous to globular. Crystal structure analysis further revealed that annealing increased the crystallite size of the TiFe phase and reduced its microstrain.

Both as atomized (AS) and vacuum annealed (VA) samples were subjected to hydrogenation under two different conditions: at room temperature and 2000 kPa of hydrogen pressure, and at 90°C under 4500 kPa of hydrogen pressure. For both AS and VA samples, no hydrogen uptake was registered under these conditions for 24 hours, probably due to long air exposure before hydrogenation. Therefore, mechanical activation methods were employed. After 5 passes of cold rolling, the atomized sample absorbed 1.56 wt.% hydrogen at room temperature and 2000 kPa hydrogen pressure. In contrast, the annealed sample could not be activated within 24 hours under the same conditions. Both the atomized and

annealed samples absorbed hydrogen at 90 °C and 4500 kPa; however, the atomized sample exhibited faster kinetics and a higher capacity. These results indicate that annealing after atomization has a detrimental effect on the activation process, likely due to recrystallization and associated microstructural changes.

Subsequently, the different mechanical treatments, such as cold rolling (5 passes), ball milling (10 minutes), and cold pressing, were compared to investigate their effects on the hydrogenation behaviour of gas atomized alloy. SEM analysis revealed that cold rolling and ball milling reduced the average particle size, producing fragmented particles with visible cracks. Cold pressing, in contrast, did not alter the particle size distribution, but numerous cracks were observed on the particle surfaces.

Rietveld refinement of the XRD patterns showed that the lattice parameters remained nearly constant across all samples. However, mechanical processing reduced crystallite size and increased microstrain. Among the processed samples, the ball-milled powder had the smallest crystallite size and the highest microstrain, while the cold-pressed sample retained the largest crystallite size and the lowest microstrain.

Hydrogen absorption behaviour was studied at room temperature and 2000 kPa hydrogen pressure. All mechanically processed samples absorbed hydrogen. Cold pressing resulted in the highest hydrogen absorption capacity. The ball-milled sample showed the fastest kinetics, which was attributed to the smallest crystallite size and, consequently, the highest grain boundary density, which facilitates hydrogen diffusion.

Finally, the activation energy of both the incubation time and the first hydrogenation was measured. The influences of temperature, constant driving force, and hydrogen pressure on the first activation were evaluated. The results indicated that the first hydrogenation follows an Arrhenius behavior ($k = Ae^{-\frac{E_A}{RT}}$),

and average activation energy was calculated as 71 kJ/mol H_2. The pre-exponential factor (A) was found to be pressure-dependent, following the equation $A = A_0 (P/P_0)^{1.8}$, where $A_0 = 2.6 \times 10^6\ s^{-1}$.

Keywords: Metal Hydride, TiFe Alloys, First Hydrogenation, Mechanical Processing, Activation Energy.

TABLE DES MATIÈRES

LISTE DES TABLEAUX

LISTE DES FIGURES

CHAPTER I.

INTRODUCTION

1.1 Hydrogen and the Future of Energy Sustainability

As global energy demands continue to rise, there is an increasing urgency to find sustainable, clean, and efficient energy sources [1]. Among the various alternatives, hydrogen has attracted significant attention as an energy vector because of its versatility, abundance, and potential for zero greenhouse gas emissions during usage [2].

Hydrogen can be produced through various methods, such as solar, wind, hydropower, and nuclear sources [3]. Its clean combustion properties make it a better alternative to fossil fuels, particularly in transportation and industry [4]. However, utilizing hydrogen effectively requires efficient storage solutions. Due to its low density and high diffusivity, hydrogen storage presents unique challenges that must be addressed to enable widespread use [5].

1.2 Hydrogen Storage

Hydrogen storage is a critical aspect of hydrogen technology. There are three primary methods for hydrogen storage: gaseous, liquid, and solid-state storage. Each of these methods has distinct characteristics, advantages, and challenges [6].

1.2.1 Gaseous Hydrogen Storage

Gaseous hydrogen is typically stored under high pressure, often in the range of 350-700 bars. However, this storage method presents several challenges. The tanks must be made of materials capable of withstanding extreme pressures, which increases cost and adds weight [7]. Additionally, gaseous hydrogen storage suffers from low volumetric energy density, meaning that large tanks are required to store sufficient amounts of hydrogen for practical applications. Leakage and safety concerns due to the high flammability of hydrogen are also notable disadvantages [8].

1.2.2 Liquid Hydrogen Storage

Storing hydrogen in liquid form involves cooling it to cryogenic temperatures (-253°C) and maintaining these conditions in specialized insulated tanks. Liquid hydrogen offers higher energy density compared to gaseous storage and can be used in applications requiring compact storage solutions, such as in aerospace. However, the liquefaction process is highly energy-intensive, consuming nearly 30-40% of the stored hydrogen's energy content. Furthermore, the requirement for expensive cryogenic equipment makes this method less efficient and economically viable for widespread adoption [9].

1.2.3 Solid-State Hydrogen Storage

Solid-state hydrogen storage has emerged as a promising alternative to overcome the limitations of gaseous and liquid storage. This method involves storing hydrogen in solid materials, such as metal hydrides, complex hydrides, or porous materials [10]. The primary advantage of solid-state storage is its safety and high volumetric energy density. However, solid-state hydrogen storage presents several challenges. The development of suitable materials that offer high storage capacity, rapid kinetics, and long-term stability remains a key area of research [11].

Solid-state hydrogen storage can be broadly classified into two mechanisms: adsorption and absorption [12]. In the adsorption mechanism, hydrogen molecules adhere to the surface of porous materials through weak van der Waals forces. Materials such as carbon nanotubes, zeolites, and metal-organic frameworks (MOFs) with high specific surface areas are commonly used for adsorption-based storage. This method is advantageous due to its reversibility and the ability to operate at relatively low pressures. However, adsorption-based storage often requires cryogenic temperatures to achieve significant hydrogen uptake. Additionally, the storage capacity of adsorption is limited by the material's specific surface area and pore size distribution, necessitating the development of advanced materials to enhance efficiency [13,14].

In contrast to adsorption, absorption involves the incorporation of hydrogen into the bulk structure of a material through chemical bonding. A schematic representation of hydrogen absorption is shown in Figure 1.1. Initially, H_2 molecules interact with the surface via Van der Waals forces and are physically adsorbed on the surface. Next, H_2 molecules dissociate into individual hydrogen atoms. The dissociated hydrogen atoms then diffuse into the material, occupying random interstitial sites. Eventually, these hydrogen atoms form metallic, covalent, or ionic bonds with the host metal, leading to the formation of a hydride compound. These materials offer high volumetric hydrogen density and provide safe storage solutions. The challenge with absorption-based storage lies in the kinetics of hydrogen uptake and release, as well as the thermodynamic properties that dictate the operational temperature and pressure ranges [10,15,16].

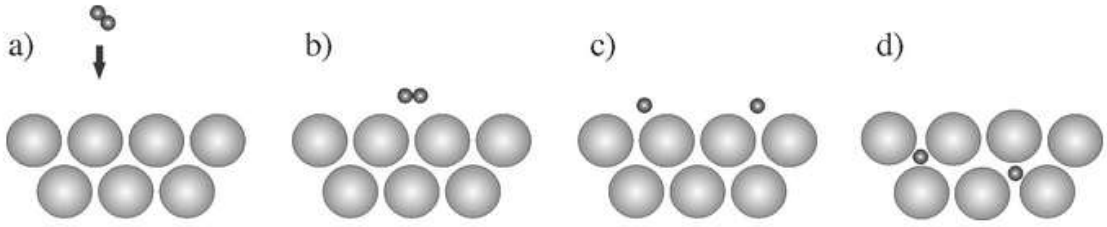

Figure 1.1 Schematic representation of the hydrogen absorption [16,17].

1.3 Metal Hydrides

Metal hydrides have garnered significant attention in the field of solid hydrogen storage due to their ability to reversibly absorb and desorb hydrogen under moderate conditions. These materials form metal-hydrogen bonds during the absorption process, creating stable hydrides that can store hydrogen with high volumetric density. There are two classes of hydrides: metallic hydrides and complex hydrides based on their composition and bonding characteristics [17]. Metallic hydrides are typically formed by transition or alkaline earth metals and exhibit metallic bonding, where hydrogen atoms are incorporated into the metal lattice, creating solid solutions or intermetallic compounds [18]. The bonding in these materials is relatively weak compared to covalent or ionic bonds, which allows for reversible hydrogen absorption and release under moderate conditions [19]. In contrast, complex hydrides consist of a metal combined with hydride anions and exhibit ionic or covalent bonding. Complex hydrides tend to offer higher gravimetric hydrogen density but face challenges such as poor reversibility and high dehydrogenation temperatures [20].

Several classes of intermetallic compounds have been identified as promising candidates for hydrogen storage. These materials are classified based on their stoichiometry and crystal structures, which influence their hydrogen storage properties [21].

AB-type Hydrides: These compounds, such as TiFe, are among the most studied materials for hydrogen storage. Usually, they contain a transition metal (A) that forms stable metal hydrides like Ti, Zr and Mg, and another element (B) which interacts more weakly with hydrogen, such as Fe, Ni, and Mn. AB-type hydrides exhibit good reversibility and moderate operating conditions; however, the first hydrogenation, also called activation, can be challenging due to surface oxidation. TiFe-based hydrides require initial activation, often achieved by repeated hydrogenation/dehydrogenation cycles. Alloying elements like Mn or Co can enhance activation properties and kinetics by reducing oxidation susceptibility and modifying thermodynamics [21,22].

AB_5-type Hydrides: Represented by materials such as $LaNi_5$, AB_5 compounds are widely used in rechargeable NiMH batteries. Usually, A is a hydride-forming element, and B is a non-hydride-forming element. These materials demonstrate excellent hydrogen absorption kinetics and cycling stability but have limited hydrogen capacity [21-23].

AB_2-type Hydrides: Examples include Zr-based compounds (e.g., $ZrMn_2$, ZrV_2). These materials offer higher hydrogen storage capacities than AB_5 but typically exhibit higher activation energies for hydrogen absorption or desorption [21,22].

A_2B-type Hydrides: This category includes Mg_2Ni and related compounds. They possess high hydrogen capacities but suffer from high desorption temperatures and slow kinetics [21,22].

1.4 Thermodynamic of Hydrogen Absorption

The kinetics and thermodynamics of metal hydride formation determine hydrogen storage performance, rate of absorption/desorption, and operational feasibility. Generally, the hydrogenation reaction is described by the following equation:

$$M + \frac{x}{2} H_2 \Leftrightarrow MH_x + Q, \tag{1.1}$$

Where M is the metal element and Q is the reaction heat.

The process of hydrogen absorption in metal hydrides is represented by the pressure-composition temperature (PCT) and its associated Van't Hoff equation. Figure 1.2 shows a schematic of PCT curve illustrating the different stages of hydrogen uptake within a metal or alloy.

At low hydrogen pressures, hydrogen atoms dissolve into the metallic host, forming a solid solution known as the α-phase. This process occurs gradually as pressure increases, with hydrogen atoms occupying interstitial sites in the metal lattice. With further hydrogen

intake, the system reaches a critical point where the nucleation of a new hydride phase (β-phase) starts. The coexistence of α and β phases gives rise to a plateau region in the PCT curve, where hydrogen is stored at almost constant pressure while the fraction of the β-phase increases. The plateau pressure shows the stability of the hydride. Lower equilibrium pressures indicate more stable hydrides, while higher pressures indicate weaker metal-hydrogen bonding, facilitating hydrogen desorption at lower temperatures. The width of the plateau shows how much hydrogen can be stored and released reversibly. At the end of the plateau, the α-phase fully transforms into the β-phase. For concentrations above this, further hydrogen uptake corresponds to solid solution of hydrogen in the β-phase [7,24,25].

The Gibbs phase rule helps describe the phase behavior of metal hydrides during hydrogen absorption and desorption. It states that the number of independent variables (degrees of freedom, F) in a system is given by:

$$F = C - P + 2, \tag{1.2}$$

where C is the number of chemical components, and P is the number of coexisting phases in equilibrium. In the case of hydrogen absorption, the system consists of two components: the metal and hydrogen (C = 2). On the plateau region of the pressure-composition isotherm, three phases coexist—the α-phase (solid solution), the β-phase (metal hydride), and hydrogen gas, so P = 3. This results in F = 1, meaning that with the change of the composition (C), the equilibrium pressure doesn't change [26,27].

At the end of the plateau, when the entire material has transformed into the β-phase, the number of phases decreases to two (P = 2), increasing the degrees of freedom to F = 2, and hydrogen concentration increases with hydrogen pressure.

The relationship between equilibrium pressure and temperature in the plateau region is explained by the Van't Hoff equation:

$$\ln\left(\frac{P_{eq}}{P_0}\right) = \frac{\Delta H}{RT} - \frac{\Delta S}{R}, \tag{1.3}$$

where Peq is the equilibrium pressure, P_0 is the standard atmosphere pressure (100 kPa), R is the gas constant, and ΔH and ΔS are respectively the enthalpy and the entropy of metal hydride formation reaction. The Van't Hoff plot (Figure 1.2), which represents ln P_{eq}/P_0 as a function of 1/T, provides valuable insight into the thermodynamic stability of the hydride. The slope of this plot yields ΔH, while the intercept corresponds to ΔS [28].

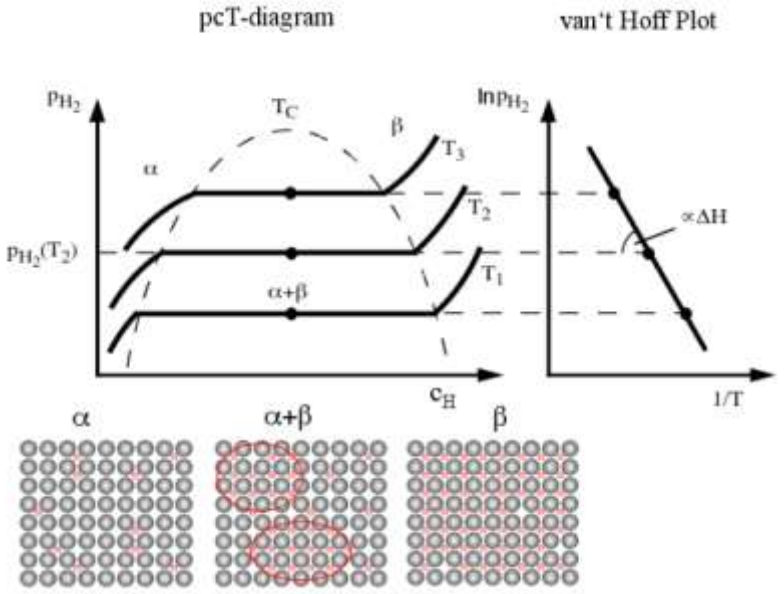

Figure 1.2 Schematic pressure-composition temperatures (PCTs) at different temperatures and Van't Hoff correlation [29].

1.5 Hydrogen Storage of TiFe Alloys

TiFe-based intermetallic compounds are among the most studied materials for hydrogen storage due to their cost-effectiveness, abundance of raw materials, and moderate operating conditions. The hydrogen absorption capacity of TiFe alloy is 1.86 wt.% at low pressure at room temperature [29]. During hydrogenation, TiFe forms TiFeH and $TiFeH_2$ hydrides [30]. However, the first hydrogenation or activation of FeTi is usually slow at room temperature due to FeTi being highly sensitive to air and a passivation layer formed on the surface that acts as a barrier to hydrogen diffusion [31,32]. Typically, thermal

activation is required to facilitate hydrogen absorption and enhance its kinetics. These activation treatments involve cycling between high temperature and room temperature under high hydrogen pressure. In the pioneering work of Reilly and Wiswall, the first hydrogenation was preceded by heating the alloy to over 400°C for 30 minutes, either in a vacuum or at low hydrogen pressure, then cooling it to room temperature and applying a high hydrogen pressure of approximately 6000 kPa. This process induces thermal stresses due to the difference in thermal expansion between the oxide layer and the TiFe substrate, leading to the formation of cracks that expose fresh TiFe surfaces to hydrogen. Additionally, the volume expansion associated with hydride formation generates further microcracks, which facilitate hydrogen diffusion into the bulk. The process had to be repeated several times until the hydrogenation occurred in about 15 minutes [33]. Since then, several studies have used this type of thermal activation procedure for TiFe alloys [34-36]. However, these processes are time-consuming and increase the operational costs.

To overcome the need for high-temperature and high-pressure conditions required for the first activation, mechanical processing techniques such as cold rolling, ball milling, and high-pressure torsion have emerged as promising methods to enhance the activation behavior of TiFe alloys [37].

Ball milling is a mechanical processing technique that reduces particle size, creates new surfaces, and introduces defects and grain boundaries, all of which enhance hydrogen diffusion. Emami et al. demonstrated that ball milling could synthesize nanocrystalline TiFe compounds that could absorb 1.3–1.5 wt.% hydrogen without any extra activation process. This enhancement was attributed to the formation of nanograins and a high fraction of high-angle grain boundaries, which can serve as hydrogen trapping sites [38].

High-Pressure Torsion (HPT) is another severe plastic deformation method that involves the application of high pressure combined with torsion shear strain, leading to significant grain refinement and the generation of lattice defects. This process can activate TiFe, possibly due to the formation of defects and cracks that provide pathways for hydrogen diffusion through the oxide layer [19,39]. A study by Edalati et al. demonstrated

that nanostructured TiFe remains active even after prolonged air exposure, owing to surface segregation, the formation of Fe-rich regions that catalyze hydrogen dissociation, and the presence of numerous dislocations, grain boundaries, and microcracks that facilitate hydrogen transport from the surface to the bulk [40].

Cold Rolling is a mechanical deformation process that reduces the thickness of metal sheets at room temperature, resulting in significant work hardening, grain refinement, and the generation of dislocations. These structural changes enhance hydrogen absorption by providing diffusion pathways [41,42].

In addition to the above-mentioned mechanical treatment process, the activation issue can be overcome by the addition of transition elements such as Mn [43,44], Zr [45,46], Cr [47], V [48,49], and Y[50,51]. These additives cause the formation of second phases, which can generate microcracks in the material due to local expansion. At the same time, these second phases also produce new grain boundaries and interfaces, which act as pathways for hydrogen diffusion into the TiFe matrix [52-57].

Gosselin et al. investigated the first hydrogenation of TiFe with the addition of X wt.% Zr (X = 4, 8, 12, 16). Their findings revealed that TiFe with 8 wt.% Zr exhibited the fastest first hydrogenation kinetics. They attributed this to the presence of a second phase, which they suggested acts as a hydrogen diffusion gateway, thereby facilitating hydrogen absorption in the TiFe phase [58].

Patel et al. investigated the effect of Zr and Mn on the microstructure and the first hydrogenation kinetics of TiFe alloy. They concluded that the fastest kinetic and highest capacity was reached by doping with 2 wt.% Mn and 4 wt.% Zr. The enhanced activation kinetics was attributed to the presence of a large proportion of Ti_2Fe type phase, potentially because this phase could act as a gateway, facilitating hydrogen entry into the TiFe phase [59].

Lv et al. studied the effects of doping, cold rolling, and forging on the microstructure and hydrogen storage properties of air-exposed TiFe + x wt.% (Zr+2V) (x = 0, 4, 5, and 6) alloys. They concluded that doping with (Zr+2V) significantly improved the first hydrogenation kinetics of TiFe due to the formation of an hcp secondary phase, which can enhance the diffusion of hydrogen. Forging effectively reduced the incubation time and enhanced the first hydrogenation kinetics, while cold rolling improved absorption kinetics but resulted in lower hydrogen capacity [46].

Guéguen et al. studied the influence of the addition of small amounts of vanadium on the hydrogenation properties of $TiFe_{0.9}V_x$ and $TiFe_{0.8}Mn_{0.1}V_x$ (x=0, 0.05, and 0.1) alloys synthesized using induction melting. The absorption kinetics of vanadium-containing samples was improved. In addition, the absorption capacity increases as a function of vanadium content since the affinity of vanadium for hydrogen is higher than that of iron; partial substitution of iron by vanadium increased the absorption capacity [49].

It is also worth mentioning that some studies have suggested that a finer microstructure can improve hydrogenation behavior [52,60-63]. For example, Patel et al. studied the effect of cooling rate on the microstructure of TiFe + 4 wt.% Zr by casting the alloy in a step mold with varying thicknesses. They found that faster cooling rates led to a finer dispersion of the secondary phase, which positively impacted the activation kinetics [63]. Similarly, Ulate-Kolitsky et al. compared TiFe-based alloys produced by gas atomization and induction melting. Their results indicated that gas atomization, due to its rapid solidification process, produced a much finer microstructure and a more uniform distribution of secondary phases within the TiFe matrix, leading to improved activation behavior [42]. These findings suggest that the choice of synthesis method plays a crucial role in determining the hydrogenation properties of TiFe alloys. Gas atomization method typically has a rapid cooling rate and can be considered a method that produces fine metallic powder with refined microstructure. However, in addition to microstructural effects, the surface condition of TiFe powders is also critical for hydrogen absorption. Due to their high specific surface area of atomized powders, more oxides layers form on the surface during air exposure. These oxide layers act as barriers to hydrogen diffusion.

1.6 Research Goals

This PhD project aims to address the challenges associated with the first hydrogen absorption of TiFe-based alloys. Although these materials are attractive for hydrogen storage applications due to their cost-effectiveness and suitable thermodynamic properties, their first hydrogenation remains difficult, due to surface oxidation.

To tackle this issue, the first step of this work is the synthesis of a $Ti_{48.8}Fe_{46.0}Mn_{5.2}$ alloy using the gas atomization method. This composition was selected by the company GKN because it is well known that partial substitution of Fe by Mn improves the hydrogen storage performances. Gas atomization was chosen as the processing method because it generally produces finer microstructures compared to conventional melting techniques such as arc melting, which may play a key role in improving activation behavior.

The overall objective of this work is to improve the first hydrogenation behavior of the produced alloy. Particular attention is given to understanding the relationship between microstructure, surface conditions, and hydrogen absorption behavior. In this context, the study examines how different mechanical activation treatments modify the material and facilitate hydrogen uptake. Furthermore, the role of annealing in altering the microstructure and its impact on hydrogen absorption is investigated.

In addition, the effects of temperature, hydrogen pressure, and constant driving force on the incubation time of the first hydrogenation are analyzed. The aim of this part of the study is to determine the activation energy of the first hydrogenation process and to provide insight into the underlying kinetic mechanisms.

1.7 Thesis Structure

This thesis consists of six chapters:

- **Chapter I** provides an introduction, emphasizing the importance of hydrogen energy as a sustainable solution, the advantages of solid-state hydrogen storage, and the role of metal hydrides, with a focus on TiFe-based alloys.
- **Chapter II** describes the experimental procedures, including sample preparation techniques and characterization methods.
- **Chapter III** discusses various mechanical activation methods used to improve the activation behavior of the $Ti_{48.8}Fe_{46.0}Mn_{5.2}$ alloy. This work was published in the Journal *hydrogen*.
- **Chapter IV** investigates the effect of annealing on the first hydrogenation behavior of the $Ti_{48.8}Fe_{46.0}Mn_{5.2}$ alloy. This work was published in the Journal *Metals*.
- **Chapter V** presents the influences of temperature, constant driving force, and hydrogen pressure on the first activation process. The corresponding results have been submitted to the journal *Materials*.
- **Chapter VI** concludes the thesis and outlines directions for future research.

CHAPTER II.

EXPERIMENTAL DETAILS

2.1 Materials

The primary objective of this study was to investigate the activation behavior of a $Ti_{48.8}Fe_{46.0}Mn_{5.2}$ alloy synthesized by gas atomization. The industrial partner, GKN Hoeganaes, carried out the gas atomization process. The nominal composition of the alloy is presented in Table 2.1.

Table 2.1 Nominal composition of FeTi-based alloy in at.%.

Melt #	C	O	N	Ti	Fe	Mn
CC - 168 Avg.	0.016	0.158	0.005	48.69	45.94	5.11

2.2 Synthesis Method

The alloy was produced by gas atomization which is one of the most common processes to produce metal powders that molten metal is dispersed into a high-velocity gas jet, such as air, argon, nitrogen, or helium. The principle of gas atomization is based on the gas-to-metal ratio to control particle size, which offers very fine control and low contamination. The process involves high-speed gas jets breaking molten metal into fine droplets that solidify quickly, resulting in spherical powders. This technique is especially valued in industries that require powders with fineness, reactivity, or low oxygen content, like additive manufacturing and powder metallurgy [64].

Gas atomization was performed by GKN Hoeganaes Innovation Center and Advanced Materials under pure argon with a VIGA-type furnace in a free-fall atomization ring configuration. Herein, the melting metal leaves the crucible and is promptly atomized by a circle of gas jets around the metal stream. This process design enables a homogeneous particle-size distribution and maximizes the degree of atomization. The powder obtained was subsequently kept in the air. A schematic of the gas atomization process, free-fall design, is shown in Figure 2.1 [65].

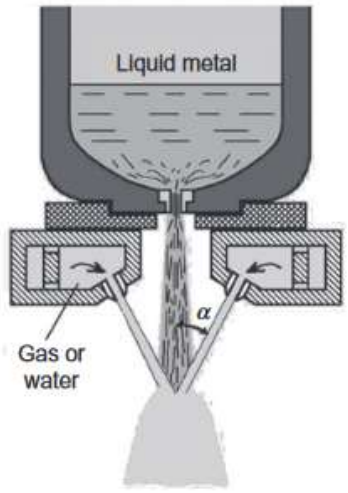

Figure 2.1 Free-fall atomizer designs (α: the angle created between the free-falling molten metal and the jet of the atomizing medium) [65].

2.3 Processing Methods

2.3.1 Annealing

Annealing is a heat treatment process in which the alloy is heated up to the appropriate temperature for a prescribed time, followed by a controlled cooling rate to achieve equilibrium microstructures. Depending upon the purpose, various annealing types are carried out at different temperatures. Annealing can influence the hydrogenation properties of metal hydrides considerably [66,67]. After gas atomization, a part of the

atomized powder was vacuum annealed at 1120°C for 1 h in a batch furnace. Annealing was performed by the industrial partner, GKN Hoeganaes.

2.3.2 Cold Rolling

Cold rolling is a metalworking process in which a metal material is passed through rollers to reduce thickness, enhance surface quality, and improve mechanical properties. Unlike hot rolling, cold rolling is performed at room temperature.

In this work, cold rolling was performed vertically in the air using a modified Durston DRM 130 rolling mill (High Wycombe, Buckinghamshire, UK). To avoid contamination from the rollers, the powder was inserted between two 316 stainless steel plates, as shown schematically in Figure 2.2. Samples were cold rolled for 5, 10, and 20 passes, shown as 5CR, 10CR, and 20CR, respectively. The roller used in this study is shown in Figure 2.3.

To investigate the effect of the cold rolling atmosphere, the process was conducted in an argon-filled glove box. The vertical cold rolling was performed using equipment from International Rolling Mills (Pawtucket, USA), as shown in Figure 2.4.

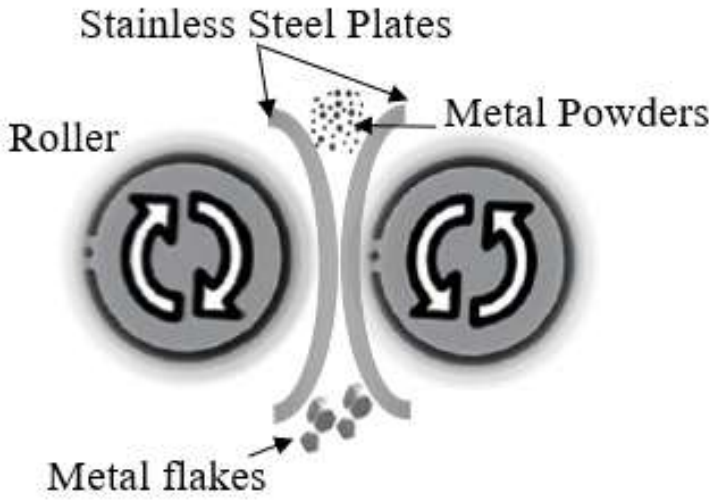

Figure 2.2 Schematic of the vertical cold rolling process.

Figure 2.3 Roller Durston DRM 130.

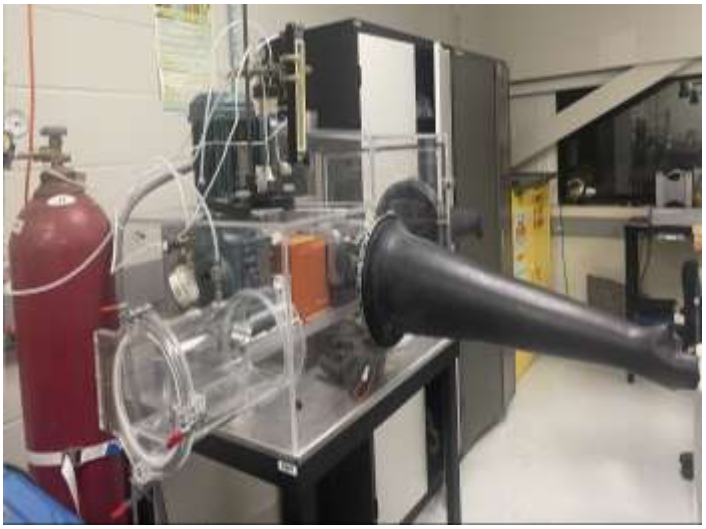

Figure 2.4 Cold rolling in argon setup.

2.3.3 Ball Milling

Ball milling is a mechanical process in which materials are ground and mixed using cylindrical containers filled with metal or ceramic balls. The container can either be shaken or rotated. The impact and friction between the balls and the material cause size reduction, mixing, and sometimes structural changes. This process enhances hydrogen absorption-desorption kinetics by reducing particle size, increasing specific surface area, and introducing defects [68].

In the present investigation, ball milling was performed using a SPEX 8000M high-energy ball mill from SPEX SamplePrep, Metuchen, NJ, USA. The milling was conducted in a 55 cm^3 stainless steel crucible with a powder-to-ball mass ratio of 1:10 for 10 minutes. All powder handling, including loading and unloading, took place inside an argon-filled glove box to prevent contamination. Figure 2.5 shows the ball milling machine used in this research.

Figure 2.5 Ball milling equipment.

2.3.4 Cold Pressing

Cold pressing is one of the most common material processing techniques and is widely used in the fabrication of powder metallurgy components. It involves applying high pressure to a material, typically metal or ceramic powders, at room temperature to form a compacted shape [69].

Cold pressing was carried out using a hydraulic press manufactured by Research & Industrial Instruments Company (London, England) shown in Figure 2.6. A die with a diameter of 14 mm was used to compact the powder under uniaxial pressure. The sample was subjected to a force of 12 tons for 2 minutes. After cold pressing, the obtained pellet was manually crushed into powder using a hardened steel mortar and pestle in the air. This crushing step was necessary to meet the size requirements of the sample holder for subsequent hydrogenation tests.

Figure 2.6 Cold press machine.

2.4 Characterization of Materials

The crystal structure of the alloys was analyzed by X-ray diffraction (XRD) measurement was carried out on a Bruker D8 Focus diffractometer (Madison, WI, USA) with CuKα radiation. The XRD patterns were analyzed by the Rietveld method using TOPAS software (Bruker, Madison, WI, USA) to determine the alloy's phase abundance, lattice parameter, and crystallite size [70].

The morphology and microstructure of the powder were analyzed using a Hitachi SU1510 scanning electron microscope (Hitachi High-Tech Canada, Inc., Toronto, ON, Canada) equipped with EDX – Energy-Dispersive X-ray spectrometer (Abingdon, UK).

The sample's hydrogen capacities and absorption kinetics were evaluated using a homemade Sievert-type apparatus. One gram of powder was placed in a sample holder and evacuated for 15 minutes before kinetic measurements. The measurements were conducted under various pressures ranging from 1500 kPa to 5000 kPa at temperatures of 298 K, 308 K, 318 K, and 328 K.

2.4.1 X-Ray Diffraction (XRD)

XRD is a non-destructive method used to analyze the crystallography of materials by observing how they interact with X-rays. It reveals essential details about the crystalline substance's phase composition, lattice parameters, and other structural characteristics. The underlying principle of XRD is governed by Bragg's Law, expressed as:

$$n\lambda = 2d\sin\theta, \tag{2.1}$$

where n is the order of reflection, λ is the wavelength of the X-rays, d is the interplanar spacing, and θ is the diffraction angle [71]. Figure 2.7 shows the schematic diagram of Bragg diffraction.

When X-rays interact with a crystal, they elastically scatter off the atoms in the lattice. Constructive interference occurs at particular angles (θ), producing diffracted rays. The instrument detects and counts these diffracted rays after processing. A resulting diffraction pattern specific to the material's crystal structure offers important information on lattice parameters, crystallite size, microstrain, and phase composition. Each material has a particular pattern of diffraction. These may be matched against standard reference databases, such as the International Powder Diffraction File (PDF), for phase identification of the material [72].

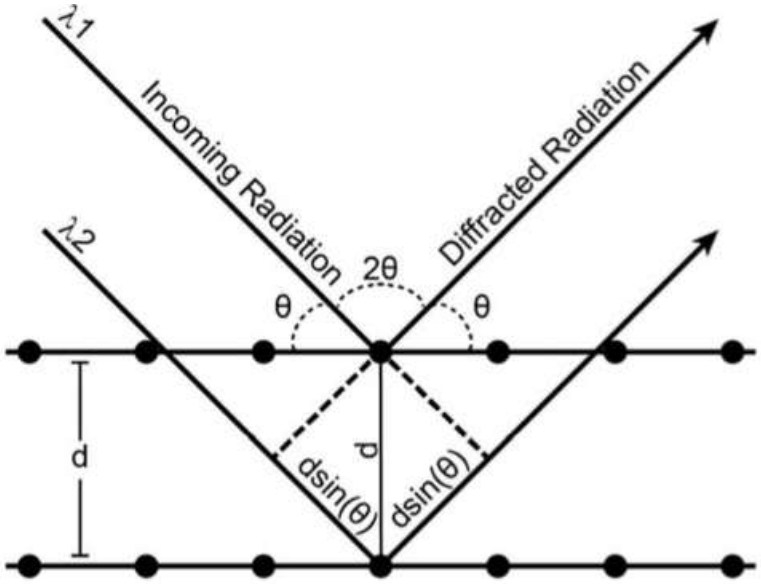

Figure 2.7 Schematic of Bragg diffraction of incident X-rays by parallel atomic planes [71].

XRD data were analyzed quantitatively using Rietveld refinement in the TOPAS software. In this method, the experimental diffraction pattern is compared with a calculated pattern generated from initial crystallographic information (such as approximate unit cell parameters, atomic positions, and space group) as well as instrumental parameters. These initial values serve only as starting points; the software then iteratively refines the structural parameters and phase fractions to obtain quantities such as crystallite size, microstrain, and lattice parameters [73].

2.4.2 Scanning Electron Microscopy (SEM)

Scanning Electron Microscopy (SEM) is a high-resolution analytical technique used to study the surface morphology and microstructural features of materials. A schematic of the SEM is presented in Figure 2.8, showing key components that work together to generate detailed images of surfaces. The electron gun produces a high-energy electron beam, which is focused and refined for precision by condenser lenses and an aperture. This beam is scanned across the sample surface utilizing scanning coils, while the objective lens provides fine adjustments for accurate imaging. The sample stage, which is adjustable in height, tilt, and rotation, securely holds the sample in place during analysis [74].

When the electron beam interacts with the sample, various signals are generated. Secondary electrons (SE) provide high-resolution images of surface morphology due to their low energy and shallow emission depth. Backscattered electrons (BSE), produced by elastic scattering with atomic nuclei, retain a large portion of their initial energy, and their intensity is dependent on the atomic number (Z) of the material, thus offering compositional contrast where elements with higher Z appear brighter. Additionally, characteristic X-rays emitted during these interactions are detected by Energy-Dispersive X-ray Spectroscopy (EDS), enabling qualitative and quantitative elemental analysis based on the unique energy signatures of each element [75].

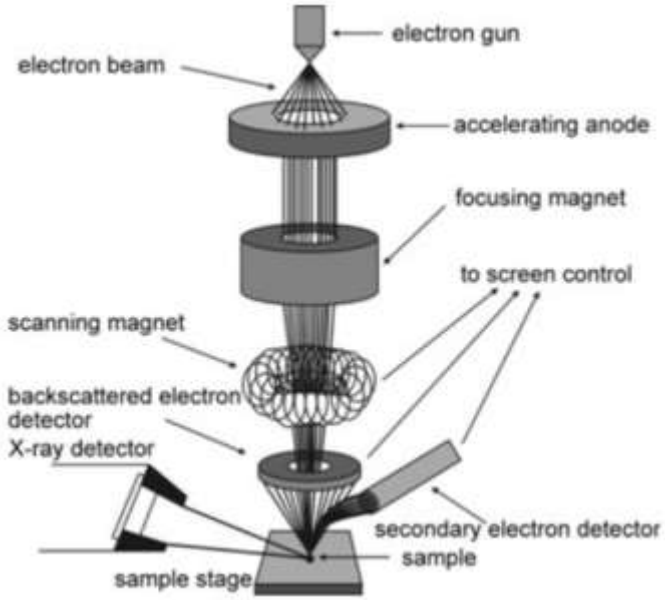

Figure 2.8 Schematic of scanning electron microscope [76].

2.4.3 Sieverts-Type Apparatus

The Sieverts technique is a volumetric method for evaluating the hydrogen storage properties of materials. The volumetric technique measures the change in hydrogen pressure within a fixed volume in direct contact with the sample. In this work, the hydrogenation properties were characterized by using a homemade volumetric Sievert's type apparatus consisting of a hydrogen reservoir, valves, a pressure gauge, a vacuum pump, and two calibrated volumes, as illustrated schematically in Figure 2.9. The principle of this technique involves the measurement of pressure changes in a calibrated system to determine the amount of hydrogen absorbed or desorbed by the material with high accuracy. Hydrogen absorption decreases the pressure, whereas desorption increases the pressure [76,77].

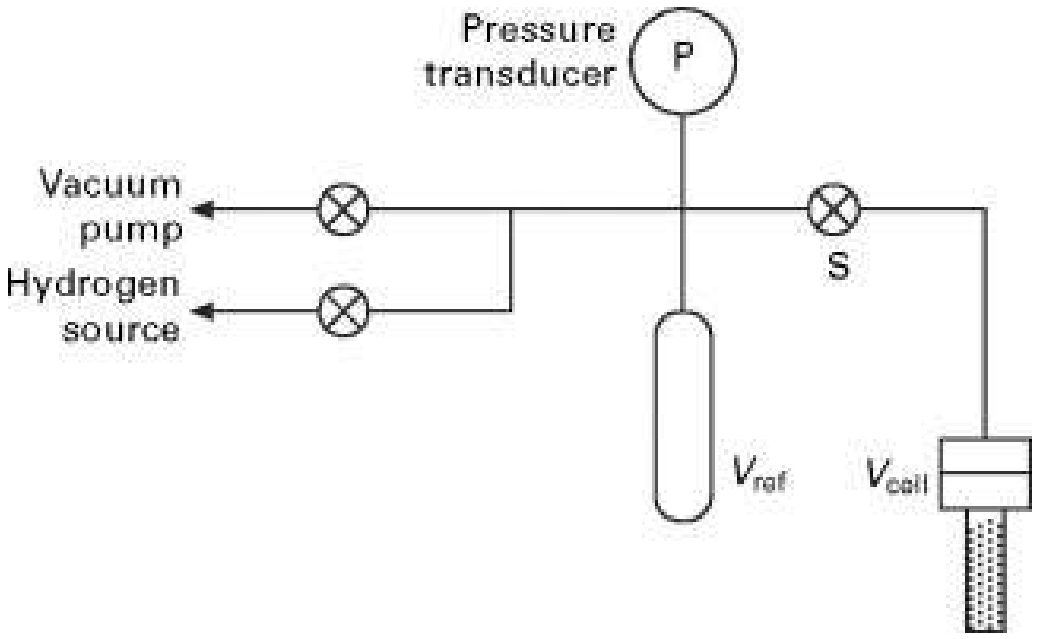

Figure 2.9 Schematic diagram of Sieverts-type apparatus [77].

The amount of hydrogen absorbed by the sample is calculated using the real gas equation:

$$\mathrm{PV} = \mathrm{nRT}\ (1 + \frac{\mathrm{nB}}{\mathrm{V}}), \tag{2.2}$$

Where *P* is the pressure, *V* is the volume, *n* is the number of moles of hydrogen, *R* is the universal gas constant, B is the second virial coefficient that is temperature dependent, and *T* is the absolute temperature of the hydrogen gas.

The volume of the apparatus was constant, and the temperature was stable during the measurement to provide an accurate value by minimizing thermal fluctuations. The amount of hydrogen absorbed or desorbed is calculated as:

$$n = \frac{V\Delta P}{RT\left(1+\frac{B}{V}\right)}, \tag{2.3}$$

The weight percentage of absorbed hydrogen can then be calculated using the following equation:

$$\text{wt. \% H absorbed} = \frac{\text{mass}_H}{\text{mass}_{sample}+\text{mass}_H}, \tag{2.4}$$

CHAPTER III.

EFFECT OF MECHANICAL PROCESSING ON FIRST HYDROGENATION OF GAS-ATOMIZED $Ti_{0.488}Fe_{0.460}Mn_{0.052}$ ALLOY

This chapter focuses on the primary experimental investigations performed on the as-received gas atomized $Ti_{0.488}Fe_{0.460}Mn_{0.052}$ alloy. Several mechanical activation techniques, including cold rolling, ball milling, and cold pressing, were applied to evaluate their effectiveness in the first hydrogenation of the alloy after long air exposure. The hydrogenation behavior obtained from these treatments was systematically compared to assess differences in activation performance and kinetic response.

3.1 Content of Article

Chapter III's content was published in *hydrogen* Journal, Volume 6, Issue 4 on December 2, 2025 (Article number 1144). The article is accessible at: https://doi.org/10.3390/hydrogen6040114 .

Effect of Mechanical Processing on First Hydrogenation of Gas-Atomized $Ti_{0.488}Fe_{0.460}Mn_{0.052}$ Alloy

Authors: Seyedehfaranak Hosseinigourajoubi [1], Chris Schade [2] and Jacques Huot [1,*]

[1] Hydrogen Research Institute, Université du Québec à Trois-Rivières, Trois-Rivières, QC G9A5H7, Canada; seyedeh.faranak.hosseini.gourajoubi@uqtr.ca

[2]GKN Hoeganaes Innovation Centre & Advanced Materials, Cinnaminson, NJ 08077, USA; chris.schade@hoeganaes.com

* Correspondence: jacques.huot@uqtr.ca; Tel.: +1-819-376-5011 (ext. 3576); Fax: +1-819-376-5164

3.2 Abstract

In this paper, we report the effects of cold rolling, ball milling, and cold pressing on the first hydrogenation behavior of $Ti_{0.488}Fe_{0.460}Mn_{0.052}$ alloy synthesized by gas atomization and exposed to the air for an extended period. It was found that cold pressing led to a higher hydrogen absorption capacity of 1.9 wt.%, while ball milling significantly improved the kinetics, achieving an incubation time of only 7 min. The cold-rolled sample (5 passes) showed a hydrogen absorption capacity similar to the ball-milled sample (1.5 wt.%) but with a slower hydrogenation rate. To further optimize the cold rolling process, the influence of the rolling atmosphere and the number of passes was systematically examined. In both air and argon, increasing the number of cold rolling passes resulted in longer incubation times. However, samples rolled under argon showed shorter incubation times compared to those rolled in the air. The difference between the two atmospheres became more pronounced after 20 rolling passes; the sample rolled in argon showed an incubation time of 55 min, whereas the sample rolled in air failed to absorb hydrogen even after 24 h.

Keywords: hydrogen storage; metal hydride; TiFe; gas atomization; cold rolling; ball milling; cold pressing; argon atmosphere.

3.3 Introduction

Hydrogen storage using metal hydrides is recognized as a safe and cost-effective method, providing high volumetric hydrogen density at moderate temperatures and pressures [78-80]. Among the reversible metal hydrides, FeTi-based alloys are interesting due to their ability to undergo reversible hydrogen absorption at conditions close to room temperature and atmospheric pressure, as well as the abundance and accessibility of their constituent elements [34,81-83].

FeTi hydrogen storage alloys suffer from sluggish hydrogen uptake, primarily due to the formation of stable oxide layers on the surface [56,84,85]. Activation of the TiFe alloys synthesized through conventional methods such as arc melting requires repeated heating cycles at approximately 400 °C under vacuum, followed by exposure to high hydrogen pressures (up to 6.5 MPa) to initiate hydrogen absorption [33]. This necessity for high-temperature and high-pressure activation represents an additional cost and a significant barrier to their commercial application.

Various strategies have been proposed to enhance the absorption kinetics of these materials. One common approach is partial substitution of Fe by transition metals such as Mn [37,43,86-88], Cr [32,89], and Ni [90,91]. Modi et al. reported that the reactivation of the $TiFe_{0.85}Mn_{0.15}$ alloy, which had been deactivated due to surface oxidation from air exposure, was significantly improved by applying a single heat treatment cycle (without the need for multiple heat treatments) at temperatures up to a maximum of 300 °C under hydrogen pressure [86]. Chung and Lee observed that partially substituting Fe with Mn promoted activation, which was attributed to the formation of secondary phases [92]. Fruchart et al. also reported that Mn addition increases the unit cell volume, which facilitates the hydrogen absorption at lower pressures [93].

Furthermore, the addition of a small amount of Zr to TiFe often leads to the formation of a secondary phase which acts as a gateway for hydrogen diffusion [45,46,94-97]. Manna et al. found that as-cast TiFe + 4 wt.% Zr absorbed 1.5 wt.% hydrogen after 45 min of

incubation time [94]. Jain et al. demonstrated that the addition of zirconium, either in its pure form or as an alloy, enabled the activation of TiFe after arc melting, without requiring any prior treatment [97].

Mechanical treatments such as cold rolling (CR) [6,42,94,98], ball milling (BM) [38,66,99,100], and high-pressure torsion (HPT) [40,101] are also promising methods for improving the activation behavior of TiFe alloys. These techniques can introduce defects, reduce particle size, and create fresh surfaces that enhance hydrogen uptake kinetics [42,94,102]. Abe et al. found that TiFe alloys synthesized via mechanical alloying followed by annealing could absorb hydrogen at room temperature. They observed that the first hydrogenation behavior of mechanically alloyed TiFe was significantly improved compared to conventional TiFe alloys produced by induction melting [66]. Chiang et al. prepared TiFe by arc melting and subjected the alloy to ball milling under hydrogen [103]. Their findings indicated that ball milling in hydrogen atmosphere enabled TiFe to absorb hydrogen without requiring an activation treatment. Vega et al. reported that TiFe processed by arc melting and subsequently subjected to 20 or 40 cold rolling passes under an inert atmosphere could absorb hydrogen rapidly at room temperature without the need for thermal activation, reaching a hydrogen absorption capacity of 1.4 wt% [6]. Gómez et al. found that nanostructured TiFe synthesized by the high-pressure torsion (HPT) method could absorb hydrogen at room temperature with fast kinetics after an activation treatment by a single-cycle evacuation at 673 K for 2 h [101]. Manna et al. studied TiFe + 4 wt% Zr + 2 wt% Mn alloy produced by the induction melting method and reported that after seven days of air exposure, the first hydrogenation kinetics were slow, with a long incubation time [94]. After 30 days of air exposure, no hydrogen absorption was observed. However, they showed that the air-exposed alloy could still be hydrogenated after ball milling or cold rolling, although with reduced capacity and slower kinetics. Similarly, Ulate-Kolitsky et al. investigated the same TiFe + 4 wt% Zr + 2 wt% Mn alloy produced by gas atomization, a method capable of directly producing metallic powders with high cooling rates, resulting in refined microstructures [42]. They demonstrated that gas-atomized alloy exhibited finer microstructures compared to induction-melted alloy, and cold rolling was more effective in recovering the hydrogenation performance of the atomized alloy compared to induction-

melted samples. These results indicate that the effectiveness of cold rolling strongly depends on the alloy's microstructure. Patel et al. investigated the effect of cooling rate on the microstructure and hydrogenation performance of TiFe + 4 wt.% Zr alloy and found that higher cooling rate led to a finer microstructure, which significantly improved hydrogen absorption kinetics [63]. These studies suggest that gas atomization could be a promising method for the production of metal hydride alloys with refined microstructures.

Despite these advancements, most studies on TiFe-based alloys have focused on samples produced by conventional casting methods, while investigations on gas-atomized alloys remain scarce. Moreover, most existing works focus on a single mechanical processing technique (such as cold rolling or ball milling), whereas comparative evaluations of different treatments are limited. In this work, we address this gap by investigating the first hydrogenation behavior of $Ti_{0.488}Fe_{0.460}Mn_{0.052}$ alloy synthesized by gas atomization and stored in air for more than two years. Three mechanical treatments, cold rolling, ball milling, and cold pressing, were systematically compared. In addition, the effects of rolling atmosphere and number of passes on the first hydrogenation are reported. This approach provides new insights into how different processing routes influence the activation of gas-atomized TiFe-based alloys.

3.4 Materials and Methods

3.4.1 Materials

The $Ti_{0.488}Fe_{0.460}Mn_{0.052}$ alloy in powder form was provided by GKN Hoeganaes (Cinnaminson, USA). The powder was produced via gas atomization under an argon atmosphere. After production, the samples were stored in the air for over 2 years.

3.4.2 Morphology and Crystal Structure

The microstructure and morphology of the powder were investigated using a Hitachi SU1510 scanning electron microscope (SEM) (Hitachi High-Tech Canada, Toronto, ON, Canada). Elemental composition was determined through Energy Dispersive X-ray Spectroscopy (EDX) with an Oxford Instrument X-Max system (Abingdon, UK), ensuring high analytical resolution.

The phase composition and crystal structure of the samples were analyzed by X-ray diffraction (XRD) using a Bruker D8 Focus powder diffractometer (Madison, WI, USA) with Cu Kα radiation. The resulting XRD patterns were evaluated using the Rietveld refinement software TOPAS V6.

3.4.3 Alloy Processing

High-energy ball milling was performed using a SPEX 8000M high-energy ball mill (SPEX SamplePrep, Metuchen, NJ, USA). The powder-to-ball mass ratio was 1:10, and milling was carried out for 10 min using a 55 cc stainless steel crucible. The vibration frequency was 1060 cycles per minute. All the loading and unloading of the powder were performed inside an argon-filled glove box to prevent contamination.

Cold pressing was carried out using a hydraulic press manufactured by Research & Industrial Instruments Company (London, UK). A die with a diameter of 14 mm was used to compact the powder under uniaxial pressure. The sample was subjected to a force of 12 tons for 2 min. After cold pressing, the obtained pellet was manually crushed into powder using a hardened steel mortar and pestle in the air.

Cold rolling in the air was conducted using a modified Durston DRM 130 model (Durston Tools, High Wycombe, UK), with powder being rolled vertically between two 0.5 mm-thick 316 stainless steel plates to avoid contamination. For cold rolling in argon, an International Rolling Mills (Pawtucket, RI, USA) was placed inside an argon-filled

glove box. Rolling speed was 20 rpm for both air and argon atmospheres. The roller gap was set to 1.1 mm; considering the combined thickness of the two steel plates (1.0 mm), the effective rolling space available for the powder was approximately 0.1 mm.

3.4.4 Hydrogenation Properties

The first hydrogenation tests were carried out at room temperature (25 °C) under a hydrogen pressure of 2000 kPa using a homemade Sievert-type apparatus. For each first hydrogenation test, one gram of powder was placed in the sample holder and evacuated for 15 min before the measurement.

3.5 Results and Discussion

Figure 3.1 presents the microstructure of the atomized $Ti_{0.488}Fe_{0.460}Mn_{0.052}$ powder, revealing two distinct regions: a grey matrix and a darker grey filamentous region.

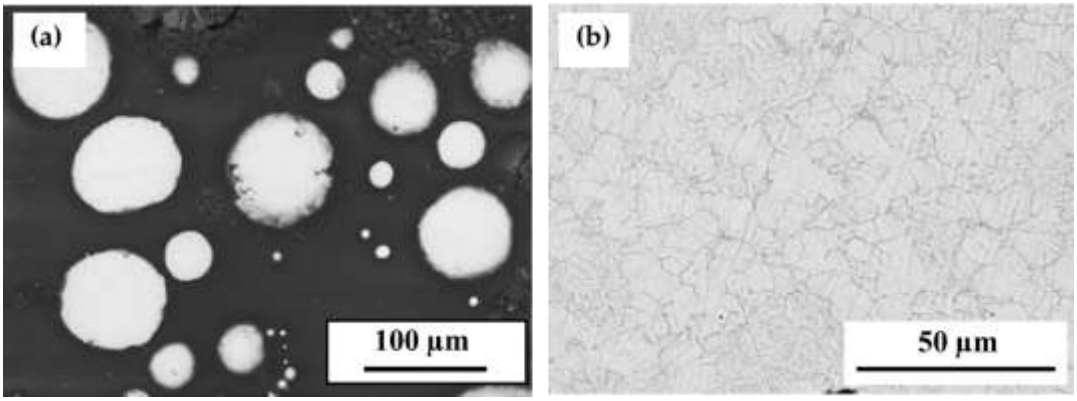

Figure 3.1 SEM images of the microstructure of the gas-atomized powder at magnifications of (a) 300× and (b) 1000×.

Figure 3.2a shows a higher-magnification backscattered electrons micrograph. At this magnification, three regions are visible. The main region (matrix) is light grey. Two secondary regions are seen: a darker grey region (Spectrum 2) and a much smaller black

region (Spectrum 3). The chemical composition of the bulk material, matrix, and secondary phases, as determined by EDS, is summarized in Table 3.1.

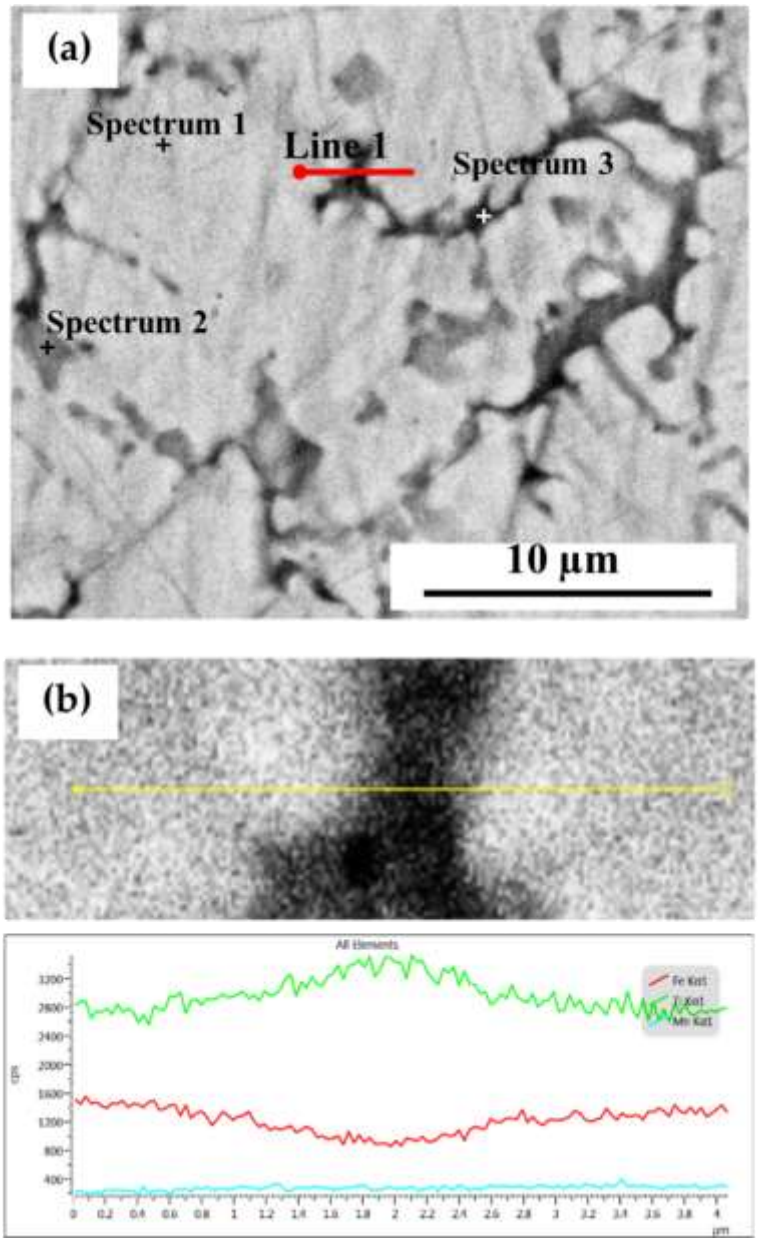

Figure 3.2 (a) High-magnification backscattered electron image of the EDS-analyzed regions of the atomized powder, (b) line analysis.

Table 3.1.Elemental composition in atomic percent (at. %) from EDX analysis of the gas-atomized powder. Error on the last significant digit is in parentheses.

Element	Nominal	Bulk	Spectrum 1 (Matrix)	Spectrum 2 (Dark Grey Region)	Spectrum 3 (Black Region)
Ti	48.8	49.4 (3)	47.5 (5)	59.1 (3)	66.6 (2)
Fe	46	45.3 (4)	48.4 (6)	34.8 (2)	26.3 (4)
Mn	5.2	5.3 (2)	4.1 (5)	6.1 (3)	7.1 (1)

Based on bulk composition measurement, the Ti, Fe, and Mn concentrations are near the nominal composition. The elemental concentrations of the matrix are close to TiFe, with Mn seemingly substituting on both Ti and Fe sites. Both the black and darker grey regions are rich in Ti and have a Mn concentration slightly higher than that of the matrix. For both regions, the composition is close to Ti_2Fe.

The interface of the matrix and second phase was investigated by line analysis (Figure 3.2b). The abundance of Ti slowly increases from the edge toward the center of the secondary region while Fe abundance decreases. Mn concentration is almost constant in both the matrix and the secondary phase. There is no indication of segregation at the edge.

The atomized $Ti_{0.488}Fe_{0.460}Mn_{0.052}$ alloy was exposed to hydrogen at room temperature under a pressure of 2000 kPa for 24 h. However, no hydrogen absorption was observed. Surface oxides are easily formed on TiFe alloys, which can hinder hydrogen absorption [45,102,104]. Therefore, this lack of hydrogen absorption is likely attributed to the long air exposure before hydrogenation. Previous studies have demonstrated that mechanical processing techniques, such as ball milling and cold rolling, could improve activation kinetics after air exposure by introducing cracks and generating fresh surfaces [6,38,42,66,94,98-100]. To address the activation issue, various mechanical processing methods were applied and compared to the activation of gas-atomized $Ti_{0.488}Fe_{0.460}Mn_{0.052}$ alloy. These included cold rolling (5 passes), ball milling (10 min), and cold pressing.

Figure 3.3 illustrates the morphology of the atomized and mechanically processed powders. Figure 3.3a,b show that the atomized powder consists of a mixture of spherical and irregularly shaped particles. The spherical particles range in size from less than 20 μm to 300 μm, while the irregularly shaped particles measure between 100 μm and 400 μm.

After five passes of cold rolling, the average particle size decreased significantly due to the fragmentation of larger particles under mechanical deformation (Figure 3.3c). Most of the particles were very small, with sizes below 20 μm. However, some larger particles, approximately 100 μm in size, could still be observed, indicating that the fragmentation process is not entirely uniform. Figure 3.3d further highlights the formation of cracks and highly fragmented particles, which become more evident at higher magnification. The cracks are marked with arrows.

Ball milling also resulted in the breakdown of particles into finer, irregularly shaped particles (Figures 3.3e,f). In contrast, cold pressing did not significantly reduce the average particle size (Figure 3.3g). However, a higher-magnification image (Figure 3.3h) reveals the presence of numerous cracks on both spherical and irregular particles.

The XRD patterns of atomized $Ti_{0.488}Fe_{0.460}Mn_{0.052}$ and mechanically processed samples before hydrogenation are presented in Figure 3.4. In addition, the XRD pattern of atomized TiFe is shown as reference sample. In all cases, only the TiFe phase is seen with no indication of other phases. As shown in Figure 3.1, the secondary regions exhibit a thin, filamentous structure and are present in a relatively small quantity compared to the matrix. Due to its limited volume and morphology, the diffraction intensity of these secondary phases was weak. Similarly, surface oxides typically form only a very thin layer (often just a few nanometers thick) on the powder surface. Because they are so thin and not very abundant, their XRD Bragg's peaks are very weak and broad, making them hard to distinguish from the background.

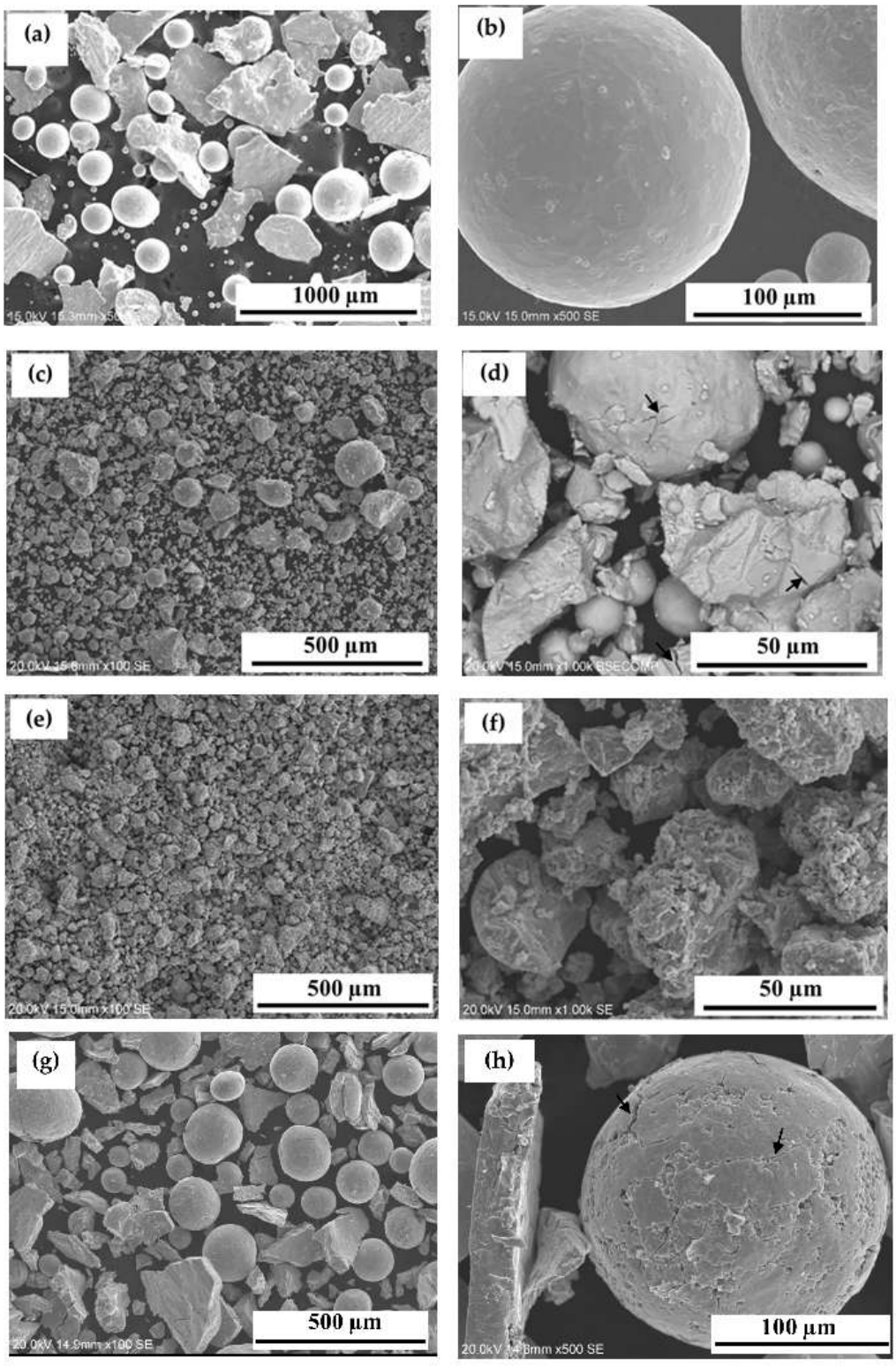

Figure 3.3 Morphology of gas-atomized powder (a,b); mechanically processed powders after 5 passes of cold rolling (c,d), 10 min of ball milling (e,f), and cold pressing (g,h).

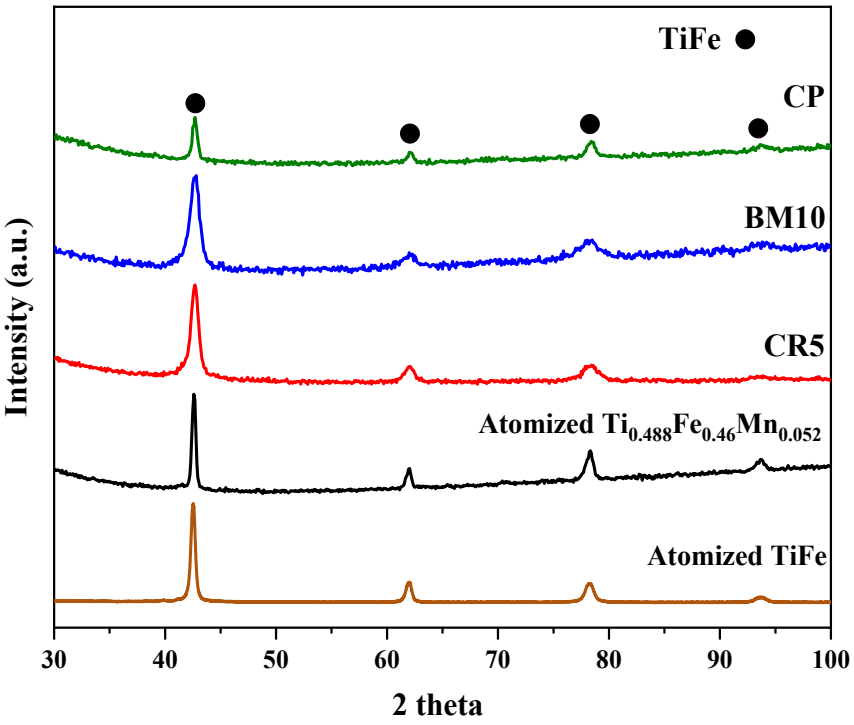

Figure 3.4 XRD patterns of gas-atomized powder and mechanically processed powders (5CR-10BM-CP) before hydrogenation.

Table 3.2 summarizes the Rietveld refinement results based on the XRD patterns of Figure 3.4. As the TiFe pattern was taken on a different diffractometer, we could not perform Rietveld's refinement on this one using the fundamental parameters. However, the lattice parameter of TiFe phase in reference TiFe alloys was 2.97971 (6) Å. Substituting Mn by Fe led to increase in lattice parameter to 2.9828 (4). The lattice parameters remained nearly constant across atomized $Ti_{0.488}Fe_{0.460}Mn_{0.052}$ and mechanically processed samples. However, a reduction in crystallite size and an increase in microstrains were observed after mechanical processing, which can be attributed to the introduction of defects and dislocations in the crystal lattice. Among the samples, the ball-milled powder displayed the smallest crystallite size and the highest microstrain, whereas the cold-pressed sample exhibited the largest crystallite size and the lowest microstrain.

Table 3.2 Rietveld's refinement of TiFe phase. The error on the last significant digit is shown in parentheses.

Sample	Lattice Parameter (Å)	Crystallite Size (nm)	Microstrain (%)
As-Atomized	2.9828 (4)	44.0 (5)	0.132 (6)
CR5	2.9829 (6)	25.4 (2)	0.196 (2)
BM10	2.9838 (7)	8.6 (6)	0.302 (3)
CP	2.9822 (9)	29.6 (4)	0.142 (2)

Figure 3.5 shows the hydrogenation curves for all samples at room temperature and hydrogen pressure of 2000 kPa. Unlike the as-received (gas-atomized) $Ti_{0.488}Fe_{0.460}Mn_{0.052}$ sample, which did not absorb hydrogen, all mechanically processed samples successfully absorbed hydrogen. It is worth mentioning that pure TiFe alloy could not absorb hydrogen at room temperature and hydrogen pressure of 2000 kPa, even after mechanical processing, whereas the $Ti_{0.488}Fe_{0.460}Mn_{0.052}$ alloy readily absorbed hydrogen following mechanical processing.

The cold-pressed sample exhibited the highest hydrogen absorption capacity of 1.9 wt.%, and cold-rolled and ball-milled samples both reached 1.5 wt.% after 24 h. In terms of kinetics, the BM10 sample demonstrated the fastest hydrogenation, with an incubation time of about 7 min, while both cold-rolled and cold-pressed samples had a longer incubation time of approximately 15 min.

Remarkably, despite the atomized powder being exposed to air for more than two years, each type of mechanical processing was able to activate the alloy and achieve good hydrogenation kinetics. For comparison, Modi et al. investigated the hydrogenation behavior of a $TiFe_{0.85}Mn_{0.15}$ alloy produced by arc melting [86]. After arc melting the alloy was subjected to ball milling for 30 min. Ball-milled alloy exhibited good kinetics and absorbed 1.2 wt.% hydrogen with no incubation time. However, after exposure to air for just 2 h, the alloy became oxidized and lost its hydrogen absorption capability. By heating

to 300 °C under hydrogen pressure, reactivation was achieved, but with a prolonged incubation time of 40 min and a reduced capacity of 0.9 wt.%. In the present work, all mechanical treatments activated the alloy with shorter incubation times and higher hydrogen capacities compared to Modi et al., which can be attributed to microstructural differences between gas-atomized and arc-melted alloys.

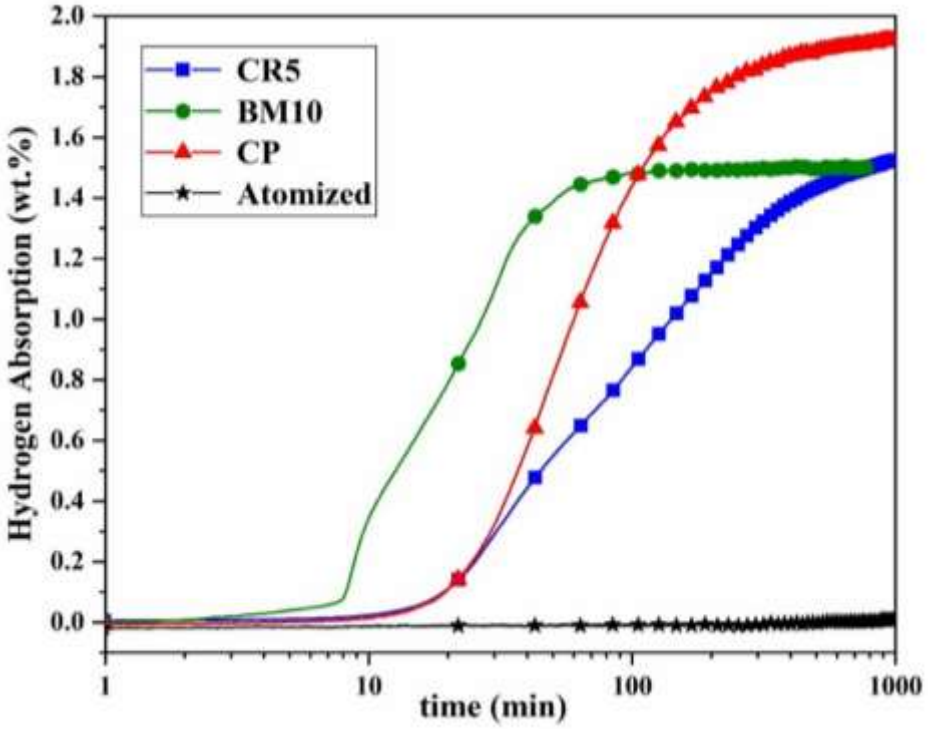

Figure 3.5 Hydrogenation curves at room temperature under 2000 kPa hydrogen pressure for as-received and mechanically processed powders.

Dematteis et al. further studied TiFe-alloys with partial substitution of Fe by Ti and Mn [88]. Samples with different compositions in the range from 48.8 at% to 54.1 at% Ti, and from 0 to 5.3 at% Mn were prepared by induction melting and subsequent annealing at 1000 °C for one week. Their results showed that activation generally required 5 MPa of hydrogen pressure and heating up to 400 °C. Only Ti-rich compositions could be activated under milder conditions (room temperature and 2500 kPa H2). Although the alloy studied here is not Ti-rich, it was activated at room temperature and moderate pressure, which can

be attributed to the finer microstructure of the gas-atomized material compared to induction-melted alloys.

The improvement in hydrogenation behavior after mechanical processing can be attributed to the refinement of the crystalline structure and the introduction of defects during deformation. As observed in Figure 3.3, mechanical processing induced cracks in the particles, likely facilitating hydrogen diffusion. The mechanical processing also introduces structural defects, such as vacancies and dislocations, which further enhance hydrogen transport within the material [105]. Rietveld refinement analysis revealed a decrease in crystallite size after mechanical processing, which corresponded to an increase in grain boundary density. These grain boundaries could serve as pathways that facilitate hydrogen diffusion [38,94,106]. Consequently, the hydrogenation kinetics improve after mechanical processing due to the combined effects of particle fragmentation, reduction in crystallite size, and the formation of grain boundaries.

As previously mentioned, the ball-milled sample not only exhibited the shortest incubation time but also demonstrated the fastest hydrogenation kinetics. As shown in Table 3.2, the BM10 sample had the smallest crystallite size, which implies a higher grain boundary density. Grain boundaries can facilitate hydrogen diffusion and act as nucleation sites for hydride formation [107]. In the study of Emami et al., it was reported that ball milling leads to the formation of nanograins, and the nanograin boundaries act as effective pathways for hydrogen diffusion [38].

Beyond the kinetics, differences in hydrogen storage capacity among the samples indicate the influence of mechanical processing on hydrogen storage behavior. As shown in Figure 3.5, the cold-pressed sample exhibited the highest capacity of 1.9 wt.% ± 0.1 wt.%. This value agrees with the nominal hydrogen capacity of TiFe alloy (1.86 wt.%).

According to the hydrogenation curves in Figure 3.5, after 1000 min, the cold-rolled sample continues to absorb hydrogen at a very slow rate, while the ball-milled sample has already reached its maximum capacity (1.5 wt.%). This indicates that the ball-milled

sample had a lower overall capacity compared to the cold-pressed one. The reduced capacity of the ball-milled sample may be attributed to the crystallite size. As previously discussed, the BM10 sample had the smallest crystallite size, resulting in a higher density of grain boundaries. Lv et al. found that as ball milling time increased and crystallite size decreased, the hydrogen storage capacity decreased [106]. They proposed that although grain boundaries facilitate hydrogen diffusion, they do not store hydrogen themselves. This may explain the lower overall capacity of the ball-milled sample, despite its faster kinetics and shorter incubation time.

Regarding the cold-rolled sample, the loss of capacity may be explained by the formation of oxides as the cold rolling was performed in the air. To verify this hypothesis, cold rolling was performed under both air and argon atmospheres for 5, 10, and 20 passes to compare the influence of rolling atmosphere on the hydrogenation behavior.

Figure 3.6 shows hydrogenation curves at room temperature and hydrogen pressure of 2000 kPa for cold-rolled samples in the air. After 5 CR in the air, absorption started after 15 min of incubation time. With 10 CR in air incubation time was increased to 35 min. After 20 CR in the air, the sample was not activated in 24 h. The difference in incubation time could be related to the surface condition of the materials. Increasing cold rolling passes in the air may lead to surface oxidation that can act as barriers to hydrogen absorption. Sleiman et al. similarly reported that while the as-cast Ti1V0.9Cr1.1 alloy could not be activated, a single cold rolling pass enabled immediate activation [108]. However, when the number of passes increased to six, the incubation time rose to about 10 min, the activation kinetics slowed, and the absorption capacity decreased.

Figure 3.7 shows the first hydrogenation of samples cold rolled in argon. Compared to rolling in the air, the incubation time is shorter. After 5 and 10 rolling passes, the incubation times were only 3 and 4 min, respectively. The hydrogen absorption capacity after 24 h was about 1.5 wt.%, which is like the samples rolled in the air. The most notable difference appeared after 20 passes; while the 20CR-air sample showed no activation within 24 h, the 20CR-argon sample began absorbing hydrogen after 55 min and reached

a capacity of 1.6 wt.% after 24 h. Even under argon atmosphere, increasing the number of cold rolling passes to 20 resulted in a longer incubation time (55 min), similar to what was observed for cold-rolled samples in the air. This suggests that, regardless of oxidation, excessive deformation may hinder the first hydrogenation. This could be attributed to the excessive plastic deformation induced by multiple passes. As the number of passes increases, the material accumulates a higher density of dislocations, defects, and internal stresses, which can disrupt hydrogen diffusion.

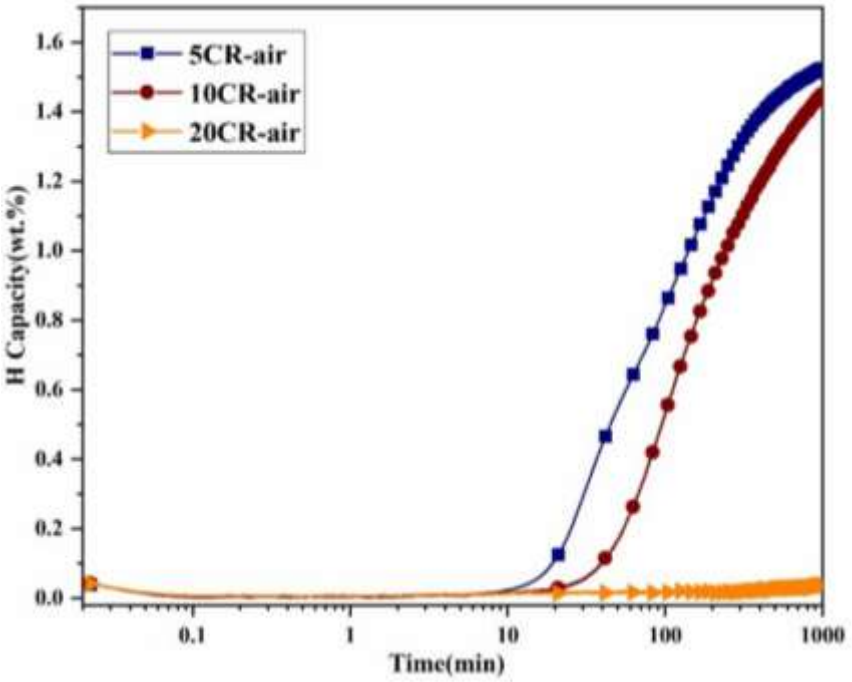

Figure 3.6 Activation curves of 5, 10, and 20 passes cold-rolled powders in air at RT/2000 kPa.

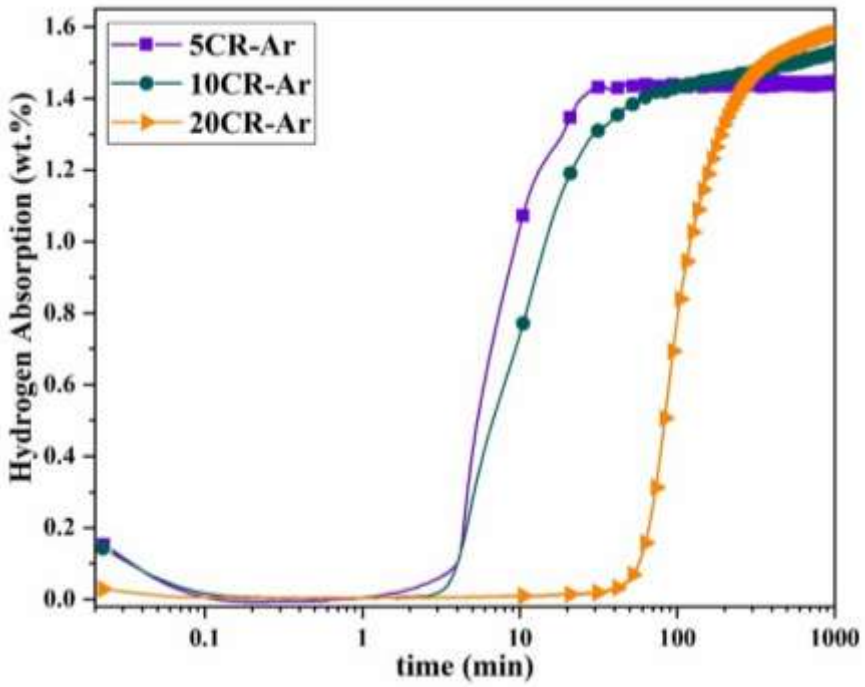

Figure 3.7 Activation curves of 5, 10, and 20 passes cold-rolled powders in argon at RT/2000 kPa.

The crystal structure of cold rolled samples in the air and argon was investigated by X-ray diffraction, and the patterns are shown in Figure 3.8. The corresponding Rietveld refinement data are summarized in Table 3.3. We see that increasing the number of rolling passes led to a reduction in crystallite size and increasing microstrain. The effect was the same for the samples rolled in argon compared to the ones rolled in the air. In fact, the crystal parameters were essentially the same for the air and argon cases. Therefore, the difference in incubation time between air and argon rolling atmosphere could not be attributed to a different crystal structure. It should be due to some surface effect that could not be seen by X-ray diffraction due to the large penetration depth of the oxides. The possible Ti, Fe and TiFe oxides have penetration depth between 2 and 10 microns. Considering that the surface oxide should have a thickness of nm, it is understandable that the presence of oxides could not be seen by X-ray diffraction. We are planning to perform XPS to obtain a better understanding of the surface composition.

Table 3.3 Rietveld's refinement of TiFe phase in cold rolled samples in air and argon. The error on the last significant digit is shown in parentheses.

Sample	Lattice Parameter (Å)	Crystallite Size (nm)	Microstrain (%)
5CR-Air	2.9829 (6)	25.4 (2)	0.196 (2)
10CR-Air	2.9839 (5)	14.3 (5)	0.213 (7)
20CR-Air	2.9841 (3)	12.1 (3)	0.235 (1)
5CR-Argon	2.9829 (9)	25.1 (8)	0.194 (1)
10CR-Argon	2.9831(3)	14.4 (8)	0.228 (1)
20CR-Argon	2.9832 (2)	12.7 (6)	0.231 (1)

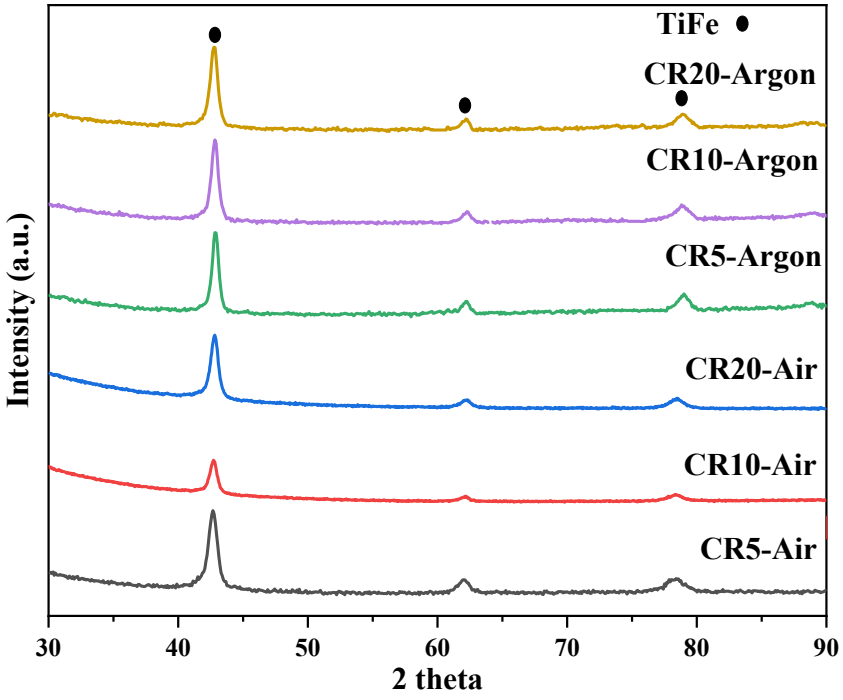

Figure 3.8 XRD patterns of cold rolled samples in air and argon before hydrogenation.

3.6 Conclusions

The effects of cold rolling, ball milling, and cold pressing on the microstructure and hydrogen storage properties of $Ti_{0.488}Fe_{0.460}Mn_{0.052}$ alloy were investigated. Cold pressing resulted in the highest hydrogen absorption capacity among the three methods, while ball milling significantly improved the first hydrogenation kinetics compared to cold rolling and cold pressing. Increasing the number of cold rolling passes in the air reduced hydrogen absorption kinetics, probably because of surface oxidation. Cold rolling under argon atmosphere produced a fast first hydrogenation. However, a higher number of passes in argon led to longer incubation times, suggesting that excessive deformation may hinder the first hydrogenation. These results suggest that combining different mechanical treatments could be explored in future studies to optimize both capacity and hydrogenation rate.

CHAPTER IV.

THE EFFECT OF ANNEALING ON THE FIRST HYDROGENATION BEHAVIOR OF ATOMIZED $Ti_{0.488}Fe_{0.460}Mn_{0.052}$ ALLOY

This chapter presents an experimental investigation of the effect of short-duration vacuum annealing on the microstructure and first hydrogenation behaviour of a gas-atomized $Ti_{48.8}Fe_{46.0}Mn_{5.2}$ alloy. The microstructural changes induced by annealing, particularly the transformation of the Ti_2Fe secondary phase from a filamentous to a globular morphology, were found to significantly reduce activation kinetics and final hydrogen capacity. The comparison between the as-atomized and annealed samples highlights the critical role of secondary phase morphology in hydrogen diffusion.

4.1 Content of Article

Chapter IV's content was published in the *Metals* Journal, Volume 15, Issue 3 on February 26, 2025 (Article number 251). The article is accessible at: https://doi.org/10.3390/met15030251.

The effect of annealing on the first hydrogenation behaviour of atomized $Ti_{48.8}Fe_{46.0}Mn_{5.2}$ alloy

Authors: Seyedehfaranak Hosseinigourajoubi [1], Chris Schade [2] and Jacques Huot [1,*]

[1] Hydrogen Research Institute, Université du Québec à Trois-Rivières, Trois-Rivières, QC G9A5H7, Canada; Seyedeh.Faranak.Hosseini.Gourajoubi@uqtr.ca

[2] GKN Hoeganaes Innovation Centre & Advanced Materials – New Jersey, USA; Chris.Schade@hoeganaes.com

* Correspondence: jacques.huot@uqtr.ca

4.2 Abstract

In this paper, we report the effect of annealing on the first hydrogenation behaviour of $Ti_{48.8}Fe_{46.0}Mn_{5.2}$ alloy. This alloy was produced by gas atomization and a portion of the powder was subjected to vacuum annealing at 1120°C for 1 hour. The goal was to investigate the usefulness of this atomized powder for hydrogen storage and to investigate the effect of annealing. Scanning electron microscopy (SEM) images revealed that both atomized and annealed alloys exhibit a two-phase structure. The atomized alloy consists of a main TiFe matrix and a filamentous Ti_2Fe-like phase. After annealing, the microstructure is globular. In addition to the microstructure, there was a change in the chemical composition of the matrix and secondary phase after annealing. The first hydrogenation at room temperature of both atomized and annealed samples required cold rolling. However, the kinetics was much slower for the annealed sample compared to the atomized sample. After the first hydrogenation, the XRD analysis identified the main phases as TiFe, $TiFeH_{0.94}$, and Ti_2FeH_3, indicating that both the TiFe and Ti_2Fe phases participated in hydrogen absorption during hydrogenation.

Keywords: TiFe alloy; hydrogen storage; metal hydride; first hydrogenation, annealing.

4.3 Introduction

Hydrogen is gaining attention as a renewable energy carrier due to its versatility and clean energy potential. When it comes to hydrogen storage, a reliable and efficient method is crucial for a wide utilization of hydrogen. Solid-state storage in metal hydrides could be suitable for storing hydrogen for a variety of applications [5,8]. Among the many different types of metal hydrides, TiFe has shown great potential for hydrogen storage applications due to its reasonable hydrogen storage capacity of 1.86 wt.% at low pressure and room temperature. Furthermore, this alloy is made from cost-effective raw materials. However, a major challenge is the first hydrogenation, the so-called activation, which is usually slow at room temperature. This is most likely due to the formation of surface oxides that act as a barrier for hydrogen dissociation and absorption [29,37,88,105]. In the pioneering work of Reilly and Wiswall [33], the first hydrogenation was preceded by heating the alloy to over 400°C for 30 minutes, either in a vacuum or at low hydrogen pressure, then cooling it to room temperature and applying a high hydrogen pressure of approximately 6000 kPa. The process had to be repeated several times until the hydrogenation occurred in about 15 minutes. Since then, several studies have used this type of activation procedure for TiFe alloys [34-36].

In addition to the above-mentioned repeated heating process, the activation issue can be overcome by other approaches: the addition of transition elements such as Mn [43,44], Zr [45,46], Cr [47], V [48,49], and Y[50,51]; addition of excess Ti in the stoichiometry[41]; and mechanical treatments [39,42,109]. Lv et al. studied the effects of doping, cold rolling, and forging on the microstructure and hydrogen storage properties of air-exposed TiFe + x wt.% (Zr+2V) (x = 0, 4, 5, and 6) alloys [46]. They concluded that doping with (Zr+2V) significantly improved the first hydrogenation kinetics of TiFe due to the formation of an hcp secondary phase, which can enhance the diffusion of hydrogen. Forging effectively reduced the incubation time and enhanced the first hydrogenation kinetics, while cold rolling improved absorption kinetics but resulted in lower hydrogen capacity.

Patel et al. investigated the effect of Zr and Mn on the microstructure and the first hydrogenation kinetic of TiFe alloy [59]. They concluded that the fastest kinetic and highest capacity was reached by doping with 2 wt% Mn and 4 wt% Zr. The enhanced activation kinetics was attributed to the presence of a large proportion of Ti_2Fe type phase, potentially because this phase could act as a gateway, facilitating hydrogen entry into the TiFe phase.

Ulate-Kolitsky et al. investigated the first hydrogenation of both cold-rolled and ball-milled TiFe-based alloy synthesized by gas atomization [42]. Cold rolling was shown to be more effective than ball milling for the regeneration of air-exposed atomized powder. Edalati et al. have shown that mechanical processing using severe plastic deformation (SPD) is effective at accelerating the hydrogenation kinetics [39]. They attributed it to the diffusivity of hydrogen that can be enhanced because of high dislocation and grain boundary density and high concentration of vacancies after SPD processing.

In this paper, the cold rolling method is used for the activation of $Ti_{48.8}Fe_{46.0}Mn_{5.2}$ alloy produced by gas atomization. Atomization is a method that is considered by the industry to produce commercial alloys. However, as this method involves rapid cooling, there are some concerns regarding the stability of the resulting phases. Moreover, atomized powders are often fragile and difficult to compact without heat treatment [65]. Therefore, it is crucial to understand the effects of annealing on phase stability, microstructural evolution, and chemical composition. In addition, annealing can significantly affect the hydrogenation properties of metal hydrides. Abe and Kuji noted that the TiFe alloy prepared by the mechanical alloying method exhibited a lower plateau pressure and reduced hydrogen reversibility at room temperature. However, after annealing at 600 °C for 3 hours, a wide plateau area could be obtained [66]. According to a study by Lee et al., the activation process of the TiFe compound can be facilitated by incorporating a small quantity of Cr or Mn as substitutes for Fe. However, when subjected to a homogenization treatment at 900°C for 80 hours, the activation rate decreased due to alterations in the amount and morphology of the second phase [67]. This indicates that annealing could improve the hydrogen absorption properties of the alloys by the reduction in plateau pressure in the PCT curve. However, compositional and morphological changes after

annealing may adversely affect activation. Also, for industrial applications, annealing for a long duration could be too costly. Therefore, the effect of a short time annealing on the microstructure and hydrogen storage properties of $Ti_{48.8}Fe_{46.0}Mn_{5.2}$ alloy synthesized by gas atomization was investigated.

4.4 Materials and Methods

The $Ti_{48.8}Fe_{46.0}Mn_{5.2}$ alloy was produced by GKN Hoeganaes Innovation Centre and Advanced Materials. The gas atomization was performed under pure argon with a VIGA-type furnace with a free-fall atomization ring configuration. After synthesis, the powder was stored in the air. A portion of the atomized powder was vacuum annealed at 1120°C for 1 hour in a batch furnace.

The morphology and microstructure of the powder were analyzed using a Hitachi Su1510 scanning electron microscope (Hitachi High-Tech Canada, Inc., Toronto, ON, Canada) equipped with an EDX – Energy Dispersive X-ray spectrometer (Abingdon, UK). The crystal structure of the alloys was analyzed by X-ray diffraction (XRD) measurement carried out on a Bruker D8 Focus diffractometer (Madison, WI, USA) with CuKα radiation. The XRD patterns were analyzed by the Rietveld method using TOPAS software (Bruker, Madison, WI, USA) to determine the alloy's phase abundance, lattice parameter, and crystallite size [70].

Cold rolling was performed vertically in the air with a modified Durston DRM 130 rolling mill (High Wycombe, Buckinghamshire, UK). The powder was inserted between two 316 stainless steel plates to avoid contamination by the rolls. Samples were cold rolled for 5 passes (5 CR).

The sample's hydrogen capacities and absorption kinetics were evaluated using a homemade Sievert-type apparatus. One gram of powders was placed in a sample holder and evacuated for 15 minutes before kinetic measurements. The absorption measurements

were taken at room temperature (25 °C) under 2000 kPa of hydrogen pressure or at 90 °C and a hydrogen pressure of 4500 kPa.

4.5 Results and Discussion

4.5.1 Microstructure

Figure 4.1 shows the backscattered electron micrographs of $Ti_{48.8}Fe_{46.0}Mn_{5.2}$ alloys in as atomized (AS) and vacuum-annealed (VA) conditions. The microstructure reveals the presence of two distinct regions: a matrix (gray) and a darker gray region. In the as atomized alloy, the darker regions have a filamentous structure, while in the VA sample, they are globular, forming distinct islands.

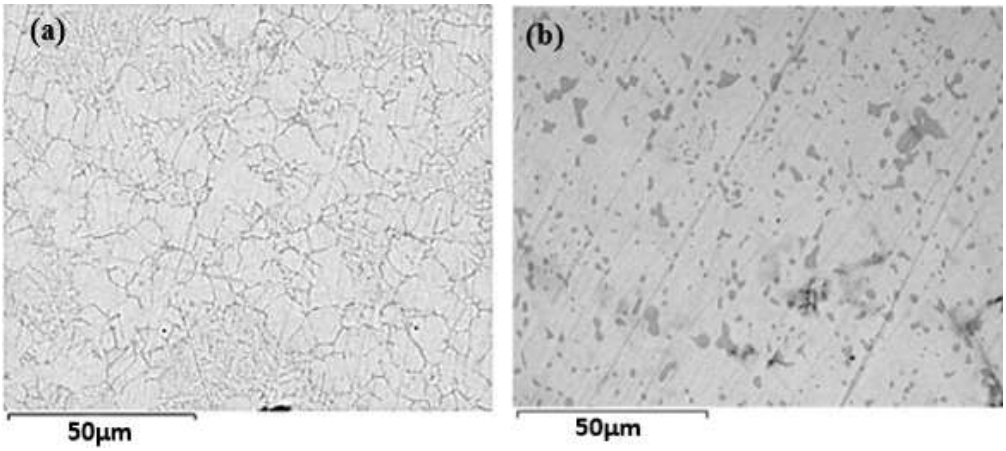

Figure 4.1 Backscattered electron micrographs of Ti48.8Fe46.0Mn5.2 alloys: (a) as atomized; (b) after vacuum annealing.

Figure 4.2 shows a higher magnification image of the atomized alloy analyzed by EDX. At this magnification, two distinct secondary regions are visible: a gray region and a black region. The chemical composition of the bulk material and each region are shown in Table 4.1. The values represent the elemental compositions (in atomic percent, at.%) of different phases within the as-atomized alloy, determined by Energy Dispersive X-ray (EDX) analysis. These compositions reflect the distribution of Ti, Fe, and Mn in the matrix and secondary phases. For the matrix region, the composition is TiFe with a small amount

of Mn. Both black and gray regions are Ti-rich and have a Mn concentration slightly higher than in the matrix. In fact, the stoichiometry of these two regions is close to Ti_2Fe. The Ti_2Fe is not a stable phase and is not included in the ASM phase diagram[110]. Reilly et al. tried to synthesize Ti_2Fe in order to study its hydrogen absorption behaviour [33]. They found that it exists above 1000 ℃ and below this temperature, it decomposes to TiFe and Ti. Dong et al. prepared Ti_2Fe alloy using an arc furnace followed by remelting in an induction furnace and subsequent spin quenching[111]. They reported that the structure type of Ti_2Fe is Ti_2Ni. Guéguen et al. observed Ti_2Fe precipitates in the TiFe matrix after arc melting and annealing at 1000 ℃ for one week under argon atmosphere [49]. Therefore, despite not being a stable phase, Ti_2Fe could be relatively easy to obtain in Ti-Fe alloys under specific high-temperature conditions followed by rapid cooling or controlled annealing. In our study, the sample was produced by gas atomization, where the melt underwent rapid cooling. Additionally, the annealing temperature is comparable to the heat treatment temperatures in the above-mentioned studies. In the present investigation, the Ti_2Fe phase was obtained after just one hour of annealing.

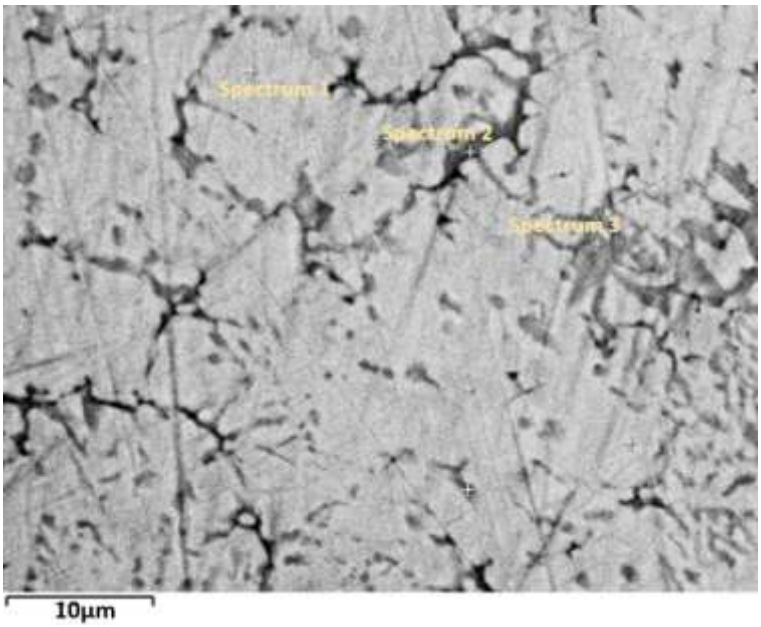

Figure 4.2 Higher magnification image of the microstructure of the as-atomized sample. Spectrum 1: matrix, Spectrum 2: black region, Spectrum 3: gray region.

Table 4.1 EDX analysis of phases of atomized alloys. Error on the last significant digit is indicated in parentheses.

Element	Nominal	Bulk	Matrix	Gray region	Black region
Ti	48.8	49.4(3)	47.5(5)	59.1(3)	66.6(2)
Fe	46	45.3(4)	48.4(6)	34.8(2)	26.3(4)
Mn	5.2	5.3(2)	4.1(5)	6.1(3)	7.1(1)

A higher magnification image of the vacuum-annealed sample (Figure 4.3) revealed a two-phase microstructure: a gray matrix and a dark second phase. The EDX analysis results, presented in Table 4.2, provide the elemental composition of both the matrix and the secondary phase in the vacuum-annealed alloy, expressed in atomic percent (at.%). The matrix composition is TiFe with Fe being substituted by Mn. The dark phase composition is close to $(Ti, Mn)_2Fe$.

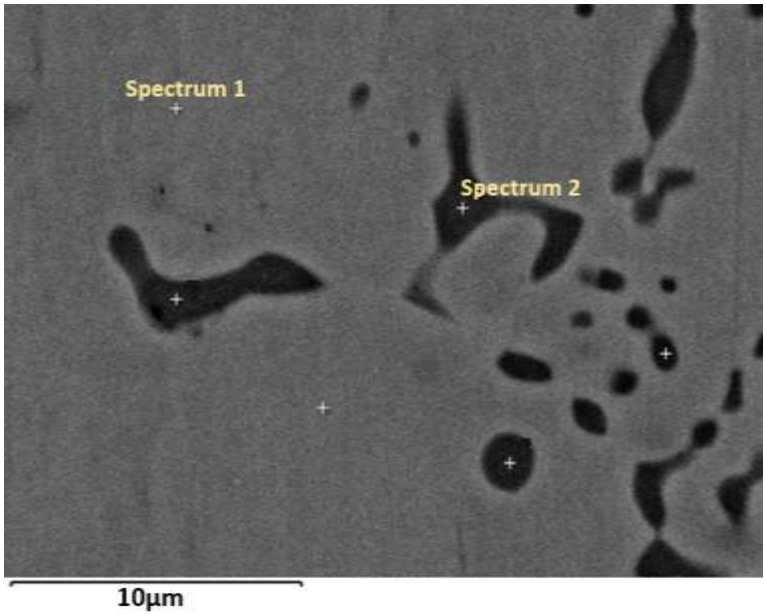

Figure 4.3 Higher magnification image of the microstructure of the vacuum annealed. Spectrum 1: matrix, spectrum 2: black region.

Table 4.2 EDX analysis showing the elemental composition of the matrix and second phase of vacuum annealed alloy. Error on the last significant digit is indicated in parentheses.

Element	Nominal	Bulk	Matrix	Gray region
Ti	48.8	48.9(5)	49.5(4)	62.2(7)
Fe	46	46.1(7)	45.5(3)	33.1(6)
Mn	5.2	5.0(1)	5.0(2)	4.7(1)

Comparing the EDX results before and after annealing shows a change in the matrix composition. Before annealing, the matrix composition was $Ti_{47.5}Fe_{48.4}Mn_{4.1}$ while after annealing, the matrix composition was closer to the nominal composition, and Mn only substituted for Fe. This is very close to the composition given by Fruchart et al. who found that Mn substitutes for Fe in the TiFe crystal structure [112]. In the as-atomized sample, the second phase exhibited slightly different compositions, with two distinct regions: gray and black, dispersed within the matrix. After annealing, only a black phase is dispersed into the matrix. The Ti and Fe concentrations in this region are close to the average of the gray and black regions in the as-atomized sample. However, after annealing, the Mn content in the second phase decreased compared to that in the as-atomized sample. The stoichiometry of the secondary phase is then Ti1.87Mn0.14Fe. Thus, for the TiFe matrix phase, Mn substitutes for Fe, while for the secondary Ti2Fe phase, Mn substitutes for Ti.

The X-ray Diffraction (XRD) patterns of as atomized and vacuum-annealed samples are shown in Figure 4.4. The main phase was identified as TiFe for both alloys. The peaks of the second phase could be observed in the XRD pattern after annealing, and it was identified as Ti_2Fe, which is consistent with the results of the EDS analysis. The absence of the Ti_2Fe phase in the AS sample can be attributed to the lower abundance and the thickness of this phase, which, as observed in SEM analysis, is only a fraction of a micron thick, while in the VA sample, the Ti_2Fe phase grows to a thickness of several microns.

Considering the penetration depth of X-ray, the Ti_2Fe phase diffracts weakly in the AS sample, making it undetectable in the XRD pattern.

Table 4.3 displays the phase fraction, lattice parameters, and crystallite size for each phase as determined by Rietveld refinement. For both AS and VA samples, the lattice parameter is slightly bigger than the 2.97838 (6) Å of TiFe measured by Jung et al. [113].

The annealing process also led to a noticeable increase in crystallite size and a reduction of microstrains for the TiFe phase. This growth is easily explained by recrystallization because of the annealing temperature (1200°C), which is close to the TiFe melting point (1317°C). In addition to the increase in crystallite size, a reduction in microstrains was observed. Microstrain is typically reduced during annealing, as the material's internal stresses decrease due to the reduction of defects.

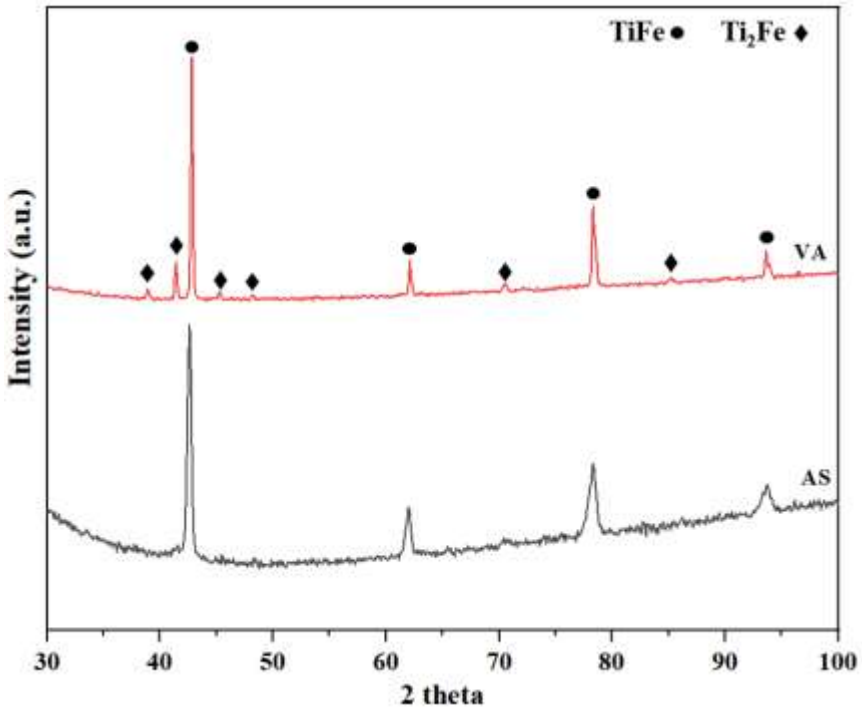

Figure 4.4 X-ray diffraction patterns of AS (as atomized) and VA (vacuum annealed) alloys.

Table 4.3. Rietveld refinement results of AS (as atomized) and VA (vacuum annealed) alloys. The error is shown in parentheses.

Sample	Phase	Phase Fraction (wt.%)	Lattice Parameter (Å)	Crystallite Size (nm)	Strain (%)
AS	TiFe	100	2.9828(4)	82(11)	0.65(3)
VA	TiFe	77 (7)	2.9884 (6)	214 (14)	0.08(3)
	Ti_2Fe	23 (7)	11.2362 (8)	140 (30)	0.2(1)

4.5.2 First Hydrogenation

The hydrogenation was performed under two different conditions: at room temperature (21°C) and 2000 kPa of hydrogen pressure and at 90°C under 4500 kPa of hydrogen. For both conditions, the experiment ran for a period of 24 hours. For both AS and VA samples, no hydrogen uptake was registered under these conditions. This could be due to the long air exposure before hydrogenation. In order to 'regenerate' the samples, they were subjected to 5 passes of cold rolling in the air. Previous studies have shown that this technique is effective in enabling the first hydrogenation of TiFe alloys. Ulate-Kolitsky et al. reported that 5 passes of cold rolling are efficient for the activation of TiFe alloys synthesized by gas atomization [42]. Manna et al. investigated the effect of air exposure on the TiFe+4 wt.% Zr alloy and they found that the seven-day air-exposed alloy did not absorb hydrogen, but cold rolling successfully led to the recovery of the alloy [94].

Figure 4.5 shows the curves of the first hydrogenation at RT/2000 kPa after 5 passes of cold rolling. The AS-5CR sample started to absorb hydrogen after about 1000 seconds and it reached the capacity of 1.56 wt.% in 24h. However, the VA-5CR sample did not

absorb hydrogen in 24 h. The fast activation of the AS-5CR sample even at RT has shown that 5 passes of cold rolling are efficient for the regeneration of atomized TiFe(Mn) alloys.

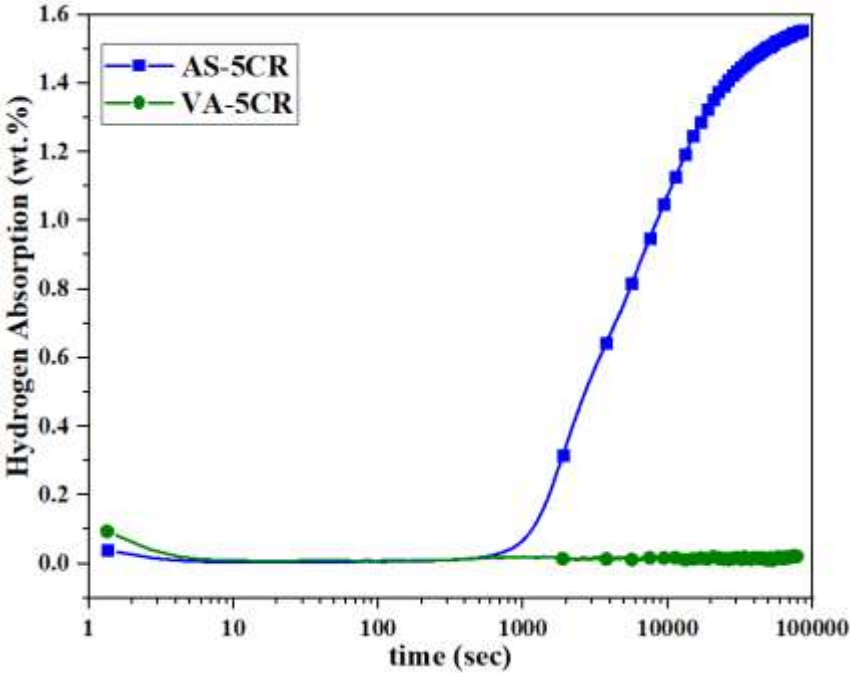

Figure 4.5 Activation curves of AS and VA samples after 5 CR at room temperature and a hydrogen pressure of 2000 kPa.

Since the VA-5CR sample did not activate at RT and 2000 kPa, the temperature was increased to 90 °C and the hydrogen pressure to 4500 kPa to investigate the effect of elevated pressure and temperature on its activation behaviour. As seen in Figure 4.6, under these conditions, both samples absorbed hydrogen. The AS-5CR sample exhibited rapid kinetics, starting hydrogen absorption within 40 seconds and reaching a capacity of 1.42 wt.% after 24 hours. In contrast, the annealed sample demonstrated a longer incubation time of 7200 seconds and finally achieved a capacity of 1.2 wt.% after 24 hours.

Based on these results, it was determined that annealing is not appropriate for the TiFe alloy studied in this work. It seems that the hydrogenation behaviour of the TiFe alloy is strongly influenced by the chemical composition and morphology of the second phase. After heat treatment, the phases' chemical composition is marginally changed but the

morphology has been drastically changed from filamentous to globular. These changes may be responsible for the longer incubation time of the VA sample. The presence of a filamentous second phase seems to facilitate the hydrogen uptake by providing nucleation points for the hydride phase and diffusion pathway for the hydrogen. After annealing, the second phase becomes more spheroidized, resulting in the reduction of pathways available for hydrogen within the alloy. This decrease in the interfacial region ultimately leads to a reduction of hydrogenation kinetic. In addition, SEM studies (Figures 2 and 3) revealed the presence of two distinct secondary regions within the TiFe matrix of the as-atomized alloy. However, after heat treatment, a dark second phase was observed in the matrix. EDS analysis (Tables 4.1 and 4.2) further confirmed compositional changes following the heat treatment. These compositional changes could potentially influence the hydrogen absorption behavior of the alloy.

Additionally, annealing also induced recrystallization in the primary TiFe phase, as evidenced by an increase in crystallite size and a reduction in microstrain determined from Rietveld refinement of XRD patterns (Table 4.3). While recrystallization reduces internal stresses, it also eliminates some of the grain boundaries that act as key diffusion pathways for hydrogen. Grain boundaries enhance hydrogen diffusion by serving as low-energy sites for hydrogen absorption and movement. The combination of reduced interfacial area in the secondary phase and a decrease in grain boundary density in the matrix likely explains the observed decline in hydrogenation performance [38,106].

Figure 4.7 presents the X-ray diffraction (XRD) patterns of the samples after cold rolling and Table 4.4 shows Rietveld refinement results. Comparing the results before and after cold rolling reveals that the cold rolling process reduced the crystallite size and increased the microstrain. Decreasing crystallite size leads to more grain boundaries. Therefore, the reduction in crystallite size and formation of a fresh surface due to crushing during cold rolling could lead to faster hydrogen absorption. The effectiveness of highly strained grain boundaries as effective trapping sites for hydrogen has been shown by Emami et al. [38]. Similarly, Lv et al. have shown that the grain boundaries formed by cold rolling could act as diffusion points for hydrogen [46].

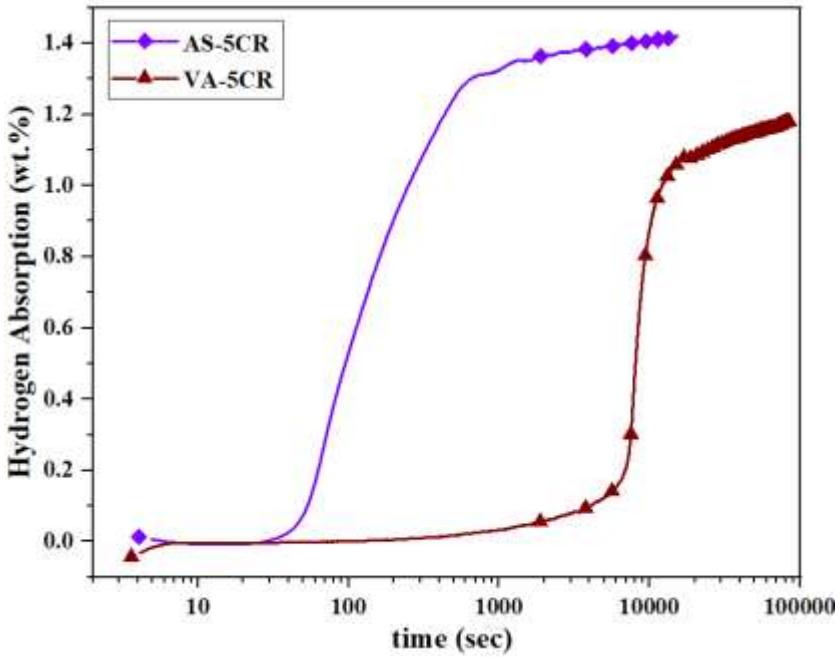

Figure 4.6 Activation curves of AS and VA samples after 5 CR at 90 ℃ and a hydrogen pressure of 4500 kPa.

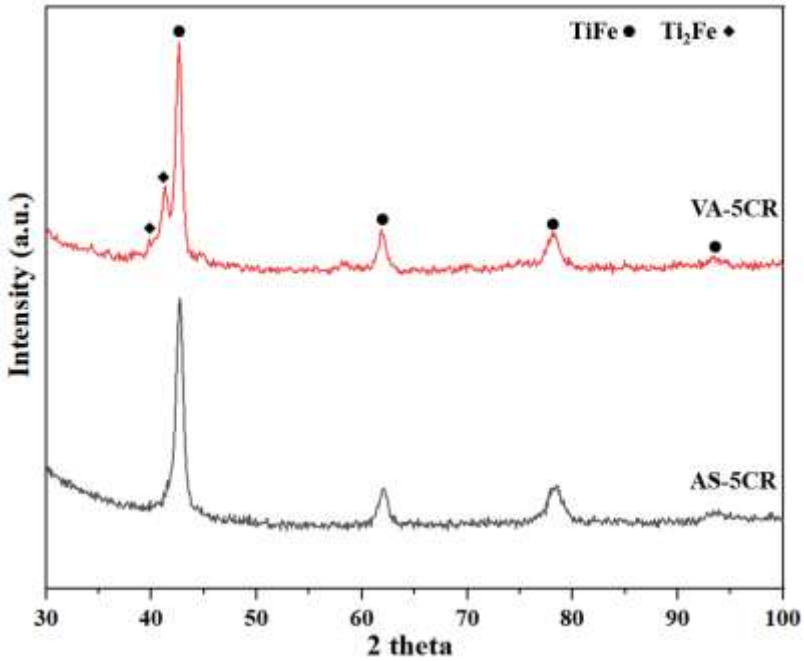

Figure 4.7 X-ray diffraction patterns of AS (as atomized) and VA (vacuum annealed) alloys after 5 passes of cold rolling.

Table 4.4 Rietveld refinement results of AS-5CR and VA-5CR. The error is shown in parentheses.

Sample	Phase	Phase Fraction Wt.%	Lattice Parameter (Å)	Crystallite Size (nm)	Strain (%)
AS-5CR	TiFe	100	2.991(2)	17(3)	1.0(6)
VA-5CR	TiFe	70 (6)	2.9900 (1)	19 (6)	0.81(8)
	Ti_2Fe	30 (6)	11.3330 (6)	10 (3)	0.10(1)

Figure 4.8 shows the X-ray diffraction (XRD) patterns of AS and VA samples after activation in 90 ℃ and 4500 kPa. The corresponding phase fractions, lattice parameters, and crystallite sizes are presented in Table 4.5. In order to preserve the hydride state, after hydrogenation at 90° C the sample was cooled to room temperature under hydrogen pressure. The diffraction pattern was registered in the air shortly after removing the sample from the sample holder. Upon analysis of the activated samples, XRD reveals the presence of TiFe, $TiFeH_{0.94,}$ and Ti_2FeH_X phases. The presence of the TiFe peak after activation in the XRD pattern indicates that the sample starts desorbing at room temperature and atmospheric pressure. TiFe phase fraction was reduced due to the presence of the orthorhombic $TiFeH_{0.94}$ phase. This phase was identified by Reidinger et al. on the desorption of TiFe hydride [114]. The lattice parameters of the $TiFeH_{0.94}$ phase presented in Table 5 are close to the lattice parameters reported by Reidinger et al.

For the VA sample, the unit cell volume of Ti_2Fe before hydrogenation is 1456 Å^3, which expands to 1803 Å^3 after hydrogenation. This corresponds to a volume expansion of 24 %. This is consistent with previous investigations by Ulate-Kolitsky et al. [41], who reported a volume expansion of 21%. The stoichiometry of the Ti_2FeH_X phase can be determined by analyzing the increase in unit cell volume resulting from hydrogen uptake. The volume increase is 347 Å^3, and there are 32 formula units per unit cell. Therefore, the

volume variation per formula unit is estimated to be about 11 Å³. Based on the assumption that the volume of a single hydrogen atom is around 2.9 Å³ [115], the resulting stoichiometry is approximately Ti_2FeH_3 (~1.9 wt.%). As this sample is made up of 20% of Ti_2FeH_3, the contribution to the total hydrogen capacity is 0.38 wt.%. The $TiFeH_{0.94}$ phase makes up 40% of the sample and contains 1 wt.% of hydrogen. Therefore, its contribution to the total capacity is 0.4 wt.% of hydrogen. Consequently, the overall hydrogen content is about 0.8 wt.%. Given the hydrogen absorption capacity of 1.2 wt.%, this shows that the sample partially desorbed before the X-ray diffraction measurement.

In the activated AS sample, assuming the Ti_2FeH_X phase has a stoichiometry of approximately Ti_2FeH_3, the 11 wt.% of this phase contributes about 0.2 wt.% hydrogen. The sample also contains 73% $TiFeH_{0.94}$, which contributes to 0.7 wt.% of hydrogen. Consequently, the total hydrogen content in the sample is 0.9 wt.%. Considering the hydrogen absorption capacity of 1.4 wt.% (Figure 6), the amount of desorbed hydrogen is 0.5 wt.%. It should be pointed out that the desorbed capacity of the VA and AS samples are almost the same, respectively 0.4 wt% and 0.5 wt.%.

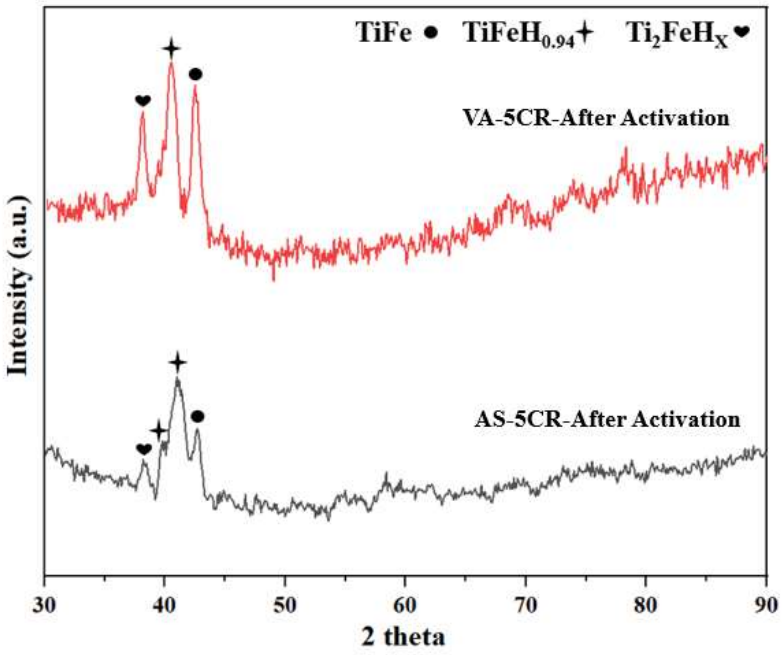

Figure 4.8 X-ray diffraction patterns of AS (as atomized) and VA (vacuum annealed) after activation.

Table 4.5 Rietveld refinement results of AS (as atomized) and VA (vacuum annealed) after activation. The error is shown in parentheses.

Sample	Phase	Phase fraction (%)	Lattice Parameter (Å)	Crystallite Size (nm)
AS-5CR-After Activation	$TiFeH_{0.94}$	73(11)	a=4.37(1) b=3.08(1) c=4.52 (1)	11(2)
	Ti_2FeHx	11(5)	12.23(2)	17(5)
	TiFe	16(8)	2.994(4)	20 (3)
VA-5CR-After Activation	$TiFeH_{0.94}$	40(13)	a=4.51 (1) b=3.11(1) c=4.40(3)	15(4)
	Ti_2FeH_x	20(6)	12.17(2)	22(7)
	TiFe	40(13)	2.986(5)	16 (5)

4.6 Conclusion

- The microstructure and first hydrogenation of $Ti_{48.8}Fe_{46.0}Mn_{5.2}$ alloy prepared by gas atomization, before and after vacuum annealing, have been investigated.

- The microstructure of the alloy before and after annealing consists of a TiFe matrix and a secondary Ti_2Fe-like phase. The secondary Ti_2Fe phase exhibited a filamentous microstructure in the atomized alloy, whereas it appeared more globular in the annealed sample.

- Both atomized and annealed alloys needed prior mechanical processing by cold rolling to absorb hydrogen. After 5 cold rolling passes, the atomized sample absorbed 1.56 wt.% hydrogen at room temperature and hydrogen pressure of 2000 kPa.

However, the annealed sample could not be activated in 24 hours under the same conditions.

- Both atomized and annealed samples absorbed hydrogen at 90ºC and hydrogen pressure of 4500 kPa but the atomized sample had faster kinetic and higher capacity.

- Annealing after atomization had a negative effect on the activation process, probably due to recrystallization and changes in the microstructure.

- X-ray analysis identified the main phases as TiFe, $TiFeH_{0.94}$, and Ti_2FeH_x after activation. Considering the volume expansion of the Ti_2Fe phase upon hydrogenation, the resulting stoichiometry is approximately Ti_2FeH_3.

CHAPTER V.

ACTIVATION ENERGY AND KINETICS OF FIRST HYDROGENATION IN $Ti_{0.488}Fe_{0.460}Mn_{0.052}$ ALLOY PRODUCED BY GAS ATOMIZATION

This chapter presents a systematic experimental investigation of the first hydrogenation behaviour of a gas-atomized $Ti_{48.8}Fe_{46.0}Mn_{5.2}$ alloy, with a particular focus on the activation energy measurement. Because the as-atomized powder exhibited no hydrogen absorption due to oxidation during air exposure, cold rolling in air was employed as a practical activation strategy to introduce cracks and surface defects that facilitate hydrogen diffusion. The effects of temperature, hydrogen pressure, and constant driving force on the incubation time were examined, revealing that the first hydrogenation follows an Arrhenius-type mechanism. Furthermore, the pre-exponential factor was found to be pressure dependent.

5.1 Content of Article

Chapter V's content was published in *inorganics* Journal, Volume 14, Issue 2 on February 17, 2026. The article is accessible at: https://doi.org/10.3390/inorganics14020062.

Activation Energy and Kinetics of First Hydrogenation in $Ti_{48.8}Fe_{46.0}Mn_{5.2}$ Alloy Produced by Gas Atomization

Authors: Seyedehfaranak Hosseinigourajoubi [1], Chris Schade [2] and Jacques Huot [1,*]

[1] Hydrogen Research Institute, Université du Québec à Trois-Rivières, Trois-Rivières, QC G9A5H7, Canada; Seyedeh.Faranak.Hosseini.Gourajoubi@uqtr.ca

[2] GKN Hoeganaes Innovation Centre & Advanced Materials – New Jersey, USA; Chris.Schade@hoeganaes.com

* Correspondence: jacques.huot@uqtr.ca

5.2 Abstract

The first hydrogenation behavior of the gas atomized $Ti_{48.8}Fe_{46.0}Mn_{5.2}$ alloy was systemically investigated. The as-received powder showed no hydrogen absorption due to the long air exposure before the hydrogenation tests. To overcome this, 5 passes of cold rolling were employed as an activation strategy. Cold rolling introduced cracks and defects that facilitated hydrogen diffusion, enabling the alloy to successfully absorb hydrogen. The influences of temperature, constant driving force, and hydrogen pressure on the first hydrogenation were evaluated. The results indicated that the first hydrogenation follows an Arrhenius behavior ($k = Ae^{-\frac{E_A}{RT}}$), and average activation energy was calculated as 71 kJ/mol H_2. The pre-exponential factor (A) was found to be pressure-dependent, following the equation $A = A_0 (P/P_0)^{1.8}$, where $A_0 = 2.6 \times 10^6$ s^{-1}.

Keywords: TiFe alloy; Metal hydride; First hydrogenation; Activation energy; Arrhenius mechanism

5.3 Introduction

Hydrogen, as an energy vector, offers a sustainable alternative to fossil fuels, addressing global challenges like climate change and rising energy demand [2]. Its high gravimetric energy density, significantly higher than that of conventional fuels, makes it an attractive option for many practical applications. However, developing efficient storage systems remains critical for the widespread usage of hydrogen [1,14,116].

Hydrogen is mainly stored in three primary forms: as a compressed gas, cryogenic liquid, or solid-state material. Compressed and liquid hydrogen storage face challenges such as high pressure, cryogenic temperature, and high costs. Solid-state in the form of metal hydrides could potentially provide safe storage with high volumetric density under relatively mild temperature and pressure conditions [4,5,116]. Solid-state storage involves the storage of hydrogen, either on the surface of solids through Van der Waals interactions or within solids, by forming chemical bonds with the metal atoms to form metal hydrides [117,118].

Among metal hydrides, TiFe-based alloys are promising materials for hydrogen storage due to their abundance, low cost, and good reversibility during hydrogen absorption and desorption [36,47,119,120]. The TiFe alloy is a well-known AB-type intermetallic compound capable of storing approximately 1.86 wt% of hydrogen, first reported by Reilly and Wiswall in 1974 [33].

A major limitation of TiFe alloys is their first hydrogenation kinetics. During air exposure, a surface oxide layer is naturally formed which acts as a barrier for hydrogen diffusion into the alloy. As a result, when TiFe alloy is exposed to hydrogen, a certain time is needed for penetration of hydrogen into the alloy and reaction with metal atoms. This period is known as the incubation time. Once this barrier is overcome, the hydrogenation can proceed [44,121].

To break the oxide layer, and starting the hydrogen absorption reaction, Reilly and Wiswall used the method of heating the alloy to 400°C, followed by cooling and applying a high hydrogen pressure of approximately 60 bars [33]. This process had to be repeated several times until the alloy could be fully hydrided. This method has since been widely used in numerous studies on TiFe alloys [122,123].

Adding transition elements such as Zr [45,46], Mn [32,43,88], Cr [32,47], and Y [124] can significantly improve the first hydrogenation kinetics by promoting the formation of secondary phases that facilitate hydrogen diffusion. Mechanical deformation techniques like ball milling [38,125], cold rolling [6,42], and high-pressure torsion [126] are also beneficial for improving first hydrogenation kinetics by creating grain boundaries and cracks, which act as pathways for hydrogen to penetrate the oxide layer. Furthermore, several studies have shown that powder processing methods like gas atomization could enhance the first hydrogenation properties of TiFe-based alloys by producing a finer microstructure [42,127,128]. Ulate-Kolitsky et al. compared alloys synthesized by gas atomization and induction melting, concluding that gas atomization resulted in a much finer microstructure and a TiFe matrix with a more refined distribution of secondary phases [42].

Previous research has indicated that the hydrogen absorption process generally follows an Arrhenius mechanism, and there have been attempts to calculate the activation energy of metal hydride formation in these alloys [43,129-132]. Bowman and Tadlock [131] investigated the hydrogen diffusion rate in TiFeH phase using nuclear magnetic resonance (NMR) techniques, and the temperature dependence of the proton relaxation rate suggested Arrhenius behavior, leading to the calculation of activation energy as 31.8 kJ/mol. Chung and Lee [132] demonstrated that hydrogen absorption kinetics of TiFe alloys improve with partial substitution of Mn and Ni for Fe. They found that the hydriding rate depends on the difference between the applied pressure and the equilibrium pressure, and from Arrhenius plots of the rate constants versus 1/T, they calculated the activation energies to be 33.5 kJ/mol for TiFe, 32.6 kJ/mol for $TiFe_{0.85}Mn_{0.15}$, and 31.8 kJ/mol for $TiFe_{0.9}Ni_{0.1}$.

The above-mentioned studies calculated the activation energy associated with hydrogen absorption after the alloy had already hydrogenated, and the incubation stage caused by the surface oxide layer was no longer present. However, the first hydrogenation where the oxide is broken is critical as it can significantly influence the cost and efficiency of metal hydride formation. In the present study, we systematically investigate the first hydrogenation behavior of a TiFe-based alloy ($Ti_{48.8}Fe_{46.0}Mn_{5.2}$) produced by gas atomization. This composition was selected because Mn substitution could promote the formation of secondary phases that facilitate hydrogen diffusion [32,43,88]. Unlike previous works, which focused only on alloys that were already subjected to a few hydrogenation/dehydrogenation steps, this study focus on the first hydrogenation. The effects of temperature, constant driving force, and hydrogen pressure on the incubation time of the first hydrogenation was investigated. To our knowledge, this is the first systematic investigation of how working conditions influence the first hydrogenation of a TiFe-based alloy.

5.4 Materials and Methods

The gas-atomized alloy, with an atomic composition of 48.8 Ti, 46.0 Fe, and 5.2 Mn, was provided by GKN Hoeganaes Innovation Centre and Advanced Materials. Gas atomization was carried out by GKN under pure argon using a VIGA-type furnace equipped with a free-fall atomization ring set-up. Following synthesis, the powder was stored in the air.

The atomized powder was subjected to five cold rolling passes before hydrogenation. Cold rolling was performed vertically in the air using a modified Durston DRM 130 rolling mill (High Wycombe, Buckinghamshire, UK). The powder was inserted between two 316 stainless steel plates to prevent contamination of the powder by the rollers.

The powder morphology before and after cold rolling was examined using a Hitachi SU1510 scanning electron microscope (SEM) (Hitachi High-Tech Canada, Toronto, ON, Canada).

The hydrogenation tests were carried out using a homemade Sievert's apparatus. The measurements were conducted under various pressures ranging from 15 bars to 50 bars at temperatures of 298 K, 308 K, 318 K, and 328 K. Each hydrogenation test was conducted on about one gram of fresh sample. The samples were evacuated for 15 minutes at room temperature prior to kinetic measurements. The volume of chamber was 44 cm^3.

5.5 Results and Discussion

The microstructure, crystal structure, and first hydrogenation of $Ti_{48.8}Fe_{46.0}Mn_{5.2}$ alloy were reported in our earlier paper [133]. It was found that the microstructure consisted of a main TiFe matrix and a filamentous Ti_2Fe-like phase. The main TiFe phase exhibited a BCC crystal structure with a lattice parameter of 2.9828 ± 0.0004 Å.

As reported in our previous study, the as-received atomized $Ti_{48.8}Fe_{46.0}Mn_{5.2}$ alloy was unable to absorb hydrogen under two different test conditions: (i) at room temperature under 20 bars H_2 pressure, and (ii) at 363 K under 45 bars H_2. To activate the alloy, it was subjected to five passes of cold rolling (5CR) in the air. After cold rolling, the obtained flakes and powders were manually crushed in air into powder using a hardened steel mortar and pestle. The resulting powder had a particle size distribution ranging from 45 to 212 μm. This obtained powder was subsequently used for the hydrogenation tests. The 5CR alloy successfully absorbed hydrogen under both above-mentioned testing conditions. Given that cold rolling in air successfully activated the material, and considering industrial collaboration of the research and the practical convenience of cold rolling in air, all further cold rolling steps were conducted in air.

Figure 5.1 presents the morphology of the as-received and cold-rolled powders. A reduction in particle size is evident after cold rolling, along with the formation of cracks

on the powder surfaces. As shown in Figure 5.1.a, a combination of spherical and non-spherical particles was observed in the atomized powder. The spherical particles have a size distribution from 20 µm up to 300 µm, while non-spherical particles fall within the 100–400 µm range. Figure 5.1.c shows that after five passes of cold rolling, the average particle size decreased significantly. Most particles were reduced to below 20 µm, although some larger particles (~100 µm) remained. In addition to the decrease in particle size, cold rolling introduced numerous cracks and surface defects which are clearly visible under the higher magnification of figure 5.1.d. These morphological changes, including particle size reduction and the formation of cracks and defects, enhance hydrogen diffusion and facilitate hydrogen absorption. This effect has been observed in other alloys such as TiFe [42,94,134], $LaNi_5$ [135], Mg [136,137], and high-entropy alloys [138].

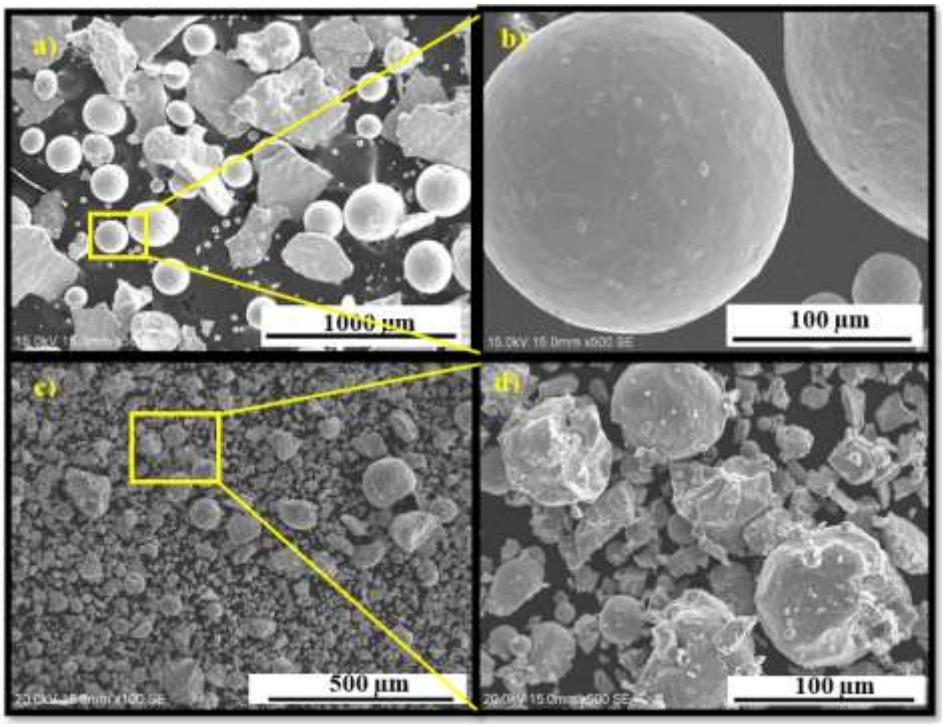

Figure 5.1 Morphology of gas atomized $Ti_{48.8}Fe_{46.0}Mn_{5.2}$ (a, b), and after 5 cold rolling passes (c, d).

After finding that five passes of cold rolling effectively regenerate the $Ti_{48.8}Fe_{46.0}Mn_{5.2}$ alloy for hydrogen absorption, the next step was to evaluate the first

hydrogenation parameters systematically. Therefore, in the following sections, we investigate the effects of temperature, constant driving force, and hydrogen pressure on the first hydrogenation behavior. To prepare the alloy for hydrogen absorption, all kinetic experiments were conducted on samples subjected to 5 cold rolling passes prior to each test.

5.5.1 Effect of temperature on first hydrogenation of $Ti_{48.8}Fe_{46.0}Mn_{5.2}$ -5CR

The effect of temperature on the first hydrogenation was investigated by measuring the incubation time at 298 K, 308 K, 318 K, and 328 K under a hydrogen pressure of 40 bars. Figure 5.2 shows the first hydrogenation kinetics of the of $Ti_{48.8}Fe_{46.0}Mn_{5.2}$ -5CR alloy at different temperatures under a hydrogen pressure of 40 bars. We see that the incubation time decreases with increasing temperature from approximately 3000 s at 298 K to 330 s at 328 K.

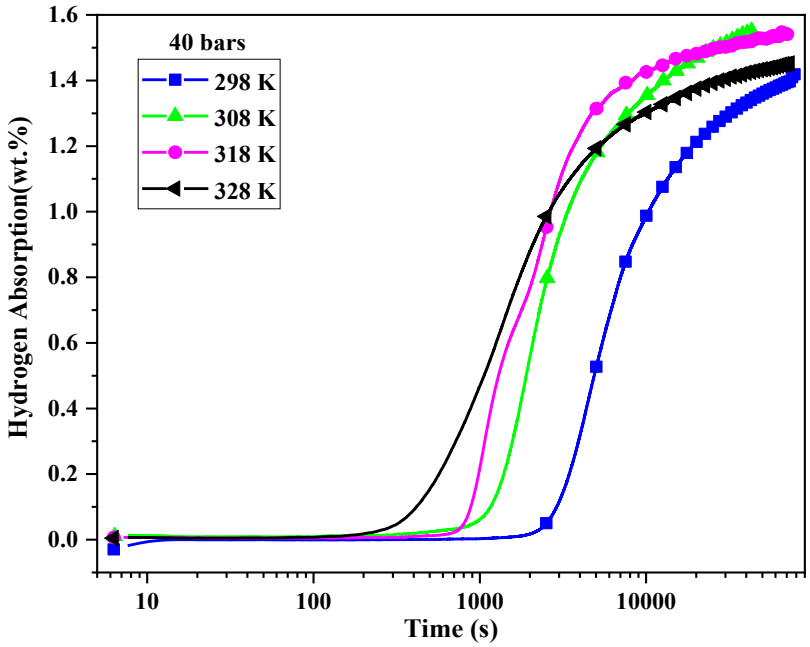

Figure 5.2 First hydrogenation curves of $Ti_{48.8}Fe_{46.0}Mn_{5.2}$ -5CR alloy at 298 K, 308 K, 318 K, and 328 K under a hydrogen pressure of 40 bars.

The fact that incubation time varies with temperature indicates that the process may follow an Arrhenius-type behavior. The Arrhenius equation describes the relationship between the rate of a chemical reaction and temperature, and is expressed as:

$$k = Ae^{-\frac{E_A}{RT}} \tag{5.1}$$

Where:

k is the rate constant of the chemical reaction,

A is the pre-exponential factor or Arrhenius factor, a constant related to the frequency of collisions of reacting molecules (s^{-1}),

E_a is the activation energy for the reaction (J/mol),

R is the universal gas constant (8.314 J/(mol K)),

T is the absolute temperature (K).

Since incubation time (t) is inversely proportional to the rate constant:

$$t \sim \frac{1}{k} \tag{5.2}$$

Then, equation (5.1) could be written as:

$$\ln t = -\ln A + \frac{E_a}{RT} \quad (5.3)$$

In Figure 5.3, ln t is plotted as a function of 1000/T. From the slope of the fitted line, the activation energy is calculated to be E_a = 69 ± 1 kJ/mol H_2. Additionally, from the intercept, A is 2.6 × 10^8 s^{-1} with a range from 1.6 × 10^8 to 4.2 × 10^8 s^{-1}.

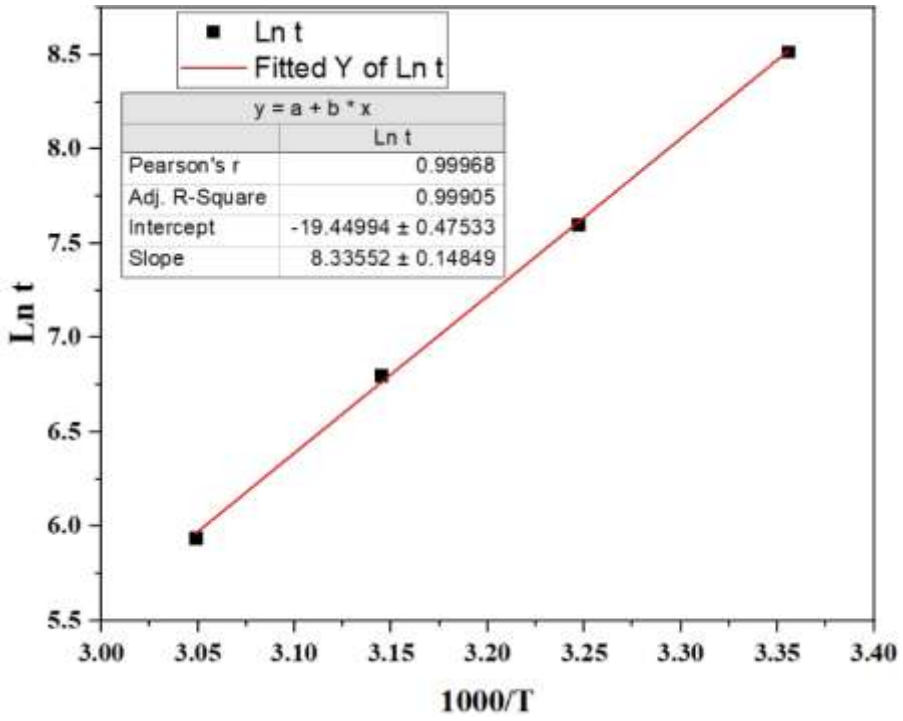

Figure 5.3 Plot of ln t (incubation time) as a function of 1000/T (T: temperature) for activation of $Ti_{48.8}Fe_{46.0}Mn_{5.2}$ -5CR at 298 K, 308 K, 318 K and 328 K under hydrogen pressure of 40 bars.

5.5.2 First hydrogenation behavior under a constant driving force

In hydrogen absorption reactions, the difference between the applied pressure and the hydrogenation equilibrium pressure is defined as the driving force, which controls the reaction rate. Driving force can be characterized using the Rudman's expression [139]:

$$c = T(1 - \sqrt{P/P_e}) \quad (5.4)$$

Where c is the driving force, T is the temperature, P is the applied pressure, and P_e is the equilibrium pressure of the reaction. For the calculation we used the literature thermodynamic values of the closely related composition $Ti_1Fe_{0.9}Mn_{0.1}$ [140].

A higher C value indicates a stronger driving force for the hydrogen absorption reaction. In these experiments, the driving force was maintained constant as C=175, and the hydrogen absorption tests were carried out at 298, 308, 318, and 328 K. The corresponding pressures were calculated as 15, 20, 27 and 35 bars, respectively. The results are shown in Figure 5.4.

The incubation time is plotted as a function of 1000/T in Figure 5.5 to determine whether the Arrhenius mechanism is still applicable. The linear fit demonstrates that the incubation time still obeys an Arrhenius law. The fitted slope yields an activation energy of $E_a = 72 \pm 4$ kJ/mol H_2. The intercept reveals the pre-exponential factor (A) as 1.3×10^9 s^{-1}, with a range from 3.2×10^8 to 5.8×10^9 s^{-1}.

The activation energies obtained under constant pressure and constant driving force conditions overlap and fall within the same range. This observation suggests that the activation energy is an intrinsic property of the alloy and essentially constant across different testing conditions.

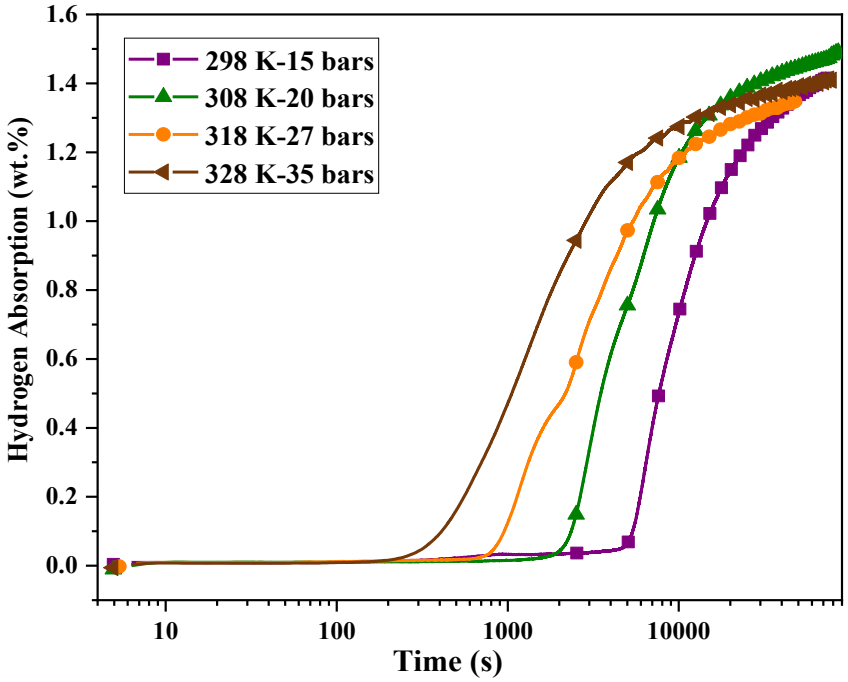

Figure 5.4 Activation curves under constant driving force for $Ti_{48.8}Fe_{46.0}Mn_{5.2}$ -5CR alloy.

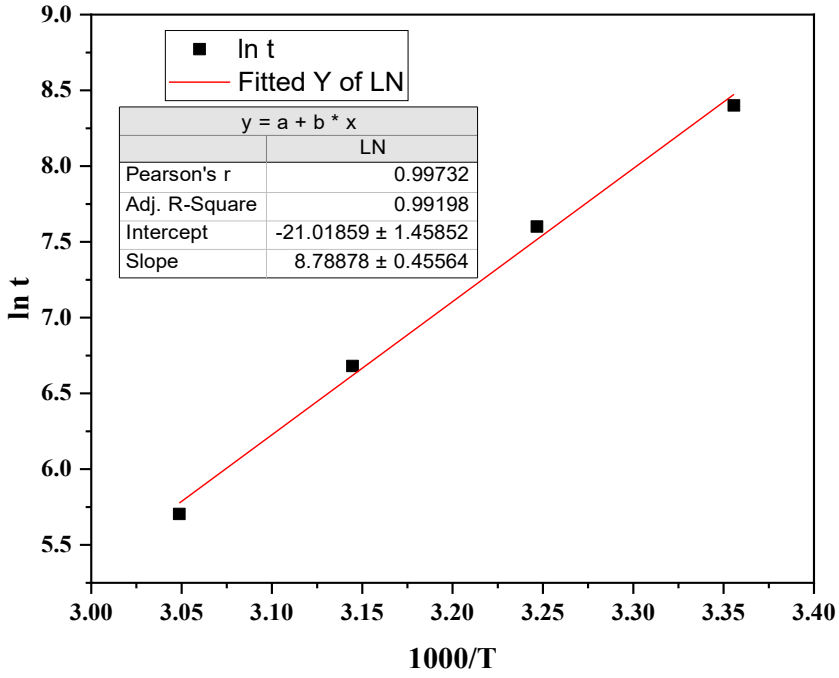

Figure 5.5 Plot of ln t (incubation time) as a function of 1000/T (T: temperature) for activation under constant driving force.

Regarding the pre-exponential factor (A), it represents the number of interactions per second, and obviously, this is pressure dependent. For practical applications, it is important to have the pressure dependence of this factor because it will give the range of pressures required to have a reasonable incubation time. In a previous investigation on $LaNi_5$ alloy, it was also reported that the pre-exponential factor is pressure-dependent [141].

The dependency of A on pressure can be expressed as:

$$A = A_0 \left(P/P_0\right)^x \tag{5.5}$$

Here, A_0 and x are constants, P represents the applied hydrogen pressure, and P_0=1 bar.

5.5.3 Effect of pressure on first hydrogenation behavior

To study the effect of pressure on the pre-exponential factor, the first hydrogenation was performed at 298 K under 20, 30, 40, and 50 bars of hydrogen pressure. The hydrogenation curves are shown in Figure 5.6. With increasing pressure, the incubation time decreased. The variation of ln t as a function of ln P/P_0 is shown in Figure 5.7.

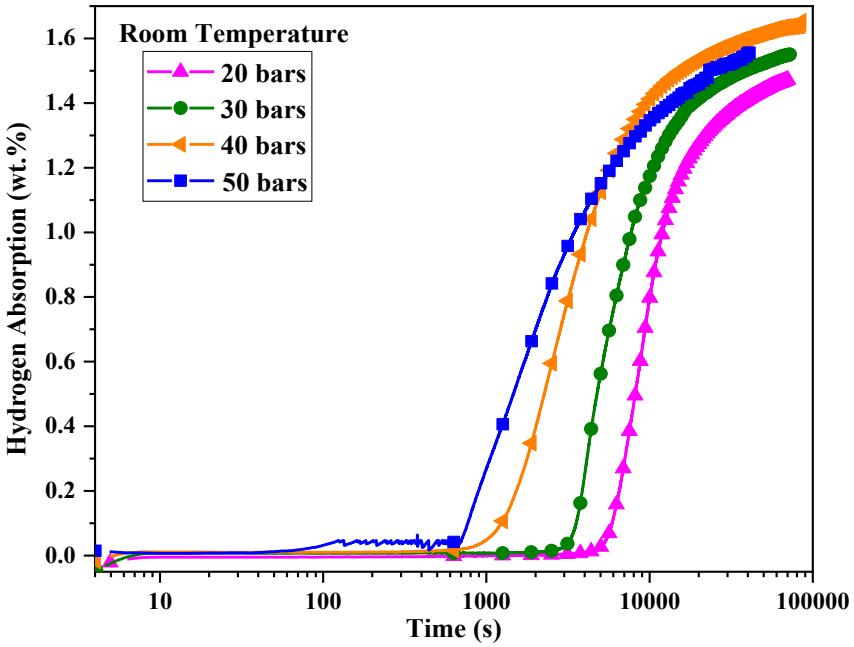

Figure 5.6 First hydrogenation curves at room temperature under 20, 30, 40, and 50 bars of hydrogen pressure.

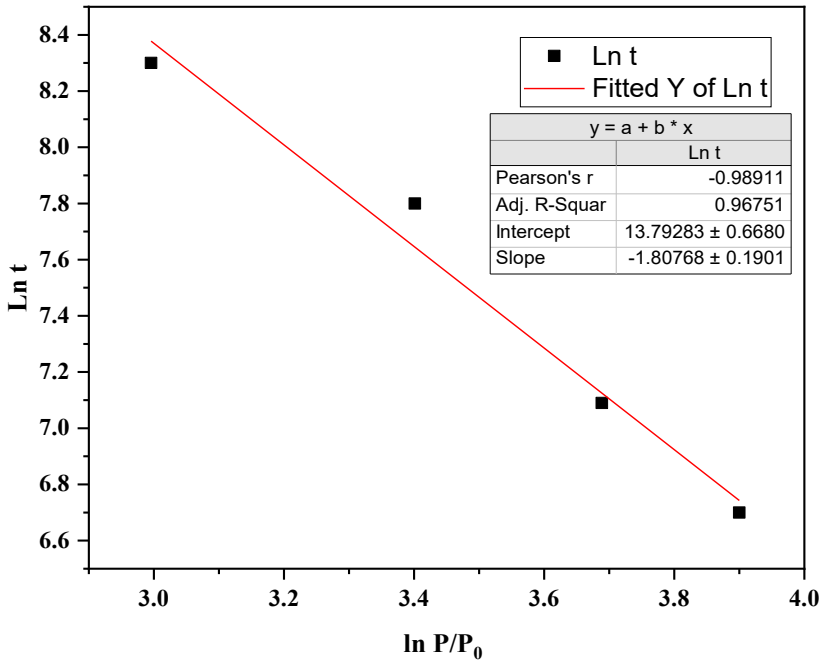

Figure 5.7 Plot of ln t as a function of ln P/P0, where t is the incubation time, and P is the pressure.

Considering equation 5.5, equation 5.3 can be written as:

$$\ln t = \frac{E_a}{RT} - \ln A_0 - x \ln\left(P/P_0\right) \tag{5.6}$$

From the fitted slope of Figure 5.7, x = 1.8 ± 0.2, therefore, the dependence of pre-exponential factor (A) to applied pressure can be expressed as:

$$A = A_0 \left(P/P_0\right)^{1.8} \tag{5.7}$$

From the intercept value of Figure 5.7:

$$13.8 = \frac{E_a}{RT} - \ln A_0 \tag{5.8}$$

Taking the average activation energy as 71 kJ/mol, A_0 is calculated to be $2.6\times10^{6} s^{-1}$.

In summary, the activation energy for the first hydrogen absorption, calculated under both constant pressure and constant driving force conditions, remains essentially constant within the experimental error, with an average value of 71 kJ/mol. The pre-exponential factor (A) shows the dependence of the incubation time on the pressure, which follows the relationship $A = A_0 \left(P/P_0\right)^{1.8}$, where $A_0 = 2.6\times10^{6}\ s^{-1}$.

The activation energy reported in the literature have been on samples that were subjected to many hydrogenation/dehydrogenation cycles. Bowman and Tadlock [131] prepared TiFeH by performing several hydriding–dehydriding cycles between room temperature and 400 °C. By using nuclear magnetic resonance (NMR) techniques, they observed that the proton relaxation rate exhibited Arrhenius-type temperature dependence.

From the slope of their plot, they determined an activation energy of 31.8 kJ/mol, which is less than the activation energy found in our study. The activation energy reported by Bowman and Tadlock refers to the hydrogenation cycles after the material had been fully activated. Our study specifically focuses on the first hydrogenation process**,** which includes both the activation energy for hydrogen absorption and the additional activation energy required for the incubation process**.** Furthermore, Bowman and Tadlock's study [131] measured the activation energy of TiFe alloys without elemental substitution, whereas manganese (Mn) was partially substituted for iron (Fe) in the present study.

On the other hand, several studies have shown that Mn substitution facilitates hydrogen absorption kinetics but does not significantly affect the activation energy [43,132]. Chung and Lee [132] prepared TiFe and $TiFe_{0.85}Mn_{0.15}$ alloys by arc melting and activated them through heat treatment at 400 °C under hydrogen atmosphere, followed by hydrogen absorption–desorption cycles at room temperature. They found that, for both alloys, the hydrogenation rate was proportional to the difference between the applied pressure and the equilibrium pressure, and it also followed an Arrhenius relationship. From their analysis, they measured activation energies of 33.5 kJ/mol for TiFe and 32.6 kJ/mol for $TiFe_{0.85}Mn_{0.15}$. Similarly, Padhee et al. [43] employed Density Functional Theory (DFT) calculations to estimate the activation energy of TiFe and $TiFe_{0.875}Mn_{0.125}$, reporting values of 32.6 kJ/mol and 33.3 kJ/mol, respectively. These results also show that Mn substitution causes minimal changes in the activation energy.

Zeaiter et al. [142] reported an activation energy of 19.43 ± 2.52 kJ/mol for $TiFe_{0.9}Mn_{0.1}$ after 12 absorption/desorption cycles, which is significantly lower than most values reported in the literature. This low activation energy may be attributed to the thermochemical treatment applied prior to the activation process, which involved heating the sample at 400 °C under 32 bar of hydrogen for 24 h in a reactor cell. Compared with the as-received powder, which exhibited an incubation time of approximately 6000 min, the thermochemically treated powder showed a much shorter incubation time of 1595 min. Unfortunately, the activation energy of the as-received powder was not reported, so a direct comparison between the two states is not possible.

Bakulin et al. [143] calculated an activation energy of 59 kJ/mol for TiFe using density functional theory (DFT). They reported that the addition of dopant elements slightly reduces the activation energy; for example, the substitution of 5 at.% Mn decreased the activation energy to 58 kJ/mol.

Overall, the literature consistently reports activation energies lower than those in our study. The reason is that they evaluated the activation energy of the hydrogen absorption reaction after the first hydrogenation had occurred, without considering incubation time in first hydrogen absorption cycle. In contrast, our study measured the activation energy for both the incubation stage and hydrogen absorption. It is thus reasonable that the activation energy measured here is bigger than the activation energy reported in the literature, as it includes the activation energy needed to break the oxide layer on the particle's surface, plus the hydrogenation activation energy.

5.6 Conclusions

In this study, the first hydrogenation behavior of $Ti_{48.8}Fe_{46.0}Mn_{5.2}$ alloy, synthesized via gas atomization, was investigated. It was found that the as-atomized alloy could not absorb hydrogen due to air exposure; however, after five passes of cold rolling in air, the alloy was successfully regenerated.

The effects of temperature, constant driving force, and hydrogen pressure on the first hydrogenation were studied. It was observed that increasing the temperature and pressure reduced the incubation time required for hydrogen absorption. Analysis of the kinetics data confirmed that the first hydrogenation follows an Arrhenius-type mechanism, with an average activation energy of 71 kJ/mol H_2. This value reflects the activation energy for both the incubation stage, associated with breaking the oxide layer, and the hydrogen absorption process, and is higher than the average activation energies reported in previous studies, which were determined after the alloys had already undergone the first hydrogenation.

The effect of pressure on the pre-exponential factor (A) was found to vary as $A=A_0(P/P_0)^{1.8}$, where A_0 equals 2.6×10^6 s^{-1}. These findings provide important insights for optimizing the first hydrogenation of TiFe-based alloys for hydrogen storage applications.

CHAPTER VI.

CONCLUSION

In this thesis, the influence of microstructure, morphology, and processing routes on the first hydrogenation of gas-atomized $Ti_{0.488}Fe_{0.460}Mn_{0.052}$ alloy was systematically investigated. The as-atomized alloy did not absorb hydrogen, most likely due to prolonged air exposure, which resulted in the formation of a passivating surface layer. This finding demonstrates that, despite Fe substitution by Mn and the use of gas atomization, the alloy cannot be directly activated without additional treatments. From an industrial perspective, considering the higher production cost of gas atomization, relying solely on this method is insufficient. Combining gas atomization with strategies such as cold rolling, or adjusting the Mn content, may improve direct activation efficiency.

Mechanical deformation methods, including cold rolling, ball milling, and cold pressing, were found to be effective activation routes, as they introduced defects, refined crystallites, and increased grain boundary density, collectively enhancing room-temperature hydrogenation kinetics. Among these methods, cold rolling was identified as particularly attractive for industrial applications due to its lower cost and greater accessibility. Notably, while TiFeMn alloys could be activated using these methods, pure TiFe alloys could not be activated by simple cold rolling in air. Additionally, gas-atomized alloys demonstrated superior activation behavior compared to conventionally melted alloys after mechanical treatment, highlighting the industrial relevance of this approach.

Our results further showed that increasing the number of cold rolling passes beyond five hindered hydrogen absorption, indicating that minimizing mechanical treatment is advantageous for both energy and time efficiency while still achieving effective activation. The rolling atmosphere also played a critical role. Rolling under argon significantly

improved hydrogenation behavior compared to rolling in air, whereas annealing negatively affected activation by altering the microstructure and reducing hydrogen diffusion pathways. These findings provide practical guidance for industrial processing, enabling more energy-efficient and time-saving activation strategies.

Looking forward, several directions for future work emerge from this study. Investigating a wider compositional range, including varying Mn contents or substitutions with elements such as Al, Cu, Zr, and Ni, could potentially enable direct activation after atomization, eliminating the need for additional mechanical or thermal treatments. Such compositional optimization would reduce production costs and facilitate large-scale industrial implementation.

Furthermore, a deeper understanding of surface and activation mechanisms is needed. Detailed surface characterization, including analysis of defects, crack depth, and morphology, could provide insights into how these features influence hydrogen absorption and whether the material retains activity after air exposure. A systematic study of air exposure duration would also help establish optimal handling, storage, and transportation protocols, ensuring that the alloy maintains hydrogenation performance under industrial conditions.

Finally, evaluating the hydrogen desorption behavior, reversible storage capacity, and long-term cycling stability of the alloy is essential to fully assess its potential for practical hydrogen storage applications. Collectively, these studies would provide a more comprehensive understanding of the first hydrogenation behavior of TiFe-based alloys and guide the optimization of alloy compositions and processing methods for industrial use, ultimately contributing to the development of efficient and cost-effective hydrogen storage systems.

REFERENCES

1. Dincer, I. Renewable energy and sustainable development: a crucial review. *Renewable and Sustainable Energy Reviews* **2000**, *4*, 157–175, doi:https://doi.org/10.1016/S1364-0321(99)00011-8.
2. Lu, X.; Krutoff, A.-C.; Wappler, M.; Fischer, A. Key influencing factors on hydrogen storage and transportation costs: A systematic literature review. *International Journal of Hydrogen Energy* **2025**, *105*, 308–325, doi:https://doi.org/10.1016/j.ijhydene.2025.01.196.
3. Liu, Z.; Xie, J.; Song, C.; Yang, X.; Kalogirou, S.A. A review of hydrogen production through solar energy with various energy storage devices. *International Journal of Hydrogen Energy* **2025**, doi:https://doi.org/10.1016/j.ijhydene.2025.01.274.
4. Von Colbe, J.B.; Ares, J.-R.; Barale, J.; Baricco, M.; Buckley, C.; Capurso, G.; Gallandat, N.; Grant, D.M.; Guzik, M.N.; Jacob, I. Application of hydrides in hydrogen storage and compression: Achievements, outlook and perspectives. *international journal of hydrogen energy* **2019**, *44*, 7780–7808.
5. Greene, D.L.; Ogden, J.M.; Lin, Z. Challenges in the designing, planning and deployment of hydrogen refueling infrastructure for fuel cell electric vehicles. *eTransportation* **2020**, *6*, 100086, doi:https://doi.org/10.1016/j.etran.2020.100086.
6. Vega, L.; Leiva, D.; Neto, R.L.; Silva, W.; Silva, R.; Ishikawa, T.; Kiminami, C.; Botta, W. Mechanical activation of TiFe for hydrogen storage by cold rolling under inert atmosphere. *international journal of hydrogen energy* **2018**, *43*, 2913–2918.
7. Züttel, A. Hydrogen storage methods. *Naturwissenschaften* **2004**, *91*, 157–172, doi:10.1007/s00114-004-0516-x.
8. Bosu, S.; Rajamohan, N. Recent advancements in hydrogen storage - Comparative review on methods, operating conditions and challenges. *International Journal of Hydrogen Energy* **2024**, *52*, 352–370, doi:https://doi.org/10.1016/j.ijhydene.2023.01.344.
9. Valenti, G. 2 - Hydrogen liquefaction and liquid hydrogen storage. In *Compendium of Hydrogen Energy*, Gupta, R.B., Basile, A., Veziroğlu, T.N., Eds.; Woodhead Publishing: 2016; pp. 27–51.
10. Yang, F.; Wang, J.; Zhang, Y.; Wu, Z.; Zhang, Z.; Zhao, F.; Huot, J.; Grobivć Novaković, J.; Novaković, N. Recent progress on the development of high entropy alloys (HEAs) for solid hydrogen storage: A review. *International Journal of Hydrogen Energy* **2022**, *47*, 11236–11249, doi:https://doi.org/10.1016/j.ijhydene.2022.01.141.
11. Callini, E.; Aguey-Zinsou, K.-F.; Ahuja, R.; Ares, J.R.; Bals, S.; Biliškov, N.; Chakraborty, S.; Charalambopoulou, G.; Chaudhary, A.-L.; Cuevas, F.; et al. Nanostructured materials for solid-state hydrogen storage: A review of the achievement of COST Action MP1103. *International Journal of Hydrogen Energy* **2016**, *41*, 14404–14428, doi:https://doi.org/10.1016/j.ijhydene.2016.04.025.
12. Kaur, M.; Pal, K. Review on hydrogen storage materials and methods from an electrochemical viewpoint. *Journal of Energy Storage* **2019**, *23*, 234–249, doi:https://doi.org/10.1016/j.est.2019.03.020.
13. Darkrim, F.L.; Malbrunot, P.; Tartaglia, G.P. Review of hydrogen storage by adsorption in carbon nanotubes. *International Journal of Hydrogen Energy* **2002**, *27*, 193–202, doi:https://doi.org/10.1016/S0360-3199(01)00103-3.

14. Umar, A.A.; Hossain, M.M. Hydrogen storage via adsorption: A review of recent advances and challenges. *Fuel* **2025**, *387*, 134273, doi:https://doi.org/10.1016/j.fuel.2024.134273.
15. Niaz, S.; Manzoor, T.; Pandith, A.H. Hydrogen storage: Materials, methods and perspectives. *Renewable and Sustainable Energy Reviews* **2015**, *50*, 457–469, doi:https://doi.org/10.1016/j.rser.2015.05.011.
16. Trasatti, S. ELECTROCHEMICAL THEORY | Hydrogen Evolution. In *Encyclopedia of Electrochemical Power Sources*, Garche, J., Ed.; Elsevier: Amsterdam, 2009; pp. 41–48.
17. Schüth, F.; Bogdanović, B.; Felderhoff, M. Light metal hydrides and complex hydrides for hydrogen storage. *Chemical Communications* **2004**, 2249–2258, doi:10.1039/B406522K.
18. Zhou, L. Progress and problems in hydrogen storage methods. *Renewable and Sustainable Energy Reviews* **2005**, *9*, 395–408, doi:https://doi.org/10.1016/j.rser.2004.05.005.
19. Omranpour Shahreza, B.; Ivanisenko, J.; Sergejev, F.; Omranpour, H.; Huot, J. A novel approach in mechanical nanostructuring synthesis of metal hydride: Hydrogen sorption enhancement by High Pressure Torsion Extrusion. *International Journal of Hydrogen Energy* **2024**, *51*, 133–142, doi:https://doi.org/10.1016/j.ijhydene.2023.10.343.
20. He, T.; Cao, H.; Chen, P. Complex hydrides for energy storage, conversion, and utilization. *Advanced Materials* **2019**, *31*, 1902757.
21. Srinivasan, S.S.; Demirocak, D.E. Metal Hydrides used for Hydrogen Storage. In *Nanostructured Materials for Next-Generation Energy Storage and Conversion: Hydrogen Production, Storage, and Utilization*, Chen, Y.-P., Bashir, S., Liu, J.L., Eds.; Springer Berlin Heidelberg: Berlin, Heidelberg, 2017; pp. 225–255.
22. Lys, A.; Fadonougbo, J.O.; Faisal, M.; Suh, J.-Y.; Lee, Y.-S.; Shim, J.-H.; Park, J.; Cho, Y.W. Enhancing the Hydrogen Storage Properties of AxBy Intermetallic Compounds by Partial Substitution: A Short Review. *Hydrogen* **2020**, *1*, 38–63.
23. Rusman, N.; Dahari, M. A review on the current progress of metal hydrides material for solid-state hydrogen storage applications. *International Journal of Hydrogen Energy* **2016**, *41*, 12108–12126.
24. Huot, J. Metal Hydrides. In *Handbook of Hydrogen Storage*; 2010; pp. 81–116.
25. Klopčič, N.; Grimmer, I.; Winkler, F.; Sartory, M.; Trattner, A. A review on metal hydride materials for hydrogen storage. *Journal of Energy Storage* **2023**, *72*, 108456, doi:https://doi.org/10.1016/j.est.2023.108456.
26. Dornheim, M. Thermodynamics of Metal Hydrides: Tailoring Reaction Enthalpies of Hydrogen Storage Materials. In *Thermodynamics - Interaction Studies - Solids, Liquids and Gases*, Moreno Piraján, J.C., Ed.; IntechOpen: Rijeka, 2011.
27. Sun, W.; Powell-Palm, M.J. Generalized Gibbs' phase rule. *arXiv preprint arXiv:2105.01337* **2021**.
28. Hagstro¨m, M.T.; Lund, P.D.; Vanhanen, J.P. Metal hydride hydrogen storage for near-ambient temperature and atmospheric pressure applications, a PDSC study. *International Journal of Hydrogen Energy* **1995**, *20*, 897–909, doi:https://doi.org/10.1016/0360-3199(95)00025-9.
29. Liu, H.; Zhang, J.; Sun, P.; Zhou, C.; Liu, Y.; Fang, Z.Z. An overview of TiFe alloys for hydrogen storage: Structure, processes, properties, and applications. *Journal of Energy Storage* **2023**, *68*, 107772, doi:https://doi.org/10.1016/j.est.2023.107772.

30. Sujan, G.K.; Pan, Z.; Li, H.; Liang, D.; Alam, N. An overview on TiFe intermetallic for solid-state hydrogen storage: microstructure, hydrogenation and fabrication processes. *Critical Reviews in Solid State and Materials Sciences* **2019**, *45*, doi:10.1080/10408436.2019.1652143.
31. Kuziora, P.; Kunce, I.; McCain, S.; Adkins, N.J.E.; Polański, M. The influence of refractory metals on the hydrogen storage characteristics of FeTi-based alloys prepared by suspended droplet alloying. *International Journal of Hydrogen Energy* **2020**, *45*, 21635–21645, doi:https://doi.org/10.1016/j.ijhydene.2020.05.216.
32. Park, K.B.; Ko, W.-S.; Fadonougbo, J.O.; Na, T.-W.; Im, H.-T.; Park, J.-Y.; Kang, J.-W.; Kang, H.-S.; Park, C.-S.; Park, H.-K. Effect of Fe substitution by Mn and Cr on first hydrogenation kinetics of air-exposed TiFe-based hydrogen storage alloy. *Materials Characterization* **2021**, *178*, 111246, doi:https://doi.org/10.1016/j.matchar.2021.111246.
33. Reilly, J.J.; Wiswall, R.H. Formation and properties of iron titanium hydride. *Inorganic Chemistry* **1974**, *13*, 218–222, doi:10.1021/ic50131a042.
34. Zhu, H.Y.; Wu, J.; Wang, Q.D. Reactivation behaviour of TiFe hydride. *Journal of Alloys and Compounds* **1994**, *215*, 91–95, doi:https://doi.org/10.1016/0925-8388(94)90823-0.
35. Lee, S.M.; Perng, T.P. Microstructural correlations with the hydrogenation kinetics of FeTi1+ξ alloys. *Journal of Alloys and Compounds* **1991**, *177*, 107–118, doi:https://doi.org/10.1016/0925-8388(91)90061-Y.
36. Schober, T.; Westlake, D.G. The activation of FeTi for hydrogen storage: A different view. *Scripta Metallurgica* **1981**, *15*, 913–918, doi:https://doi.org/10.1016/0036-9748(81)90277-5.
37. Dematteis, E.; Berti, N.; Cuevas, F.; Latroche, M.; Baricco, M. Substitutional effects in TiFe for hydrogen storage: a comprehensive review. *Materials Advances* **2021**, *2*, doi:10.1039/D1MA00101A.
38. Emami, H.; Edalati, K.; Matsuda, J.; Akiba, E.; Horita, Z. Hydrogen storage performance of TiFe after processing by ball milling. *Acta Materialia* **2015**, *88*, 190–195, doi:https://doi.org/10.1016/j.actamat.2014.12.052.
39. Edalati, K.; Matsuda, J.; Yanagida, A.; Akiba, E.; Horita, Z. Activation of TiFe for hydrogen storage by plastic deformation using groove rolling and high-pressure torsion: Similarities and differences. *International Journal of Hydrogen Energy* **2014**, *39*, 15589–15594, doi:https://doi.org/10.1016/j.ijhydene.2014.07.124.
40. Edalati, K.; Matsuda, J.; Arita, M.; Daio, T.; Akiba, E.; Horita, Z. Mechanism of activation of TiFe intermetallics for hydrogen storage by severe plastic deformation using high-pressure torsion. *Applied Physics Letters* **2013**, *103*, doi:10.1063/1.4823555.
41. Ulate-Kolitsky, E.; Tougas, B.; Huot, J. First Hydrogenation of TiFe with Addition of 20 wt.% Ti. *Hydrogen* **2022**, *3*, 379–388.
42. Ulate-Kolitsky, E.; Tougas, B.; Neumann, B.; Schade, C.; Huot, J. First hydrogenation of mechanically processed TiFe-based alloy synthesized by gas atomization. *International Journal of Hydrogen Energy* **2021**, *46*, 7381–7389, doi:https://doi.org/10.1016/j.ijhydene.2020.11.237.
43. Padhee, S.P.; Roy, A.; Pati, S. Role of Mn-substitution towards the enhanced hydrogen storage performance in FeTi. *International Journal of Hydrogen Energy* **2022**, *47*, 9357–9371, doi:https://doi.org/10.1016/j.ijhydene.2022.01.032.

44. Miller, H.I.; Murray, J.; Laury, E.; Reinhardt, J.; Goudy, A.J. The hydriding and dehydriding kinetics of FeTi and Fe0.9TiMn0.1. *Journal of Alloys and Compounds* **1995**, *231*, 670–674, doi:https://doi.org/10.1016/0925-8388(95)01750-X.
45. Li, C.; Gao, X.; Liu, B.; Wei, X.; Zhang, W.; Lan, Y.; Wang, H.; Yuan, Z. Effects of Zr doping on activation capability and hydrogen storage performances of TiFe-based alloy. *International Journal of Hydrogen Energy* **2023**, *48*, 2256–2270, doi:https://doi.org/10.1016/j.ijhydene.2022.10.098.
46. Lv, P.; Liu, Z.; Dixit, V. Improved hydrogen storage properties of TiFe alloy by doping (Zr+2V) additive and using mechanical deformation. *International Journal of Hydrogen Energy* **2019**, *44*, 27843–27852, doi:https://doi.org/10.1016/j.ijhydene.2019.08.249.
47. Chen, Z.; Guo, F.; Sunamoto, R.; Yin, C.; Miyaoka, H.; Ichikawa, T. Anti-oxidation effect of chromium addition for TiFe hydrogen storage alloys. *Journal of Alloys and Compounds* **2024**, *1008*, 176634, doi:https://doi.org/10.1016/j.jallcom.2024.176634.
48. Kumar, S.; Tiwari, G.P.; Sonak, S.; Jain, U.; Krishnamurthy, N. High performance FeTi – 3.1 mass % V alloy for on board hydrogen storage solution. *Energy* **2014**, *75*, 520–524, doi:https://doi.org/10.1016/j.energy.2014.08.011.
49. Guéguen, A.; Latroche, M. Influence of the addition of vanadium on the hydrogenation properties of the compounds TiFe0.9Vx and TiFe0.8Mn0.1Vx (x=0, 0.05 and 0.1). *Journal of Alloys and Compounds* **2011**, *509*, 5562–5566, doi:https://doi.org/10.1016/j.jallcom.2011.02.036.
50. Han, Z.; Yuan, Z.; Zhai, T.; Feng, D.; Sun, H.; Zhang, Y. Effect of yttrium content on microstructure and hydrogen storage properties of TiFe-based alloy. *International Journal of Hydrogen Energy* **2023**, *48*, 676–695, doi:https://doi.org/10.1016/j.ijhydene.2022.09.227.
51. Li, C.; Lan, Y.; Wei, X.; Zhang, W.; Liu, B.; Gao, X.; Yuan, Z. Improvement of hydrogen absorption and desorption properties of TiFe-based alloys by adding yttrium. *Journal of Alloys and Compounds* **2022**, *927*, 166992, doi:https://doi.org/10.1016/j.jallcom.2022.166992.
52. Jain, P.; Gosselin, C.; Skryabina, N.; Fruchart, D.; Huot, J. Hydrogenation properties of TiFe with Zr7Ni10 alloy as additive. *Journal of Alloys and Compounds* **2015**, *636*, 375–380, doi:https://doi.org/10.1016/j.jallcom.2015.02.104.
53. Kulshreshtha, S.K.; Jayakumar, O.D.; Bhatt, K.B. Hydriding characteristics of palladium and platinum alloyed FeTi. *Journal of Materials Science* **1993**, *28*, 4229–4233, doi:10.1007/BF00351259.
54. Bratanich, T.I.; Solonin, S.M.; Skorokhod, V.V. Mechanical activation of hydrogen sorption with intermetallic compounds LaNi5 and TiFe in powder systems. *International Journal of Hydrogen Energy* **1995**, *20*, 353–355, doi:https://doi.org/10.1016/0360-3199(94)00062-5.
55. Trudeau, M.L.; Dignard-Bailey, L.; Schulz, R.; Tessier, P.; Zaluski, L.; Ryan, D.H.; Strom-Olsen, J.O. The oxidation of nanocrystalline FeTi hydrogen storage compounds. *Nanostructured Materials* **1992**, *1*, 457–464, doi:https://doi.org/10.1016/0965-9773(92)90078-C.
56. Jai-Young, L.; Park, C.N.; Pyun, S.M. The activation processes and hydriding kinetics of FeTi. *Journal of the Less Common Metals* **1983**, *89*, 163–168, doi:https://doi.org/10.1016/0022-5088(83)90262-X.

57. Inui, H.; Yamamoto, T.; Hirota, M.; Yamaguchi, M. Lattice defects introduced during hydrogen absorption–desorption cycles and their effects on P–C characteristics in some intermetallic compounds. *Journal of Alloys and Compounds* **2002**, *330-332*, 117–124, doi:https://doi.org/10.1016/S0925-8388(01)01489-X.
58. Gosselin, C.; Santos, D.; Huot, J. First hydrogenation enhancement in TiFe alloys for hydrogen storage. *Journal of Physics D: Applied Physics* **2017**, *50*, 375303, doi:10.1088/1361-6463/aa7d6a.
59. Patel, A.K.; Duguay, A.; Tougas, B.; Schade, C.; Sharma, P.; Huot, J. Microstructure and first hydrogenation properties of TiFe alloy with Zr and Mn as additives. *International Journal of Hydrogen Energy* **2020**, *45*, 787–797, doi:https://doi.org/10.1016/j.ijhydene.2019.10.239.
60. Han, Z.; Li, J.; Zhai, T.; Sun, H.; Yuan, Z.; Li, T.; Zhang, L.; Zhang, Y. Effect on the activation and hydrogen storage properties of Y–TiFe-based composites with vanadium via mechanical milling. *International Journal of Hydrogen Energy* **2025**, *106*, 686–699.
61. Han, Z.; Wang, B.; Zhai, T.; Sun, H.; Li, T.; Yuan, Z.; Zhang, L.; Zhang, Y. Influence on the microstructure and hydrogen storage properties of Y–TiFe-based composites with transition metals via mechanical milling. *Intermetallics* **2025**, *177*, 108603, doi:https://doi.org/10.1016/j.intermet.2024.108603.
62. Luo, L.; Li, Y.; Liu, S.; Yang, F.; Yuan, Z.; Li, L.; Li, Y. Nanoscale microstructure and hydrogen storage performance of as cast La-containing V-based multicomponent alloys. *International Journal of Hydrogen Energy* **2022**, *47*, 34165–34182, doi:https://doi.org/10.1016/j.ijhydene.2022.08.021.
63. Patel, A.K.; Tougas, B.; Sharma, P.; Huot, J. Effect of cooling rate on the microstructure and hydrogen storage properties of TiFe with 4 wt% Zr as an additive. *Journal of Materials Research and Technology* **2019**, *8*, 5623–5630, doi:https://doi.org/10.1016/j.jmrt.2019.09.030.
64. *Powder Metallurgy*; ASM International: 2015.
65. Neikov, O.D. Chapter 4 - Atomization and Granulation. In *Handbook of Non-Ferrous Metal Powders (Second Edition)*, Neikov, O.D., Naboychenko, S.S., Yefimov, N.A., Eds.; Elsevier: Oxford, 2019; pp. 125–185.
66. Abe, M.; Kuji, T. Hydrogen absorption of TiFe alloy synthesized by ball milling and post-annealing. *Journal of Alloys and Compounds* **2007**, *446-447*, 200–203, doi:https://doi.org/10.1016/j.jallcom.2006.12.063.
67. Lee, S.M.; Perng, T.P. Effect of the second phase on the initiation of hydrogenation of TiFe1−xMx (M = Cr,Mn) alloys. *International Journal of Hydrogen Energy* **1994**, *19*, 259–263, doi:https://doi.org/10.1016/0360-3199(94)90095-7.
68. Suryanarayana, C. Mechanical alloying and milling. *Progress in materials science* **2001**, *46*, 1–184.
69. German, R.M. *Powder Metallurgy Science*; Metal Powder Industries Federation: 1994.
70. Evans, J.S.O. Advanced Input Files & Parametric Quantitative Analysis Using Topas. *Materials Science Forum* **2010**, *651*, 1–9, doi:10.4028/www.scientific.net/MSF.651.1.
71. Stan, C.V.; Beavers, C.M.; Kunz, M.; Tamura, N. X-ray diffraction under extreme conditions at the Advanced Light Source. *Quantum Beam Science* **2018**, *2*, 4.
72. Bunaciu, A.A.; UdriŞTioiu, E.G.; Aboul-Enein, H.Y. X-ray diffraction: instrumentation and applications. *Critical reviews in analytical chemistry* **2015**, *45*, 289–299.
73. Coelho, A.A. TOPAS-academic. *Coelho Software, Brisbane, Australia* **2007**.

74. Mohammed, A.; Abdullah, A. Scanning electron microscopy (SEM): A review. In Proceedings of the Proceedings of the 2018 International Conference on Hydraulics and Pneumatics—HERVEX, Băile Govora, Romania, 2018; pp. 7–9.
75. Flegler, S.L.; Heckman, J.W.; Klomparens, K.L. Scanning and transmission electron microscopy: an introduction. *(No Title)* **1993**.
76. Gray, E.M. 7 - Reliably measuring hydrogen uptake in storage materials. In *Solid-State Hydrogen Storage*, Walker, G., Ed.; Woodhead Publishing: 2008; pp. 174–204.
77. Fichtner, M. Chapter 6 - Nanoscale Materials For Hydrogen and Energy Storage. In *Frontiers of Nanoscience*, Wilde, G., Ed.; Elsevier: 2009; Volume 1, pp. 270–297.
78. Bernauer, O.; Halene, C. Properties of metal hydrides for use in industrial applications. *Journal of the Less Common Metals* **1987**, *131*, 213–224, doi:https://doi.org/10.1016/0022-5088(87)90521-2.
79. Sakintuna, B.; Lamari-Darkrim, F.; Hirscher, M. Metal hydride materials for solid hydrogen storage: A review. *International Journal of Hydrogen Energy* **2007**, *32*, 1121–1140, doi:https://doi.org/10.1016/j.ijhydene.2006.11.022.
80. Schlapbach, L.; Züttel, A. Hydrogen-storage materials for mobile applications. *Nature* **2001**, *414*, 353–358, doi:10.1038/35104634.
81. Haraki, T.; Oishi, K.; Uchida, H.; Miyamoto, Y.; Abe, M.; Kokaji, T.; Uchida, S. Properties of hydrogen absorption by nano-structured FeTi alloys. *International Journal of Materials Research* **2008**, *99*, 507–512, doi:doi:10.3139/146.101669.
82. Lanyin, S.; Fangjie, L.; Deyou, B. An advanced TiFe series hydrogen storage material with high hydrogen capacity and easily activated properties. *International Journal of Hydrogen Energy* **1990**, *15*, 259–262.
83. Zadorozhnyy, V.; Klyamkin, S.; Zadorozhnyy, M.; Bermesheva, O.; Kaloshkin, S. Hydrogen storage nanocrystalline TiFe intermetallic compound: Synthesis by mechanical alloying and compacting. *International Journal of Hydrogen Energy* **2012**, *37*, 17131–17136, doi:https://doi.org/10.1016/j.ijhydene.2012.08.078.
84. Schober, T. On the activation of FeTi for hydrogen storage. *Journal of the Less Common Metals* **1983**, *89*, 63–70, doi:https://doi.org/10.1016/0022-5088(83)90249-7.
85. Bläsius, A.; Gonster, U. Mössbauer surface studies on Tife hydrogen storage material. *Applied physics* **1980**, *22*, 331–332, doi:10.1007/BF00899887.
86. Modi, P.; Aguey-Zinsou, K.-F. Titanium-iron-manganese (TiFe0.85Mn0.15) alloy for hydrogen storage: Reactivation upon oxidation. *International Journal of Hydrogen Energy* **2019**, *44*, 16757–16764, doi:https://doi.org/10.1016/j.ijhydene.2019.05.005.
87. Yuan, Z.-m.; Qi, Z.; Zhai, T.-t.; Wang, H.-z.; Wang, H.-y.; Zhang, Y.-h. Effects of La substitution on microstructure and hydrogen storage properties of Ti–Fe–Mn-based alloy prepared through melt spinning. *Transactions of Nonferrous Metals Society of China* **2021**, *31*, 3087–3095, doi:https://doi.org/10.1016/S1003-6326(21)65717-5.
88. Dematteis, E.M.; Dreistadt, D.M.; Capurso, G.; Jepsen, J.; Cuevas, F.; Latroche, M. Fundamental hydrogen storage properties of TiFe-alloy with partial substitution of Fe by Ti and Mn. *Journal of Alloys and Compounds* **2021**, *874*, 159925, doi:https://doi.org/10.1016/j.jallcom.2021.159925.
89. Jung, J.Y.; Lee, S.-I.; Faisal, M.; Kim, H.; Lee, Y.-S.; Suh, J.-Y.; Shim, J.-H.; Huh, J.-Y.; Cho, Y.W. Effect of Cr addition on room temperature hydrogenation of TiFe alloys. *International Journal of Hydrogen Energy* **2021**, *46*, 19478–19485, doi:https://doi.org/10.1016/j.ijhydene.2021.03.096.

90. Komedera, K.; Michalik, J.; Sworst, K.; Gondek, Ł. Structure, Microstructure and Hyperfine Interactions in Hf- and Ni-Substituted TiFe Alloy for Hydrogen Storage. *Acta Physica Polonica A* **2024**, *146*, 215–221, doi:10.12693/APhysPolA.146.215.
91. Sun, H.; Yan, Z.; Han, Z.; Li, J.; Zhai, T.; Yuan, Z.; Li, T.; Xu, J.; Zhang, Y. Hydrogen storage properties of TiFe-based composite with Ni addition. *Heliyon* **2024**, *10*, e41022, doi:https://doi.org/10.1016/j.heliyon.2024.e41022.
92. Chung, H.S.; Lee, J.Y. Effect of partial substitution of Mn and Ni for Fe in FeTi on hydriding kinetics. *International Journal of Hydrogen Energy* **1986**, *11*, 335–339, doi:https://doi.org/10.1016/0360-3199(86)90153-9.
93. Fruchart, D.; Commandré, M.; Sauvage, D.; Rouault, A.; Tellgren, R. Structural and activation process studies of Fe・Ti-like hydride compounds. *Journal of the Less Common Metals* **1980**, *74*, 55–63, doi:https://doi.org/10.1016/0022-5088(80)90073-9.
94. Manna, J.; Tougas, B.; Huot, J. Mechanical activation of air exposed TiFe + 4 wt% Zr alloy for hydrogenation by cold rolling and ball milling. *International Journal of Hydrogen Energy* **2018**, *43*, 20795–20800, doi:https://doi.org/10.1016/j.ijhydene.2018.09.096.
95. Patel, A.K.; Sharma, P.; Huot, J. Effect of annealing on microstructure and hydrogenation properties of TiFe + X wt% Zr (X = 4, 8). *International Journal of Hydrogen Energy* **2018**, *43*, 6238–6243, doi:https://doi.org/10.1016/j.ijhydene.2018.02.029.
96. Patel, A.; Huot, J.; Sharma, P. *Hydrogen storage properties of TiFe + X wt.% Zr, V (X=0, 4) alloys*; 2016.
97. Jain, P.; Gosselin, C.; Huot, J. Effect of Zr, Ni and Zr7Ni10 alloy on hydrogen storage characteristics of TiFe alloy. *International Journal of Hydrogen Energy* **2015**, *40*, 16921–16927, doi:https://doi.org/10.1016/j.ijhydene.2015.06.007.
98. Oliveira, V.B.; Beatrice, C.A.G.; Leal, R.M.; Silva, W.B.; Pessan, L.A.; Botta, W.J.; Leiva, D.R. Hydrogen absorption/desorption behavior of a cold-rolled TiFe intermetallic compound. *Materials Research* **2021**, *24*, e20210204.
99. Vega, L.E.R.; Leiva, D.R.; Leal Neto, R.M.; Silva, W.B.; Silva, R.A.; Ishikawa, T.T.; Kiminami, C.S.; Botta, W.J. Improved ball milling method for the synthesis of nanocrystalline TiFe compound ready to absorb hydrogen. *International Journal of Hydrogen Energy* **2020**, *45*, 2084–2093, doi:https://doi.org/10.1016/j.ijhydene.2019.11.035.
100. Tajima, I.; Abe, M.; Uchida, H.; Hattori, M.; Miyamoto, Y.; Haraki, T. Hydrogen sorption kinetics of FeTi alloy with nano-structured surface layers. *Journal of Alloys and Compounds* **2013**, *580*, S33–S35, doi:https://doi.org/10.1016/j.jallcom.2013.03.011.
101. Gómez, E.I.L.; Edalati, K.; Antiqueira, F.J.; Coimbrão, D.D.; Zepon, G.; Leiva, D.R.; Ishikawa, T.T.; Cubero-Sesin, J.M.; Botta, W.J. Synthesis of Nanostructured TiFe Hydrogen Storage Material by Mechanical Alloying via High-Pressure Torsion. *Advanced Engineering Materials* **2020**, *22*, doi:10.1002/adem.202000011.
102. Shang, H.; Li, Y.; Li, C.; Hu, D.; Yang, G.; Li, J.; Zhang, Y.; Zhang, Y. Activation, modification and application of TiFe-based hydrogen storage alloys. *International Journal of Hydrogen Energy* **2024**, *96*, 274–299, doi:https://doi.org/10.1016/j.ijhydene.2024.11.278.
103. Chiang, C.H.; Chin, Z.H.; Perng, T.P. Hydrogenation of TiFe by high-energy ball milling. *Journal of Alloys and Compounds* **2000**, *307*, 259–265, doi:https://doi.org/10.1016/S0925-8388(00)00827-6.

104. Lee, S.-Y.; Ha, T.; Suh, J.-Y.; Kim, D.-I.; Lee, Y.-S.; Shim, J.-H. Orientation relationship between TiFeH and TiFe phases in AB-type Ti–Fe–V–Ce hydrogen storage alloy. *Journal of Alloys and Compounds* **2024**, *983*, 173943, doi:https://doi.org/10.1016/j.jallcom.2024.173943.
105. Edalati, K.; Matsuo, M.; Emami, H.; Itano, S.; Alhamidi, A.; Staykov, A.; Smith, D.J.; Orimo, S.-i.; Akiba, E.; Horita, Z. Impact of severe plastic deformation on microstructure and hydrogen storage of titanium-iron-manganese intermetallics. *Scripta Materialia* **2016**, *124*, 108–111, doi:https://doi.org/10.1016/j.scriptamat.2016.07.007.
106. Lv, P.; Guzik, M.N.; Sartori, S.; Huot, J. Effect of ball milling and cryomilling on the microstructure and first hydrogenation properties of TiFe+4wt.% Zr alloy. *Journal of Materials Research and Technology* **2019**, *8*, 1828–1834, doi:https://doi.org/10.1016/j.jmrt.2018.12.013.
107. Gubicza, J. Chapter 11 - Relationship Between Microstructure and Hydrogen Storage Properties of Nanomaterials. In *Defect Structure and Properties of Nanomaterials (Second Edition)*, Gubicza, J., Ed.; Woodhead Publishing: 2017; pp. 297–315.
108. Sleiman, S.; Aliouat, A.; Huot, J. Enhancement of First Hydrogenation of Ti1V0.9Cr1.1 BCC Alloy by Cold Rolling and Ball Milling. *Materials* **2020**, *13*, 3106.
109. Patel, A.K.; Siemiaszko, D.; Dworecka-Wójcik, J.; Polański, M. Just shake or stir. About the simplest solution for the activation and hydrogenation of an FeTi hydrogen storage alloy. *International Journal of Hydrogen Energy* **2022**, *47*, 5361–5371, doi:https://doi.org/10.1016/j.ijhydene.2021.11.136.
110. Alloy Phase Diagrams. **2016**, doi:10.31399/asm.hb.v03.9781627081634.
111. Dong, C.; Hei, Z.K.; Wang, L.B.; Song, Q.H.; Wu, Y.K.; Kuo, K.H. A new icosahedral quasicrystal in rapidly solidified FeTi2. *Scripta Metallurgica* **1986**, *20*, 1155–1158, doi:https://doi.org/10.1016/0036-9748(86)90194-8.
112. Fruchart, D.; Commandré, M.; Sauvage, D.; Rouault, A.; Tellgren, R. Structural and activation process studies of FeTi-like hydride compounds☆. *Journal of The Less Common Metals* **1980**, *74*, 55–63.
113. Jung, J.Y.; Lee, Y.-S.; Suh, J.-Y.; Huh, J.-Y.; Cho, Y.W. Tailoring the equilibrium hydrogen pressure of TiFe via vanadium substitution. *Journal of Alloys and Compounds* **2021**, *854*, 157263, doi:https://doi.org/10.1016/j.jallcom.2020.157263.
114. Reidinger, F.; Lynch, J.F.; Reilly, J.J. An X-ray diffraction examination of the FeTi-H2 system. *Journal of Physics F: Metal Physics* **1982**, *12*, L49, doi:10.1088/0305-4608/12/3/007.
115. Kirchheim, R.; Pundt, A. 25 - Hydrogen in Metals. In *Physical Metallurgy (Fifth Edition)*, Laughlin, D.E., Hono, K., Eds.; Elsevier: Oxford, 2014; pp. 2597–2705.
116. Bosu, S.; Rajamohan, N. Recent advancements in hydrogen storage-Comparative review on methods, operating conditions and challenges. *International Journal of Hydrogen Energy* **2024**, *52*, 352–370.
117. Abe, J.O.; Popoola, A.P.I.; Ajenifuja, E.; Popoola, O.M. Hydrogen energy, economy and storage: Review and recommendation. *International Journal of Hydrogen Energy* **2019**, *44*, 15072–15086, doi:https://doi.org/10.1016/j.ijhydene.2019.04.068.
118. Schlapbach, L. Technology: Hydrogen-fuelled vehicles. *Nature* **2009**, *460*, 809–811, doi:10.1038/460809a.

119. Rachidi, S.; El Kassaoui, M.; Tahiri, N.; Mounkachi, O.; Ez-Zahraouy, H. Understanding degradation mechanisms and hydrogenation kinetics of intrinsic γ-FeTiH2. *Journal of Energy Storage* **2024**, *104*, 114571, doi:https://doi.org/10.1016/j.est.2024.114571.
120. Lototsky, M.V.; Davids, M.W.; Fokin, V.N.; Fokina, E.E.; Tarasov, B.P. Hydrogen-Accumulating Materials Based on Titanium and Iron Alloys (Review). *Thermal Engineering* **2024**, *71*, 264–279, doi:10.1134/S0040601524030030.
121. Sartori, S.; Amati, M.; Gregoratti, L.; Jensen, E.H.; Kudriashova, N.; Huot, J. Study of Phase Composition in TiFe+ 4 wt.% Zr Alloys by Scanning Photoemission Microscopy. *Inorganics* **2023**, *11*, 26.
122. Zhu, H.; Wu, J.; Wang, Q. Reactivation behaviour of TiFe hydride. *Journal of alloys and compounds* **1994**, *215*, 91–95.
123. Liu, H.; Zhang, J.; Sun, P.; Zhou, C.; Liu, Y.; Fang, Z.Z. The mechanistic role of Ti4Fe2O1-x phases in the activation of TiFe alloys for hydrogen storage. *International Journal of Hydrogen Energy* **2023**, *48*, 32011–32024, doi:https://doi.org/10.1016/j.ijhydene.2023.05.016.
124. Gosselin, C.; Huot, J. First hydrogenation enhancement in TiFe alloys for hydrogen storage doped with yttrium. *Metals* **2019**, *9*, 242.
125. Falcão, R.B.; Dammann, E.D.C.C.; Rocha, C.J.; Durazzo, M.; Ichikawa, R.U.; Martinez, L.G.; Botta, W.J.; Leal Neto, R.M. An alternative route to produce easily activated nanocrystalline TiFe powder. *International Journal of Hydrogen Energy* **2018**, *43*, 16107–16116, doi:https://doi.org/10.1016/j.ijhydene.2018.07.027.
126. Edalati, K.; Matsuda, J.; Iwaoka, H.; Toh, S.; Akiba, E.; Horita, Z. High-pressure torsion of TiFe intermetallics for activation of hydrogen storage at room temperature with heterogeneous nanostructure. *International Journal of Hydrogen Energy* **2013**, *38*, 4622–4627, doi:https://doi.org/10.1016/j.ijhydene.2013.01.185.
127. Park, K.B.; Fadonougbo, J.O.; Na, T.-W.; Lee, T.W.; Kim, M.; Lee, D.H.; Kwon, H.G.; Park, C.-S.; Do Kim, Y.; Park, H.-K. On the first hydrogenation kinetics and mechanisms of a TiFe0.85Cr0.15 alloy produced by gas atomization. *Materials Characterization* **2022**, *192*, 112188, doi:https://doi.org/10.1016/j.matchar.2022.112188.
128. Lee, D.H.; Kwon, H.G.; Park, K.B.; Im, H.-T.; Kwak, R.H.; Sohn, S.S.; Park, H.-K.; Fadonougbo, J.O. Phase formation behavior and hydrogen sorption characteristics of TiFe0.8Mn0.2 powders prepared by gas atomization. *International Journal of Hydrogen Energy* **2023**, *48*, 27697–27709, doi:https://doi.org/10.1016/j.ijhydene.2023.03.289.
129. Nong, Z.-S.; Zhu, J.-C.; Yang, X.-W.; Cao, Y.; Lai, Z.-H.; Liu, Y. First-principles study of hydrogen storage and diffusion in B2 FeTi alloy. *Computational Materials Science* **2014**, *81*, 517–523, doi:https://doi.org/10.1016/j.commatsci.2013.08.060.
130. Lebsanft, E.; Richter, D.; Topler, J. Investigation of the hydrogen diffusion in FeTiHx by means of quasielastic neutron scattering. *Journal of Physics F: Metal Physics* **1979**, *9*, 1057, doi:10.1088/0305-4608/9/6/012.
131. Bowman Jr, R.C.; Tadlock, W.E. Hydrogen diffusion in β-phase titanium iron hydride. *Solid State Communications* **1979**, *32*, 313–318.
132. Chung, H.; Lee, J.-Y. Effect of partial substitution of Mn and Ni for Fe in FeTi on hydriding kinetics. *International journal of hydrogen energy* **1986**, *11*, 335–339.
133. Hosseinigourajoubi, S.; Schade, C.; Huot, J. The Effect of Annealing on the First Hydrogenation Behavior of Atomized Ti48.8Fe46.0Mn5.2 Alloy. *Metals* **2025**, *15*, 251.

134. Vega, L.E.R.; Leiva, D.R.; Leal Neto, R.M.; Silva, W.B.; Silva, R.A.; Ishikawa, T.T.; Kiminami, C.S.; Botta, W.J. Mechanical activation of TiFe for hydrogen storage by cold rolling under inert atmosphere. *International Journal of Hydrogen Energy* **2018**, *43*, 2913–2918, doi:https://doi.org/10.1016/j.ijhydene.2017.12.054.
135. Tousignant, M.; Huot, J. Hydrogen sorption enhancement in cold rolled LaNi5. *Journal of Alloys and Compounds* **2014**, *595*, 22–27, doi:https://doi.org/10.1016/j.jallcom.2014.01.169.
136. Lima, G.F.; Triques, M.R.M.; Kiminami, C.S.; Botta, W.J.; Jorge, A.M. Hydrogen storage properties of pure Mg after the combined processes of ECAP and cold-rolling. *Journal of Alloys and Compounds* **2014**, *586*, S405–S408, doi:https://doi.org/10.1016/j.jallcom.2013.03.106.
137. Floriano, R.; Leiva, D.R.; Carvalho, J.A.; Ishikawa, T.T.; Botta, W.J. Cold rolling under inert atmosphere: A powerful tool for Mg activation. *International Journal of Hydrogen Energy* **2014**, *39*, 4959–4965, doi:https://doi.org/10.1016/j.ijhydene.2014.01.070.
138. Hidalgo-Jimenez, J.; Cubero-Sesin, J.M.; Edalati, K.; Khajavi, S.; Huot, J. Effect of high-pressure torsion on first hydrogenation of Laves phase Ti0.5Zr0.5(Mn1-xFex)Cr1 (x = 0, 0.2 and 0.4) high entropy alloys. *Journal of Alloys and Compounds* **2023**, *969*, 172243, doi:https://doi.org/10.1016/j.jallcom.2023.172243.
139. Rudman, P. Hydrogen-diffusion-rate-limited hydriding and dehydriding kinetics. *Journal of Applied Physics* **1979**, *50*, 7195–7199.
140. Huston, E.L.; Sandrock, G.D. Engineering properties of metal hydrides. *Journal of the Less Common Metals* **1980**, *74*, 435–443, doi:https://doi.org/10.1016/0022-5088(80)90182-4.
141. Sleiman, S.; Shahgaldi, S.; Huot, J. Investigation of the First Hydrogenation of LaNi5. *Reactions* **2024**, *5*, 419–428.
142. Zeaiter, A.; Nardin, P.; Pour Yazdi, M.A.; Billard, A. Outstanding shortening of the activation process stage for a TiFe-based hydrogen storage alloy. *Materials Research Bulletin* **2019**, *112*, 132–141, doi:https://doi.org/10.1016/j.materresbull.2018.12.015.
143. Bakulin, A.V.; Kulkov, A.S.; Kulkova, S.E. Impurity influence on the hydrogen diffusivity in B2–TiFe. *International Journal of Hydrogen Energy* **2023**, *48*, 232–242, doi:https://doi.org/10.1016/j.ijhydene.2022.09.206.

PUBLICATIONS

Article 1

hydrogen

MDPI

Article

Effect of Mechanical Processing on First Hydrogenation of Gas-Atomized $Ti_{0.488}Fe_{0.46}Mn_{0.052}$ Alloy

Seyedehfaranak Hosseinigourajoubi [1], Chris Schade [2] and Jacques Huot [1,*]

[1] Hydrogen Research Institute, Université du Québec à Trois-Rivières, Trois-Rivières, QC G9A5H7, Canada; seyedeh.faranak.hosseini.gourajoubi@uqtr.ca
[2] GKN Hoeganaes Innovation Centre & Advanced Materials, Cinnaminson, NJ 08077, USA; chris.schade@hoeganaes.com
* Correspondence: jacques.huot@uqtr.ca; Tel.: +1-819-376-5011 (ext. 3576); Fax: +1-819-376-5164

Abstract

In this paper, we report the effects of cold rolling, ball milling, and cold pressing on the first hydrogenation behavior of $Ti_{0.488}Fe_{0.460}Mn_{0.052}$ alloy synthesized by gas atomization and exposed to the air for an extended period. It was found that cold pressing led to a higher hydrogen absorption capacity of 1.9 wt.%, while ball milling significantly improved the kinetics, achieving an incubation time of only 7 min. The cold-rolled sample (5 passes) showed a hydrogen absorption capacity similar to the ball-milled sample (1.5 wt.%) but with a slower hydrogenation rate. To further optimize the cold rolling process, the influence of the rolling atmosphere and the number of passes was systematically examined. In both air and argon, increasing the number of cold rolling passes resulted in longer incubation times. However, samples rolled under argon showed shorter incubation times compared to those rolled in the air. The difference between the two atmospheres became more pronounced after 20 rolling passes; the sample rolled in argon showed an incubation time of 55 min, whereas the sample rolled in air failed to absorb hydrogen even after 24 h.

Keywords: hydrogen storage; metal hydride; TiFe; gas atomization; cold rolling; ball milling; cold pressing; argon atmosphere

Academic Editor: Lusheng Wang and Yuxin Wang

Received: 4 September 2025
Revised: 8 November 2025
Accepted: 20 November 2025
Published: 2 December 2025

Citation: Hosseinigourajoubi, S.; Schade, C.; Huot, J. Effect of Mechanical Processing on First Hydrogenation of Gas-Atomized $Ti_{0.488}Fe_{0.46}Mn_{0.052}$ Alloy. *Hydrogen* **2025**, *6*, 114. https://doi.org/10.3390/hydrogen6040114

1. Introduction

Hydrogen storage using metal hydrides is recognized as a safe and cost-effective method, providing high volumetric hydrogen density at moderate temperatures and pressures [1–3]. Among the reversible metal hydrides, FeTi-based alloys are interesting due to their ability to undergo reversible hydrogen absorption at conditions close to room temperature and atmospheric pressure, as well as the abundance and accessibility of their constituent elements [4–7].

FeTi hydrogen storage alloys suffer from sluggish hydrogen uptake, primarily due to the formation of stable oxide layers on the surface [8–10]. Activation of the TiFe alloys synthesized through conventional methods such as arc melting requires repeated heating cycles at approximately 400 °C under vacuum, followed by exposure to high hydrogen pressures (up to 6.5 MPa) to initiate hydrogen absorption [11]. This necessity for high-temperature and high-pressure activation represents an additional cost and a significant barrier to their commercial application.

Various strategies have been proposed to enhance the absorption kinetics of these materials. One common approach is partial substitution of Fe by transition metals such

as Mn [12–16], Cr [17,18], and Ni [19,20]. Modi et al. reported that the reactivation of the $TiFe_{0.85}Mn_{0.15}$ alloy, which had been deactivated due to surface oxidation from air exposure, was significantly improved by applying a single heat treatment cycle (without the need for multiple heat treatments) at temperatures up to a maximum of 300 °C under hydrogen pressure [14]. Chung and Lee observed that partially substituting Fe with Mn promoted activation, which was attributed to the formation of secondary phases [21]. Fruchart et al. also reported that Mn addition increases the unit cell volume, which facilitates the hydrogen absorption at lower pressures [22].

Furthermore, the addition of a small amount of Zr to TiFe often leads to the formation of a secondary phase which acts as a gateway for hydrogen diffusion [23–28]. Manna et al. found that as-cast TiFe + 4 wt.% Zr absorbed 1.5 wt.% hydrogen after 45 min of incubation time [24]. Jain et al. demonstrated that the addition of zirconium, either in its pure form or as an alloy, enabled the activation of TiFe after arc melting, without requiring any prior treatment [28].

Mechanical treatments such as cold rolling (CR) [24,29–31], ball milling (BM) [32–35], and high-pressure torsion (HPT) [36,37] are also promising methods for improving the activation behavior of TiFe alloys. These techniques can introduce defects, reduce particle size, and create fresh surfaces that enhance hydrogen uptake kinetics [24,29,38]. Abe et al. found that TiFe alloys synthesized via mechanical alloying followed by annealing could absorb hydrogen at room temperature. They observed that the first hydrogenation behavior of mechanically alloyed TiFe was significantly improved compared to conventional TiFe alloys produced by induction melting [34]. Chiang et al. prepared TiFe by arc melting and subjected the alloy to ball milling under hydrogen [39]. Their findings indicated that ball milling in hydrogen atmosphere enabled TiFe to absorb hydrogen without requiring an activation treatment. Vega et al. reported that TiFe processed by arc melting and subsequently subjected to 20 or 40 cold rolling passes under an inert atmosphere could absorb hydrogen rapidly at room temperature without the need for thermal activation, reaching a hydrogen absorption capacity of 1.4 wt% [30]. Gómez et al. found that nanostructured TiFe synthesized by the high-pressure torsion (HPT) method could absorb hydrogen at room temperature with fast kinetics after an activation treatment by a single-cycle evacuation at 673 K for 2 h [37]. Manna et al. studied TiFe + 4 wt% Zr + 2 wt% Mn alloy produced by the induction melting method and reported that after seven days of air exposure, the first hydrogenation kinetics were slow, with a long incubation time [24]. After 30 days of air exposure, no hydrogen absorption was observed. However, they showed that the air-exposed alloy could still be hydrogenated after ball milling or cold rolling, although with reduced capacity and slower kinetics. Similarly, Ulate-Kolitsky et al. investigated the same TiFe + 4 wt% Zr + 2 wt% Mn alloy produced by gas atomization, a method capable of directly producing metallic powders with high cooling rates, resulting in refined microstructures [29]. They demonstrated that gas-atomized alloy exhibited finer microstructures compared to induction-melted alloy, and cold rolling was more effective in recovering the hydrogenation performance of the atomized alloy compared to induction-melted samples. These results indicate that the effectiveness of cold rolling strongly depends on the alloy's microstructure. Patel et al. investigated the effect of cooling rate on the microstructure and hydrogenation performance of TiFe + 4 wt.% Zr alloy and found that higher cooling rate led to a finer microstructure, which significantly improved hydrogen absorption kinetics [40]. These studies suggest that gas atomization could be a promising method for the production of metal hydride alloys with refined microstructures.

Despite these advancements, most studies on TiFe-based alloys have focused on samples produced by conventional casting methods, while investigations on gas-atomized alloys remain scarce. Moreover, most existing works focus on a single mechanical process-

ing technique (such as cold rolling or ball milling), whereas comparative evaluations of different treatments are limited. In this work, we address this gap by investigating the first hydrogenation behavior of $Ti_{0.488}Fe_{0.460}Mn_{0.052}$ alloy synthesized by gas atomization and stored in air for more than two years. Three mechanical treatments, cold rolling, ball milling, and cold pressing, were systematically compared. In addition, the effects of rolling atmosphere and number of passes on the first hydrogenation are reported. This approach provides new insights into how different processing routes influence the activation of gas-atomized TiFe-based alloys.

2. Materials and Methods

2.1. Materials

The $Ti_{0.488}Fe_{0.460}Mn_{0.052}$ alloy in powder form was provided by GKN Hoeganaes (Cinnaminson, NJ, USA). The powder was produced via gas atomization under an argon atmosphere. After production, the samples were stored in the air for over 2 years.

2.2. Morphology and Crystal Structure

The microstructure and morphology of the powder were investigated using a Hitachi SU1510 scanning electron microscope (SEM) (Hitachi High-Tech Canada, Toronto, ON, Canada). Elemental composition was determined through Energy Dispersive X-ray Spectroscopy (EDX) with an Oxford Instrument X-Max system (Abingdon, UK), ensuring high analytical resolution.

The phase composition and crystal structure of the samples were analyzed by X-ray diffraction (XRD) using a Bruker D8 Focus powder diffractometer (Madison, WI, USA) with Cu Kα radiation. The resulting XRD patterns were evaluated using the Rietveld refinement software TOPAS V6.

2.3. Alloy Processing

High-energy ball milling was performed using a SPEX 8000M high-energy ball mill (SPEX SamplePrep, Metuchen, NJ, USA). The powder-to-ball mass ratio was 1:10, and milling was carried out for 10 min using a 55 cc stainless steel crucible. The vibration frequency was 1060 cycles per minute. All the loading and unloading of the powder were performed inside an argon-filled glove box to prevent contamination.

Cold pressing was carried out using a hydraulic press manufactured by Research & Industrial Instruments Company (London, UK). A die with a diameter of 14 mm was used to compact the powder under uniaxial pressure. The sample was subjected to a force of 12 tons for 2 min. After cold pressing, the obtained pellet was manually crushed into powder using a hardened steel mortar and pestle in the air.

Cold rolling in the air was conducted using a modified Durston DRM 130 model (Durston Tools, High Wycombe, UK), with powder being rolled vertically between two 0.5 mm-thick 316 stainless steel plates to avoid contamination. For cold rolling in argon, an International Rolling Mills (Pawtucket, RI, USA) was placed inside an argon-filled glove box. Rolling speed was 20 rpm for both air and argon atmospheres. The roller gap was set to 1.1 mm; considering the combined thickness of the two steel plates (1.0 mm), the effective rolling space available for the powder was approximately 0.1 mm.

2.4. Hydrogenation Properties

The first hydrogenation tests were carried out at room temperature (25 °C) under a hydrogen pressure of 2000 kPa using a homemade Sievert-type apparatus. For each first hydrogenation test, one gram of powder was placed in the sample holder and evacuated for 15 min before the measurement.

3. Results and Discussion

Figure 1 presents the microstructure of the atomized $Ti_{0.488}Fe_{0.460}Mn_{0.052}$ powder, revealing two distinct regions: a grey matrix and a darker grey filamentous region.

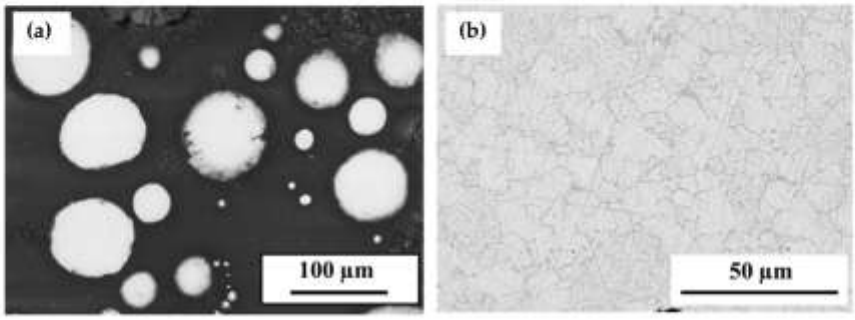

Figure 1. SEM images of the microstructure of the gas-atomized powder at magnifications of (**a**) 300× and (**b**) 1000×.

Figure 2a shows a higher-magnification backscattered electrons micrograph. At this magnification, three regions are visible. The main region (matrix) is light grey. Two secondary regions are seen: a darker grey region (Spectrum 2) and a much smaller black region (Spectrum 3). The chemical composition of the bulk material, matrix, and secondary phases, as determined by EDS, is summarized in Table 1.

Table 1. Elemental composition in atomic percent (at. %) from EDX analysis of the gas-atomized powder. Error on the last significant digit is in parentheses.

Element	Nominal	Bulk	Spectrum 1 (Matrix)	Spectrum 2 (Dark Grey Region)	Spectrum 3 (Black Region)
Ti	48.8	49.4 (3)	47.5 (5)	59.1 (3)	66.6 (2)
Fe	46	45.3 (4)	48.4 (6)	34.8 (2)	26.3 (4)
Mn	5.2	5.3 (2)	4.1 (5)	6.1 (3)	7.1 (1)

Based on bulk composition measurement, the Ti, Fe, and Mn concentrations are near the nominal composition. The elemental concentrations of the matrix are close to TiFe, with Mn seemingly substituting on both Ti and Fe sites. Both the black and darker grey regions are rich in Ti and have a Mn concentration slightly higher than that of the matrix. For both regions, the composition is close to Ti_2Fe.

The interface of the matrix and second phase was investigated by line analysis (Figure 2b). The abundance of Ti slowly increases from the edge toward the center of the secondary region while Fe abundance decreases. Mn concentration is almost constant in both the matrix and the secondary phase. There is no indication of segregation at the edge.

The atomized $Ti_{0.488}Fe_{0.460}Mn_{0.052}$ alloy was exposed to hydrogen at room temperature under a pressure of 2000 kPa for 24 h. However, no hydrogen absorption was observed. Surface oxides are easily formed on TiFe alloys, which can hinder hydrogen absorption [25,38,41]. Therefore, this lack of hydrogen absorption is likely attributed to the long air exposure before hydrogenation. Previous studies have demonstrated that mechanical processing techniques, such as ball milling and cold rolling, could improve activation kinetics after air exposure by introducing cracks and generating fresh surfaces [24,29–35]. To address the activation issue, various mechanical processing methods were applied and compared

to the activation of gas-atomized $Ti_{0.488}Fe_{0.460}Mn_{0.052}$ alloy. These included cold rolling (5 passes), ball milling (10 min), and cold pressing. Figure 3 illustrates the morphology of the atomized and mechanically processed powders. Figure 3a,b show that the atomized powder consists of a mixture of spherical and irregularly shaped particles. The spherical particles range in size from less than 20 µm to 300 µm, while the irregularly shaped particles measure between 100 µm and 400 µm.

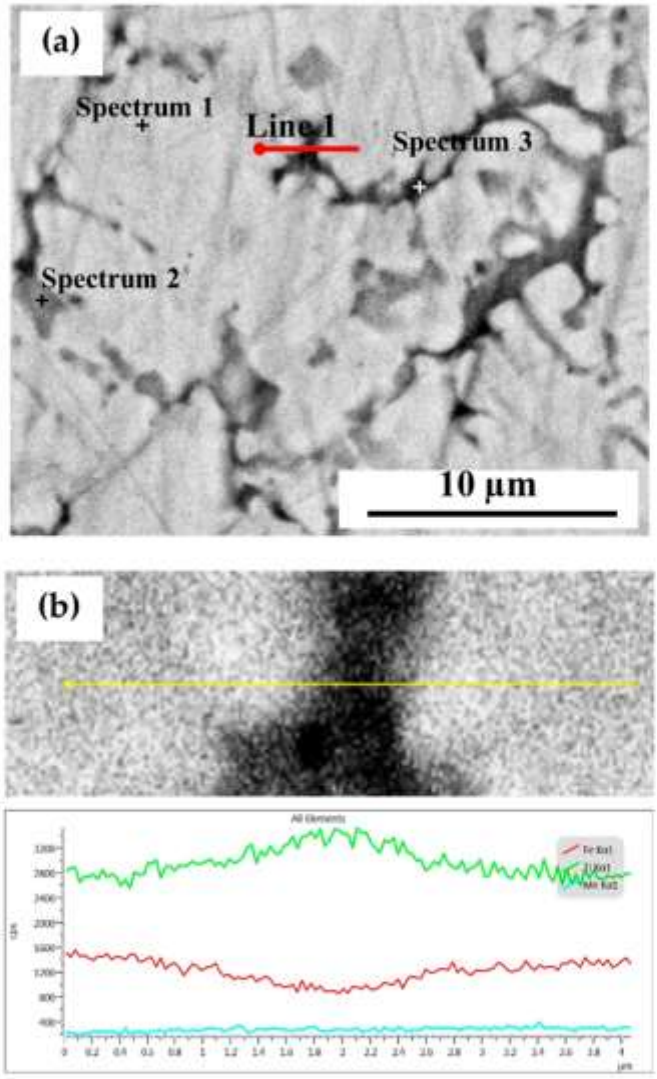

Figure 2. (**a**) High-magnification backscattered electron image of the EDS-analyzed regions of the atomized powder, (**b**) line analysis.

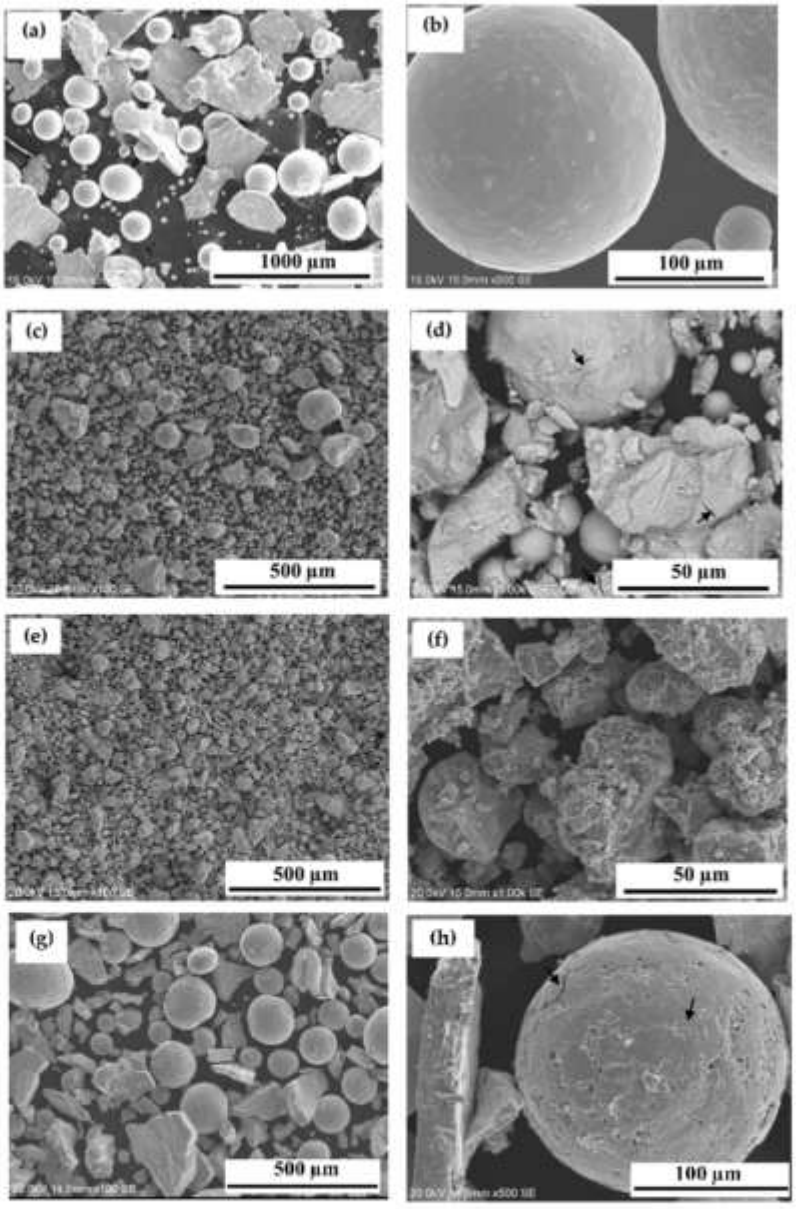

Figure 3. Morphology of gas-atomized powder (**a**,**b**); mechanically processed powders after 5 passes of cold rolling (**c**,**d**), 10 min of ball milling (**e**,**f**), and cold pressing (**g**,**h**).

After five passes of cold rolling, the average particle size decreased significantly due to the fragmentation of larger particles under mechanical deformation (Figure 3c). Most of the particles were very small, with sizes below 20 µm. However, some larger particles, approximately 100 µm in size, could still be observed, indicating that the fragmentation process is not entirely uniform. Figure 3d further highlights the formation of cracks and

highly fragmented particles, which become more evident at higher magnification. The cracks are marked with arrows.

Ball milling also resulted in the breakdown of particles into finer, irregularly shaped particles (Figure 3e,f). In contrast, cold pressing did not significantly reduce the average particle size (Figure 3g). However, a higher-magnification image (Figure 3h) reveals the presence of numerous cracks on both spherical and irregular particles.

The XRD patterns of atomized $Ti_{0.488}Fe_{0.460}Mn_{0.052}$ and mechanically processed samples before hydrogenation are presented in Figure 4. In addition, the XRD pattern of atomized TiFe is shown as reference sample. In all cases, only the TiFe phase is seen with no indication of other phases. As shown in Figure 1, the secondary regions exhibit a thin, filamentous structure and are present in a relatively small quantity compared to the matrix. Due to its limited volume and morphology, the diffraction intensity of these secondary phases was weak. Similarly, surface oxides typically form only a very thin layer (often just a few nanometers thick) on the powder surface. Because they are so thin and not very abundant, their XRD Bragg's peaks are very weak and broad, making them hard to distinguish from the background.

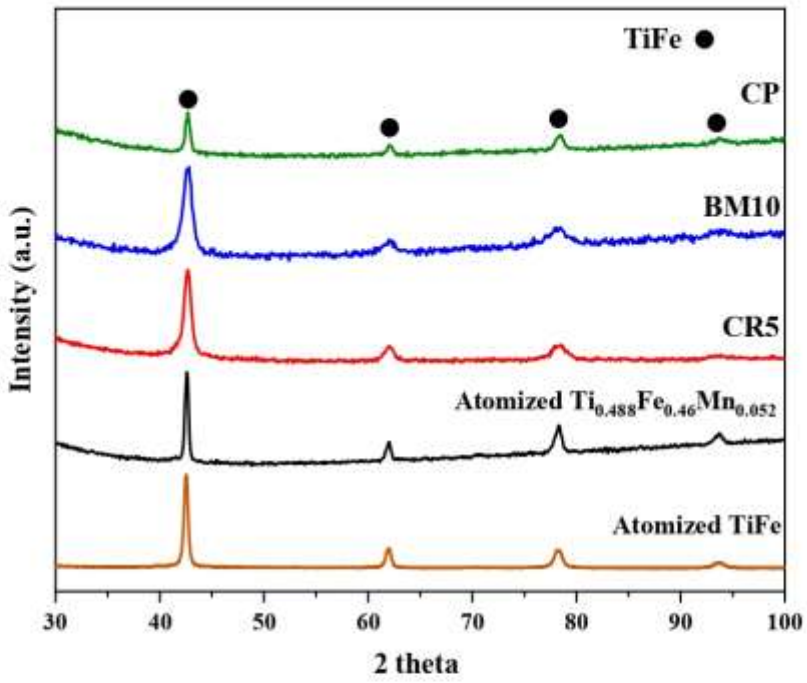

Figure 4. XRD patterns of gas-atomized powder and mechanically processed powders (5CR-10BM-CP) before hydrogenation.

Table 2 summarizes the Rietveld refinement results based on the XRD patterns of Figure 4. As the TiFe pattern was taken on a different diffractometer, we could not perform Rietveld's refinement on this one using the fundamental parameters. However, the lattice parameter of TiFe phase in reference TiFe alloys was 2.97971 (6) Å. Substituting Mn by Fe led to increase in lattice parameter to 2.9828 (4). The lattice parameters remained nearly constant across atomized $Ti_{0.488}Fe_{0.460}Mn_{0.052}$ and mechanically processed samples. However, a reduction in crystallite size and an increase in microstrains were observed

after mechanical processing, which can be attributed to the introduction of defects and dislocations in the crystal lattice. Among the samples, the ball-milled powder displayed the smallest crystallite size and the highest microstrain, whereas the cold-pressed sample exhibited the largest crystallite size and the lowest microstrain.

Table 2. Rietveld's refinement of TiFe phase. The error on the last significant digit is shown in parentheses.

Sample	Lattice Parameter (Å)	Crystallite Size (nm)	Microstrain (%)
As-Atomized	2.9828 (4)	44.0 (5)	0.132 (6)
CR5	2.9829 (6)	25.4 (2)	0.196 (2)
BM10	2.9838 (7)	8.6 (6)	0.302 (3)
CP	2.9822 (9)	29.6 (4)	0.142 (2)

Figure 5 shows the hydrogenation curves for all samples at room temperature and hydrogen pressure of 2000 kPa. Unlike the as-received (gas-atomized) $Ti_{0.488}Fe_{0.460}Mn_{0.052}$ sample, which did not absorb hydrogen, all mechanically processed samples successfully absorbed hydrogen. It is worth mentioning that pure TiFe alloy could not absorb hydrogen at room temperature and hydrogen pressure of 2000 kPa, even after mechanical processing, whereas the $Ti_{0.488}Fe_{0.460}Mn_{0.052}$ alloy readily absorbed hydrogen following mechanical processing.

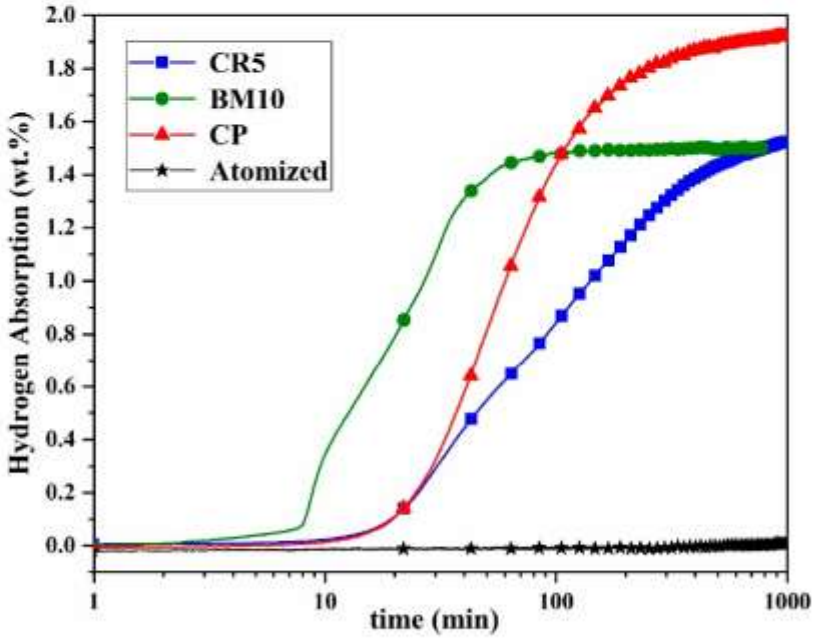

Figure 5. Hydrogenation curves at room temperature under 2000 kPa hydrogen pressure for as-received and mechanically processed powders.

The cold-pressed sample exhibited the highest hydrogen absorption capacity of 1.9 wt.%, and cold-rolled and ball-milled samples both reached 1.5 wt.% after 24 h. In terms of kinetics, the BM10 sample demonstrated the fastest hydrogenation, with an incu-

bation time of about 7 min, while both cold-rolled and cold-pressed samples had a longer incubation time of approximately 15 min.

Remarkably, despite the atomized powder being exposed to air for more than two years, each type of mechanical processing was able to activate the alloy and achieve good hydrogenation kinetics. For comparison, Modi et al. investigated the hydrogenation behavior of a $TiFe_{0.85}Mn_{0.15}$ alloy produced by arc melting [14]. After arc melting the alloy was subjected to ball milling for 30 min. Ball-milled alloy exhibited good kinetics and absorbed 1.2 wt.% hydrogen with no incubation time. However, after exposure to air for just 2 h, the alloy became oxidized and lost its hydrogen absorption capability. By heating to 300 °C under hydrogen pressure, reactivation was achieved, but with a prolonged incubation time of 40 min and a reduced capacity of 0.9 wt.%. In the present work, all mechanical treatments activated the alloy with shorter incubation times and higher hydrogen capacities compared to Modi et al., which can be attributed to microstructural differences between gas-atomized and arc-melted alloys.

Dematteis et al. further studied TiFe-alloys with partial substitution of Fe by Ti and Mn [16]. Samples with different compositions in the range from 48.8 at% to 54.1 at% Ti, and from 0 to 5.3 at% Mn were prepared by induction melting and subsequent annealing at 1000 °C for one week. Their results showed that activation generally required 5 MPa of hydrogen pressure and heating up to 400 °C. Only Ti-rich compositions could be activated under milder conditions (room temperature and 2500 kPa H_2). Although the alloy studied here is not Ti-rich, it was activated at room temperature and moderate pressure, which can be attributed to the finer microstructure of the gas-atomized material compared to induction-melted alloys.

The improvement in hydrogenation behavior after mechanical processing can be attributed to the refinement of the crystalline structure and the introduction of defects during deformation. As observed in Figure 3, mechanical processing induced cracks in the particles, likely facilitating hydrogen diffusion. The mechanical processing also introduces structural defects, such as vacancies and dislocations, which further enhance hydrogen transport within the material [42]. Rietveld refinement analysis revealed a decrease in crystallite size after mechanical processing, which corresponded to an increase in grain boundary density. These grain boundaries could serve as pathways that facilitate hydrogen diffusion [24,32,43]. Consequently, the hydrogenation kinetics improve after mechanical processing due to the combined effects of particle fragmentation, reduction in crystallite size, and the formation of grain boundaries.

As previously mentioned, the ball-milled sample not only exhibited the shortest incubation time but also demonstrated the fastest hydrogenation kinetics. As shown in Table 2, the BM10 sample had the smallest crystallite size, which implies a higher grain boundary density. Grain boundaries can facilitate hydrogen diffusion and act as nucleation sites for hydride formation [44]. In the study of Emami et al., it was reported that ball milling leads to the formation of nanograins, and the nanograin boundaries act as effective pathways for hydrogen diffusion [32].

Beyond the kinetics, differences in hydrogen storage capacity among the samples indicate the influence of mechanical processing on hydrogen storage behavior. As shown in Figure 5, the cold-pressed sample exhibited the highest capacity of 1.9 wt.% ± 0.1 wt.%. This value agrees with the nominal hydrogen capacity of TiFe alloy (1.86 wt.%).

According to the hydrogenation curves in Figure 5, after 1000 min, the cold-rolled sample continues to absorb hydrogen at a very slow rate, while the ball-milled sample has already reached its maximum capacity (1.5 wt.%). This indicates that the ball-milled sample had a lower overall capacity compared to the cold-pressed one. The reduced capacity of the ball-milled sample may be attributed to the crystallite size. As previously

discussed, the BM10 sample had the smallest crystallite size, resulting in a higher density of grain boundaries. Lv et al. found that as ball milling time increased and crystallite size decreased, the hydrogen storage capacity decreased [43]. They proposed that although grain boundaries facilitate hydrogen diffusion, they do not store hydrogen themselves. This may explain the lower overall capacity of the ball-milled sample, despite its faster kinetics and shorter incubation time.

Regarding the cold-rolled sample, the loss of capacity may be explained by the formation of oxides as the cold rolling was performed in the air. To verify this hypothesis, cold rolling was performed under both air and argon atmospheres for 5, 10, and 20 passes to compare the influence of rolling atmosphere on the hydrogenation behavior.

Figure 6 shows hydrogenation curves at room temperature and hydrogen pressure of 2000 kPa for cold-rolled samples in the air. After 5 CR in the air, absorption started after 15 min of incubation time. With 10 CR in air incubation time was increased to 35 min. After 20 CR in the air, the sample was not activated in 24 h. The difference in incubation time could be related to the surface condition of the materials. Increasing cold rolling passes in the air may lead to surface oxidation that can act as barriers to hydrogen absorption. Sleiman et al. similarly reported that while the as-cast $Ti_1V_{0.9}Cr_{1.1}$ alloy could not be activated, a single cold rolling pass enabled immediate activation [45]. However, when the number of passes increased to six, the incubation time rose to about 10 min, the activation kinetics slowed, and the absorption capacity decreased.

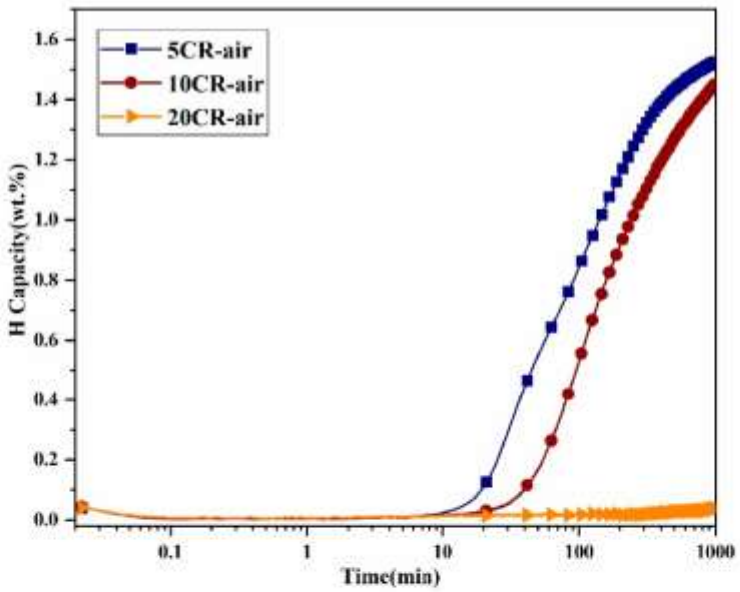

Figure 6. Activation curves of 5, 10, and 20 passes cold-rolled powders in air at RT/2000 kPa.

Figure 7 shows the first hydrogenation of samples cold rolled in argon. Compared to rolling in the air, the incubation time is shorter. After 5 and 10 rolling passes, the incubation times were only 3 and 4 min, respectively. The hydrogen absorption capacity after 24 h was about 1.5 wt.%, which is like the samples rolled in the air. The most notable difference appeared after 20 passes; while the 20CR-air sample showed no activation within 24 h, the 20CR-argon sample began absorbing hydrogen after 55 min and reached a capacity of 1.6 wt.% after 24 h. Even under argon atmosphere, increasing the number of cold rolling

passes to 20 resulted in a longer incubation time (55 min), similar to what was observed for cold-rolled samples in the air. This suggests that, regardless of oxidation, excessive deformation may hinder the first hydrogenation. This could be attributed to the excessive plastic deformation induced by multiple passes. As the number of passes increases, the material accumulates a higher density of dislocations, defects, and internal stresses, which can disrupt hydrogen diffusion.

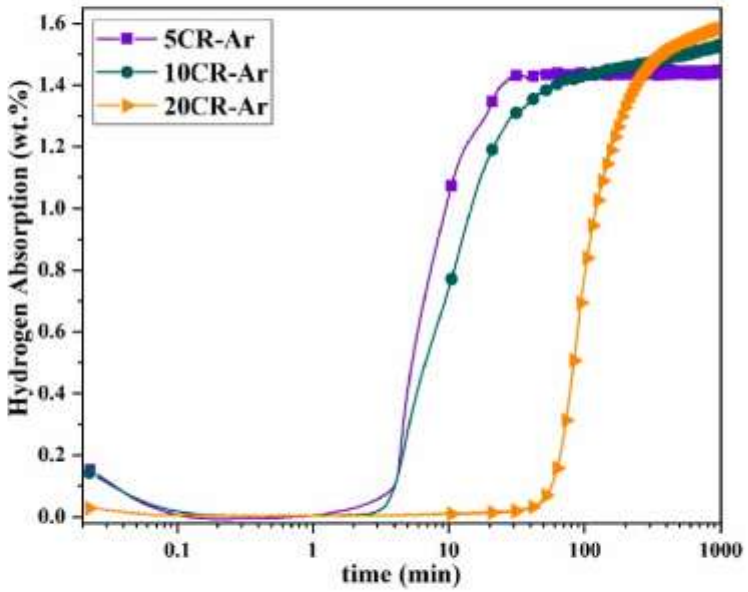

Figure 7. Activation curves of 5, 10, and 20 passes cold-rolled powders in argon at RT/2000 kPa.

The crystal structure of cold rolled samples in the air and argon was investigated by X-ray diffraction, and the patterns are shown in Figure 8. The corresponding Rietveld refinement data are summarized in Table 3. We see that increasing the number of rolling passes led to a reduction in crystallite size and increasing microstrain. The effect was the same for the samples rolled in argon compared to the ones rolled in the air. In fact, the crystal parameters were essentially the same for the air and argon cases. Therefore, the difference in incubation time between air and argon rolling atmosphere could not be attributed to a different crystal structure. It should be due to some surface effect that could not be seen by X-ray diffraction due to the large penetration depth of the oxides. The possible Ti, Fe and TiFe oxides have penetration depth between 2 and 10 microns. Considering that the surface oxide should have a thickness of nm, it is understandable that the presence of oxides could not be seen by X-ray diffraction. We are planning to perform XPS to obtain a better understanding of the surface composition.

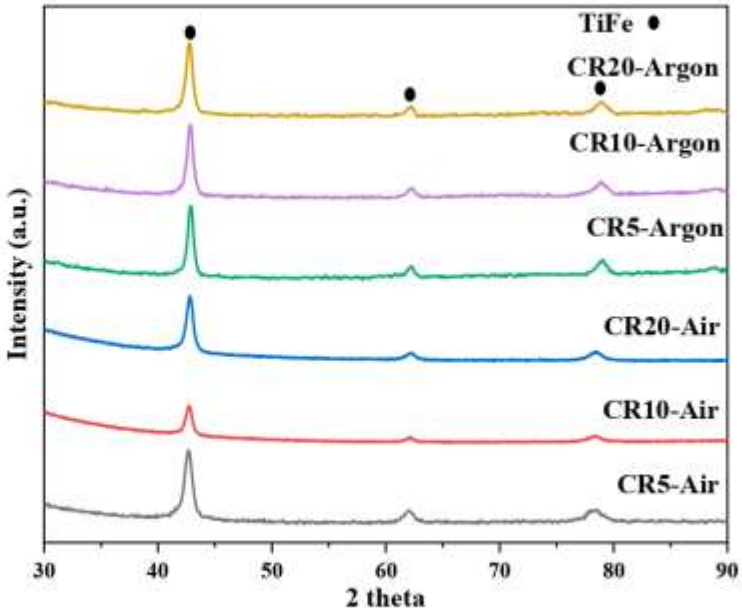

Figure 8. XRD patterns of cold rolled samples in air and argon before hydrogenation.

Table 3. Rietveld's refinement of TiFe phase in cold rolled samples in air and argon. The error on the last significant digit is shown in parentheses.

Sample	Lattice Parameter (Å)	Crystallite Size (nm)	Microstrain (%)
5CR-Air	2.9829 (6)	25.4 (2)	0.196 (2)
10CR-Air	2.9839 (5)	14.3 (5)	0.213 (7)
20CR-Air	2.9841 (3)	12.1 (3)	0.235 (1)
5CR-Argon	2.9829 (9)	25.1 (8)	0.194 (1)
10CR-Argon	2.9831(3)	14.4 (8)	0.228 (1)
20CR-Argon	2.9832 (2)	12.7 (6)	0.231 (1)

4. Conclusions

The effects of cold rolling, ball milling, and cold pressing on the microstructure and hydrogen storage properties of $Ti_{0.488}Fe_{0.460}Mn_{0.052}$ alloy were investigated. Cold pressing resulted in the highest hydrogen absorption capacity among the three methods, while ball milling significantly improved the first hydrogenation kinetics compared to cold rolling and cold pressing. Increasing the number of cold rolling passes in the air reduced hydrogen absorption kinetics, probably because of surface oxidation. Cold rolling under argon atmosphere produced a fast first hydrogenation. However, a higher number of passes in argon led to longer incubation times, suggesting that excessive deformation may hinder the first hydrogenation. These results suggest that combining different mechanical treatments could be explored in future studies to optimize both capacity and hydrogenation rate.

Author Contributions: Conceptualization, S.H. and J.H.; validation, S.H. and J.H.; formal analysis, S.H.; investigation, S.H.; writing—original draft preparation, S.H.; writing—review and editing, S.H.,

C.S. and J.H.; supervision, J.H.; project administration, J.H. and C.S. All authors have read and agreed to the published version of the manuscript.

Funding: This research was funded by MITACS Project IT Number: IT28247/Canadian Academic Institution: UQTR/Canadian Academic Supervisor: Jacques Huot/Partner Organization: GKN (Hoeganaes Corporation).

Data Availability Statement: The data presented in this study are available on request from the corresponding author.

Acknowledgments: Seyedehfaranak Hosseinigourajoubi acknowledges GKN Hoeganaes Innovation Centre and Advanced Materials and MITACS for the fellowship.

Conflicts of Interest: Author, Chris Schade, is employed by GKN Company, which provided funding and supplied the samples for this study. All other authors declare no conflict of interest.

Abbreviations

The following abbreviations are used in this manuscript:

CR	Cold Rolling
BM	Ball Milling
CP	Cold Pressing
HPT	High-Pressure Torsion

References

1. Bernauer, O.; Halene, C. Properties of metal hydrides for use in industrial applications. *J. Less Common Met.* **1987**, *131*, 213–224. [CrossRef]
2. Sakintuna, B.; Lamari-Darkrim, F.; Hirscher, M. Metal hydride materials for solid hydrogen storage: A review. *Int. J. Hydrogen Energy* **2007**, *32*, 1121–1140. [CrossRef]
3. Schlapbach, L.; Züttel, A. Hydrogen-storage materials for mobile applications. *Nature* **2001**, *414*, 353–358. [CrossRef]
4. Zhu, H.Y.; Wu, J.; Wang, Q.D. Reactivation behaviour of TiFe hydride. *J. Alloys Compd.* **1994**, *215*, 91–95. [CrossRef]
5. Haraki, T.; Oishi, K.; Uchida, H.; Miyamoto, Y.; Abe, M.; Kokaji, T.; Uchida, S. Properties of hydrogen absorption by nano-structured FeTi alloys. *Int. J. Mater. Res.* **2008**, *99*, 507–512. [CrossRef]
6. Lanyin, S.; Fangjie, L.; Deyou, B. An advanced TiFe series hydrogen storage material with high hydrogen capacity and easily activated properties. *Int. J. Hydrogen Energy* **1990**, *15*, 259–262. [CrossRef]
7. Zadorozhnyy, V.; Klyamkin, S.; Zadorozhnyy, M.; Bermesheva, O.; Kaloshkin, S. Hydrogen storage nanocrystalline TiFe intermetallic compound: Synthesis by mechanical alloying and compacting. *Int. J. Hydrogen Energy* **2012**, *37*, 17131–17136. [CrossRef]
8. Schober, T. On the activation of FeTi for hydrogen storage. *J. Less Common Met.* **1983**, *89*, 63–70. [CrossRef]
9. Bläsius, A.; Gonster, U. Mössbauer surface studies on Tife hydrogen storage material. *Appl. Phys.* **1980**, *22*, 331–332. [CrossRef]
10. Jai-Young, L.; Park, C.N.; Pyun, S.M. The activation processes and hydriding kinetics of FeTi. *J. Less Common Met.* **1983**, *89*, 163–168. [CrossRef]
11. Reilly, J.J.; Wiswall, R.H. Formation and properties of iron titanium hydride. *Inorg. Chem.* **1974**, *13*, 218–222. [CrossRef]
12. Dematteis, E.; Berti, N.; Cuevas, F.; Latroche, M.; Baricco, M. Substitutional effects in TiFe for hydrogen storage: A comprehensive review. *Mater. Adv.* **2021**, *2*, 2524–2560. [CrossRef]
13. Padhee, S.P.; Roy, A.; Pati, S. Role of Mn-substitution towards the enhanced hydrogen storage performance in FeTi. *Int. J. Hydrogen Energy* **2022**, *47*, 9357–9371. [CrossRef]
14. Modi, P.; Aguey-Zinsou, K.-F. Titanium-iron-manganese ($TiFe_{0.85}Mn_{0.15}$) alloy for hydrogen storage: Reactivation upon oxidation. *Int. J. Hydrogen Energy* **2019**, *44*, 16757–16764. [CrossRef]
15. Yuan, Z.-M.; Qi, Z.; Zhai, T.-T.; Wang, H.-Z.; Wang, H.-Y.; Zhang, Y.-H. Effects of La substitution on microstructure and hydrogen storage properties of Ti–Fe–Mn-based alloy prepared through melt spinning. *Trans. Nonferrous Met. Soc. China* **2021**, *31*, 3087–3095. [CrossRef]
16. Dematteis, E.M.; Dreistadt, D.M.; Capurso, G.; Jepsen, J.; Cuevas, F.; Latroche, M. Fundamental hydrogen storage properties of TiFe-alloy with partial substitution of Fe by Ti and Mn. *J. Alloys Compd.* **2021**, *874*, 159925. [CrossRef]
17. Jung, J.Y.; Lee, S.-I.; Faisal, M.; Kim, H.; Lee, Y.-S.; Suh, J.-Y.; Shim, J.-H.; Huh, J.-Y.; Cho, Y.W. Effect of Cr addition on room temperature hydrogenation of TiFe alloys. *Int. J. Hydrogen Energy* **2021**, *46*, 19478–19485. [CrossRef]

18. Park, K.B.; Ko, W.-S.; Fadonougbo, J.O.; Na, T.-W.; Im, H.-T.; Park, J.-Y.; Kang, J.-W.; Kang, H.-S.; Park, C.-S.; Park, H.-K. Effect of Fe substitution by Mn and Cr on first hydrogenation kinetics of air-exposed TiFe-based hydrogen storage alloy. *Mater. Charact.* **2021**, *178*, 111246. [CrossRef]
19. Komedera, K.; Michalik, J.; Sworst, K.; Gondek, Ł. Structure, Microstructure and Hyperfine Interactions in Hf- and Ni-Substituted TiFe Alloy for Hydrogen Storage. *Acta Phys. Pol. A* **2024**, *146*, 215–221. [CrossRef]
20. Sun, H.; Yan, Z.; Han, Z.; Li, J.; Zhai, T.; Yuan, Z.; Li, T.; Xu, J.; Zhang, Y. Hydrogen storage properties of TiFe-based composite with Ni addition. *Heliyon* **2024**, *10*, e41022. [CrossRef]
21. Chung, H.S.; Lee, J.Y. Effect of partial substitution of Mn and Ni for Fe in FeTi on hydriding kinetics. *Int. J. Hydrogen Energy* **1986**, *11*, 335–339. [CrossRef]
22. Fruchart, D.; Commandré, M.; Sauvage, D.; Rouault, A.; Tellgren, R. Structural and activation process studies of Fe Ti-like hydride compounds. *J. Less Common Met.* **1980**, *74*, 55–63. [CrossRef]
23. Lv, P.; Liu, Z.; Dixit, V. Improved hydrogen storage properties of TiFe alloy by doping (Zr+2V) additive and using mechanical deformation. *Int. J. Hydrogen Energy* **2019**, *44*, 27843–27852. [CrossRef]
24. Manna, J.; Tougas, B.; Huot, J. Mechanical activation of air exposed TiFe + 4 wt% Zr alloy for hydrogenation by cold rolling and ball milling. *Int. J. Hydrogen Energy* **2018**, *43*, 20795–20800. [CrossRef]
25. Li, C.; Gao, X.; Liu, B.; Wei, X.; Zhang, W.; Lan, Y.; Wang, H.; Yuan, Z. Effects of Zr doping on activation capability and hydrogen storage performances of TiFe-based alloy. *Int. J. Hydrogen Energy* **2023**, *48*, 2256–2270. [CrossRef]
26. Patel, A.K.; Sharma, P.; Huot, J. Effect of annealing on microstructure and hydrogenation properties of TiFe + X wt% Zr (X = 4, 8). *Int. J. Hydrogen Energy* **2018**, *43*, 6238–6243. [CrossRef]
27. Patel, A.; Huot, J.; Sharma, P. Hydrogen storage properties of TiFe + X wt.% Zr, V (X = 0, 4) alloys. In Proceedings of the 2016 Canadian Association of Physicists (CAP) Congress, Ottawa, ON, Canada, 13–17 June 2016. [CrossRef]
28. Jain, P.; Gosselin, C.; Huot, J. Effect of Zr, Ni and Zr7Ni10 alloy on hydrogen storage characteristics of TiFe alloy. *Int. J. Hydrogen Energy* **2015**, *40*, 16921–16927. [CrossRef]
29. Ulate-Kolitsky, E.; Tougas, B.; Neumann, B.; Schade, C.; Huot, J. First hydrogenation of mechanically processed TiFe-based alloy synthesized by gas atomization. *Int. J. Hydrogen Energy* **2021**, *46*, 7381–7389. [CrossRef]
30. Vega, L.; Leiva, D.; Neto, R.L.; Silva, W.; Silva, R.; Ishikawa, T.; Kiminami, C.; Botta, W. Mechanical activation of TiFe for hydrogen storage by cold rolling under inert atmosphere. *Int. J. Hydrogen Energy* **2018**, *43*, 2913–2918. [CrossRef]
31. Oliveira, V.B.; Beatrice, C.A.G.; Leal, R.M.; Silva, W.B.; Pessan, L.A.; Botta, W.J.; Leiva, D.R. Hydrogen absorption/desorption behavior of a cold-rolled TiFe intermetallic compound. *Mater. Res.* **2021**, *24*, e20210204. [CrossRef]
32. Emami, H.; Edalati, K.; Matsuda, J.; Akiba, E.; Horita, Z. Hydrogen storage performance of TiFe after processing by ball milling. *Acta Mater.* **2015**, *88*, 190–195. [CrossRef]
33. Vega, L.E.R.; Leiva, D.R.; Leal Neto, R.M.; Silva, W.B.; Silva, R.A.; Ishikawa, T.T.; Kiminami, C.S.; Botta, W.J. Improved ball milling method for the synthesis of nanocrystalline TiFe compound ready to absorb hydrogen. *Int. J. Hydrogen Energy* **2020**, *45*, 2084–2093. [CrossRef]
34. Abe, M.; Kuji, T. Hydrogen absorption of TiFe alloy synthesized by ball milling and post-annealing. *J. Alloys Compd.* **2007**, *446–447*, 200–203. [CrossRef]
35. Tajima, I.; Abe, M.; Uchida, H.; Hattori, M.; Miyamoto, Y.; Haraki, T. Hydrogen sorption kinetics of FeTi alloy with nano-structured surface layers. *J. Alloys Compd.* **2013**, *580*, S33–S35. [CrossRef]
36. Edalati, K.; Matsuda, J.; Arita, M.; Daio, T.; Akiba, E.; Horita, Z. Mechanism of activation of TiFe intermetallics for hydrogen storage by severe plastic deformation using high-pressure torsion. *Appl. Phys. Lett.* **2013**, *103*, 143902. [CrossRef]
37. Gómez, E.I.L.; Edalati, K.; Antiqueira, F.J.; Coimbrão, D.D.; Zepon, G.; Leiva, D.R.; Ishikawa, T.T.; Cubero-Sesin, J.M.; Botta, W.J. Synthesis of Nanostructured TiFe Hydrogen Storage Material by Mechanical Alloying via High-Pressure Torsion. *Adv. Eng. Mater.* **2020**, *22*, 2000011. [CrossRef]
38. Shang, H.; Li, Y.; Li, C.; Hu, D.; Yang, G.; Li, J.; Zhang, Y.; Zhang, Y. Activation, modification and application of TiFe-based hydrogen storage alloys. *Int. J. Hydrogen Energy* **2024**, *96*, 274–299. [CrossRef]
39. Chiang, C.H.; Chin, Z.H.; Perng, T.P. Hydrogenation of TiFe by high-energy ball milling. *J. Alloys Compd.* **2000**, *307*, 259–265. [CrossRef]
40. Patel, A.K.; Tougas, B.; Sharma, P.; Huot, J. Effect of cooling rate on the microstructure and hydrogen storage properties of TiFe with 4 wt% Zr as an additive. *J. Mater. Res. Technol.* **2019**, *8*, 5623–5630. [CrossRef]
41. Lee, S.-Y.; Ha, T.; Suh, J.-Y.; Kim, D.-I.; Lee, Y.-S.; Shim, J.-H. Orientation relationship between TiFeH and TiFe phases in AB-type Ti–Fe–V–Ce hydrogen storage alloy. *J. Alloys Compd.* **2024**, *983*, 173943. [CrossRef]
42. Edalati, K.; Matsuo, M.; Emami, H.; Itano, S.; Alhamidi, A.; Staykov, A.; Smith, D.J.; Orimo, S.-I.; Akiba, E.; Horita, Z. Impact of severe plastic deformation on microstructure and hydrogen storage of titanium-iron-manganese intermetallics. *Scr. Mater.* **2016**, *124*, 108–111. [CrossRef]

43. Lv, P.; Guzik, M.N.; Sartori, S.; Huot, J. Effect of ball milling and cryomilling on the microstructure and first hydrogenation properties of TiFe+4wt.% Zr alloy. *J. Mater. Res. Technol.* **2019**, *8*, 1828–1834. [CrossRef]
44. Gubicza, J. (Ed.) Chapter 11—Relationship Between Microstructure and Hydrogen Storage Properties of Nanomaterials. In *Defect Structure and Properties of Nanomaterials*, 2nd ed.; Woodhead Publishing: Cambridge, UK, 2017; pp. 297–315. [CrossRef]
45. Sleiman, S.; Aliouat, A.; Huot, J. Enhancement of First Hydrogenation of $Ti_1V_{0.9}Cr_{1.1}$ BCC Alloy by Cold Rolling and Ball Milling. *Materials* **2020**, *13*, 3106. [CrossRef] [PubMed]

Article 2

metals

MDPI

Article

The Effect of Annealing on the First Hydrogenation Behavior of Atomized $Ti_{48.8}Fe_{46.0}Mn_{5.2}$ Alloy

Seyedehfaranak Hosseinigourajoubi [1], Chris Schade [2] and Jacques Huot [1,*]

[1] Hydrogen Research Institute, Université du Québec à Trois-Rivières, Trois-Rivières, QC G9A5H7, Canada; seyedeh.faranak.hosseini.gourajoubi@uqtr.ca
[2] GKN Hoeganaes Innovation Centre & Advanced Materials, Cinnaminson, NJ 08077, USA; chris.schade@hoeganaes.com
* Correspondence: jacques.huot@uqtr.ca

Abstract: In this paper, we report the effect of annealing on the first hydrogenation behavior of $Ti_{48.8}Fe_{46.0}Mn_{5.2}$ alloy. This alloy was produced by gas atomization, and a portion of the powder was subjected to vacuum annealing at 1120 °C for 1 h. The goal was to investigate the usefulness of this atomized powder for hydrogen storage and also to investigate the effect of annealing. Scanning electron microscopy (SEM) images revealed that both atomized and annealed alloys exhibit a two-phase structure. The atomized alloy consists of a main TiFe matrix and a filamentous Ti_2Fe-like phase. After annealing, the microstructure is globular. In addition to the microstructure, there was a change in the chemical composition of the matrix and secondary phase after annealing. The first hydrogenation at room temperature of both atomized and annealed samples required cold rolling. However, the kinetics was much slower for the annealed sample compared to the atomized sample. After the first hydrogenation, the XRD analysis identified the main phases as TiFe, $TiFeH_{0.94}$, and Ti_2FeH_3, indicating that both the TiFe and Ti_2Fe phases participated in hydrogen absorption during hydrogenation.

Keywords: TiFe alloy; hydrogen storage; metal hydride; first hydrogenation; annealing

Academic Editors: Nebojša Nikolić and Gabriele Mulas

Received: 26 November 2024
Revised: 29 January 2025
Accepted: 24 February 2025
Published: 26 February 2025

Citation: Hosseinigourajoubi, S.; Schade, C.; Huot, J. The Effect of Annealing on the First Hydrogenation Behavior of Atomized $Ti_{48.8}Fe_{46.0}Mn_{5.2}$ Alloy. *Metals* **2025**, *15*, 251. https://doi.org/10.3390/met15030251

1. Introduction

Hydrogen is gaining attention as a renewable energy carrier due to its versatility and clean energy potential. When it comes to hydrogen storage, a reliable and efficient method is crucial for the wide utilization of hydrogen. Solid-state storage in metal hydrides could be suitable for storing hydrogen for a variety of applications [1,2]. Among the many different types of metal hydrides, TiFe has shown great potential for hydrogen storage applications due to its reasonable hydrogen storage capacity of 1.86 wt.% at low pressure and room temperature. Furthermore, this alloy is made from cost-effective raw materials. However, a major challenge is the first hydrogenation, the so-called activation, which is usually slow at room temperature. This is most likely due to the formation of surface oxides that act as a barrier for hydrogen dissociation and absorption [3–6]. In the pioneering work of Reilly and Wiswall [7], the first hydrogenation was preceded by heating the alloy to over 400 °C for 30 min, either in a vacuum or at low hydrogen pressure, and then cooling it to room temperature and applying a high hydrogen pressure of approximately 6000 kPa. The process had to be repeated several times until the hydrogenation occurred in about 15 min. Since then, several studies have used this type of activation procedure for TiFe alloys [8–10].

In addition to the above-mentioned repeated heating process, the activation issue can be overcome by other approaches: the addition of transition elements such as Mn [11,12], Zr [13,14], Cr [15], V [16,17], and Y [18,19]; the addition of excess Ti in the stoichiometry [20]; and mechanical treatments [21–23]. Lv et al. studied the effects of doping, cold rolling, and forging on the microstructure and hydrogen storage properties of air-exposed TiFe + x wt.% (Zr + 2V) (x = 0, 4, 5, and 6) alloys [14]. They concluded that doping with (Zr + 2V) significantly improved the first hydrogenation kinetics of TiFe due to the formation of an hcp secondary phase, which can enhance the diffusion of hydrogen. Forging effectively reduced the incubation time and enhanced the first hydrogenation kinetics, while cold rolling improved the absorption kinetics but resulted in a lower hydrogen capacity.

Patel et al. investigated the effect of Zr and Mn on the microstructure and the first hydrogenation kinetics of TiFe alloy [24]. They concluded that the fastest kinetics and highest capacity were reached by doping with 2 wt% Mn and 4 wt% Zr. The enhanced activation kinetics was attributed to the presence of a large proportion of Ti_2Fe-type phase, potentially because this phase could act as a gateway, facilitating hydrogen entry into the TiFe phase.

Ulate-Kolitsky et al. investigated the first hydrogenation of both cold-rolled and ball-milled TiFe-based alloy synthesized by gas atomization [21]. Cold rolling was shown to be more effective than ball milling for the regeneration of air-exposed atomized powder. Edalati et al. have shown that mechanical processing using severe plastic deformation (SPD) is effective at accelerating the hydrogenation kinetics [23]. They attributed it to the diffusivity of hydrogen that can be enhanced because of the high dislocation and grain boundary density and high concentration of vacancies after SPD processing.

In this paper, the cold rolling method is used for the activation of $Ti_{48.8}Fe_{46.0}Mn_{5.2}$ alloy produced by gas atomization. Atomization is a method that is utilized by industries to produce commercial alloys. However, as this method involves rapid cooling, there are some concerns regarding the stability of the resulting phases. Moreover, atomized powders are often fragile and difficult to compact without heat treatment [25]. Therefore, it is crucial to understand the effects of annealing on the phase stability, microstructural evolution, and chemical composition. In addition, annealing can significantly affect the hydrogenation properties of metal hydrides. Abe and Kuji noted that the TiFe alloy prepared by the mechanical alloying method exhibited a lower plateau pressure and reduced hydrogen reversibility at room temperature. However, after annealing at 600 °C for 3 h, a wide plateau area could be obtained [26]. According to a study by Lee et al., the activation process of the TiFe compound can be facilitated by incorporating a small quantity of Cr or Mn as substitutes for Fe. However, when subjected to a homogenization treatment at 900 °C for 80 h, the activation rate decreased due to alterations in the amount and morphology of the secondary phase [27]. This indicates that annealing could improve the hydrogen absorption properties of the alloys by reducing the plateau pressure in the PCT curve. However, compositional and morphological changes after annealing may adversely affect activation. Additionally, for industrial applications, annealing for a long duration could be too costly. Therefore, the effects of a short annealing time on the microstructure and hydrogen storage properties of $Ti_{48.8}Fe_{46.0}Mn_{5.2}$ alloy synthesized by gas atomization were investigated.

2. Materials and Methods

The $Ti_{48.8}Fe_{46.0}Mn_{5.2}$ alloy was produced by GKN Hoeganaes Innovation Centre and Advanced Materials. The gas atomization was performed under pure argon with a VIGA-type furnace with a free-fall atomization ring configuration. After synthesis, the powder

was stored in the air. A portion of the atomized powder was vacuum annealed at 1120 °C for 1 h in a batch furnace.

The morphology and microstructure of the powder were analyzed using a Hitachi Su1510 scanning electron microscope (Hitachi High-Tech Canada, Inc., Toronto, ON, Canada) equipped with an EDX—Energy Dispersive X-ray spectrometer (Oxford instrument, Abingdon, UK). The crystal structure of the alloys was analyzed by X-ray diffraction (XRD) measurement carried out on a Bruker D8 Focus diffractometer (Madison, WI, USA) with CuKα radiation. The XRD patterns were analyzed by the Rietveld method using TOPAS software v 7.0 (Bruker, Madison, WI, USA) to determine the alloy's phase abundance, lattice parameter, and crystallite size [28].

Cold rolling was performed vertically in the air with a modified Durston DRM 130 rolling mill (High Wycombe, Buckinghamshire, UK). The powder was inserted between two 316 stainless steel plates to avoid contamination by the rolls. Samples were cold rolled for 5 passes (5 CR).

The sample's hydrogen capacities and absorption kinetics were evaluated using a homemade Sievert-type apparatus. One gram of powders was placed in a sample holder and evacuated for 15 min before kinetic measurements. The absorption measurements were taken at room temperature (25 °C) under 2000 kPa of hydrogen pressure or at 90 °C and a hydrogen pressure of 4500 kPa.

3. Results and Discussion

3.1. Microstructure

Figure 1 shows the backscattered electron micrographs of $Ti_{48.8}Fe_{46.0}Mn_{5.2}$ alloys in as-atomized (AS) and vacuum-annealed (VA) conditions. The microstructure reveals the presence of two distinct regions: a matrix (gray) and a darker gray region. In the as-atomized alloy, the darker regions have a filamentous structure, while in the VA sample, they are globular, forming distinct islands.

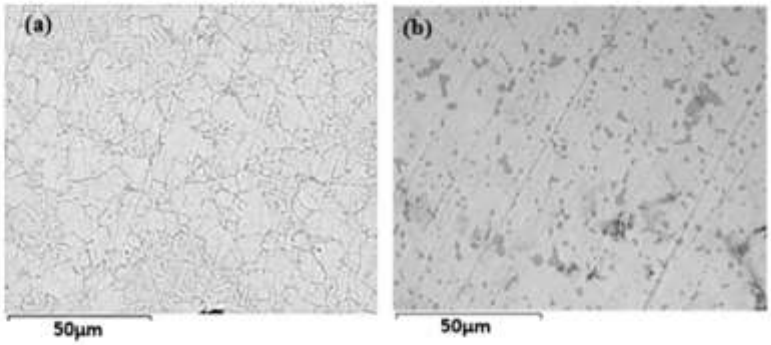

Figure 1. Backscattered electron micrographs of $Ti_{48.8}Fe_{46.0}Mn_{5.2}$ alloys: (**a**) as-atomized; (**b**) after vacuum annealing.

Figure 2 shows a higher magnification image of the atomized alloy analyzed by EDX. At this magnification, two distinct secondary regions are visible: a gray region and a black region. The chemical compositions of the bulk material and each region are shown in Table 1. The values represent the elemental compositions (in atomic percent, at.%) of different phases within the as-atomized alloy, determined by Energy Dispersive X-ray (EDX) analysis. These compositions reflect the distribution of Ti, Fe, and Mn in the matrix and secondary phases. We see that the bulk composition is slightly different than the

nominal one. Unfortunately, we do not have the 'error' on the nominal composition, but the difference is so small that we assume that the bulk composition is the real composition of the alloy. For the matrix region, the composition is TiFe with a small amount of Mn. Both the black and gray regions are Ti-rich and have a Mn concentration slightly higher than that in the matrix. In fact, the stoichiometry of these two regions is close to Ti_2Fe. The Ti_2Fe is not a stable phase and is not included in the ASM phase diagram [29]. Reilly et al. tried to synthesize Ti_2Fe in order to study its hydrogen absorption behavior [7]. They found that it exists above 1000 °C and that below this temperature, it decomposes to TiFe and Ti. Dong et al. prepared Ti_2Fe alloy using an arc furnace followed by remelting in an induction furnace and subsequent spin quenching [30]. They reported that the structure type of Ti_2Fe is Ti_2Ni. Guéguen et al. observed Ti_2Fe precipitates in the TiFe matrix after arc melting and annealing at 1000 °C for one week under argon atmosphere [17]. Therefore, despite not being a stable phase, Ti_2Fe could be relatively easy to obtain in Ti-Fe alloys under specific high-temperature conditions followed by rapid cooling or controlled annealing. In our study, the sample was produced by gas atomization, where the melt underwent rapid cooling. Additionally, the annealing temperature is comparable to the heat treatment temperatures in the above-mentioned studies. In the present investigation, the Ti_2Fe phase was obtained after just one hour of annealing.

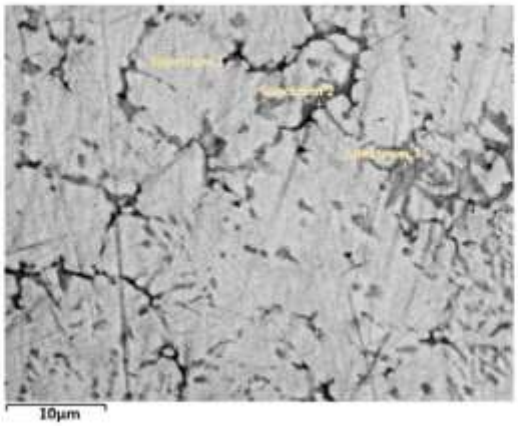

Figure 2. Higher magnification image of the microstructure of the as-atomized sample. Spectrum 1: matrix, spectrum 2: black region, spectrum 3: gray region.

Table 1. EDX analysis of phases of atomized alloys. Error on the last significant digit is indicated in parentheses.

Element	Nominal	Bulk	Matrix	Gray Region	Black Region
Ti	48.8	49.4 (3)	47.5 (5)	59.1 (3)	66.6 (2)
Fe	46	45.3 (4)	48.4 (6)	34.8 (2)	26.3 (4)
Mn	5.2	5.3 (2)	4.1 (5)	6.1 (3)	7.1 (1)

The higher magnification image of the vacuum-annealed sample (Figure 3) revealed a two-phase microstructure: a gray matrix and a dark secondary phase. The EDX analysis results are presented in Table 2. First, it shows that the bulk composition agrees with the bulk value given in Table 1, thus proving that the actual composition of the alloy given by the bulk values is the real one. Contrary to the matrix composition of the as-atomized alloy,

the matrix has a composition that is much closer to the TiFe stoichiometry with Fe being substituted by Mn. The dark phase composition is close to $(Ti, Mn)_2Fe$.

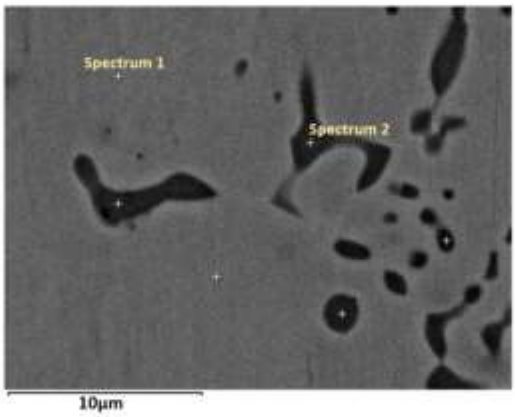

Figure 3. Higher magnification image of the microstructure of the vacuum annealed sample. Spectrum 1: matrix, spectrum 2: black region.

Table 2. EDX analysis showing the elemental composition of the matrix and secondary phase of vacuum-annealed alloy. Error on the last significant digit is indicated in parentheses.

Element	Nominal	Bulk	Matrix	Gray Region
Ti	48.8	48.9 (5)	49.5 (4)	62.2 (7)
Fe	46	46.1 (7)	45.5 (3)	33.1 (6)
Mn	5.2	5.0 (1)	5.0 (2)	4.7 (1)

Comparing the EDX results before and after annealing shows a change in the matrix composition. Before annealing, the matrix composition was $Ti_{47.5}Fe_{48.4}Mn_{4.1}$, while after annealing, the matrix composition was closer to the nominal composition, and Mn only substituted for Fe. This is very close to the composition given by Fruchart et al., who found that Mn substitutes for Fe in the TiFe crystal structure [31]. In the as-atomized sample, the secondary phase exhibited slightly different compositions, with two distinct regions, namely, gray and black, dispersed within the matrix. After annealing, only a black phase is dispersed into the matrix. The Ti and Fe concentrations in this region are close to the average of the gray and black regions in the as-atomized sample. However, after annealing, the Mn content in the secondary phase decreased compared to that in the as-atomized sample. The stoichiometry of the secondary phase is then $Ti_{1.87}Mn_{0.14}Fe$. Thus, for the TiFe matrix phase, Mn substitutes for Fe, while for the secondary Ti_2Fe phase, Mn substitutes for Ti.

The X-ray diffraction (XRD) patterns of the as-atomized and vacuum-annealed samples are shown in Figure 4. The main phase was identified as TiFe for both alloys. The peaks of the secondary phase could be observed in the XRD pattern after annealing, and it was identified as Ti_2Fe, which is consistent with the results of the EDS analysis. The absence of the Ti_2Fe phase in the AS sample can be attributed to the lower abundance and the thickness of this phase, which, as observed in SEM analysis, is only a fraction of a micron thick, while in the VA sample, the Ti_2Fe phase grows to a thickness of several microns. Considering the penetration depth of X-rays, the Ti_2Fe phase diffracts weakly in the AS sample, making it undetectable in the XRD pattern.

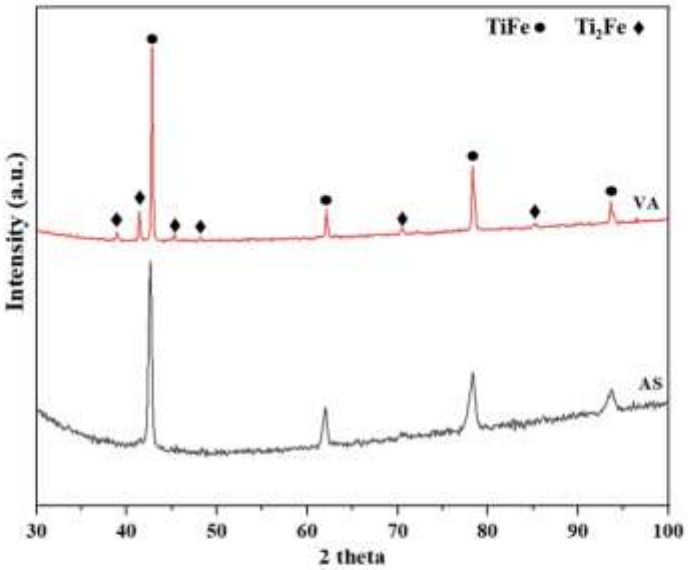

Figure 4. X-ray diffraction patterns of AS (as-atomized) and VA (vacuum-annealed) alloys.

Table 3 displays the phase fraction, lattice parameters, and crystallite size for each phase as determined by Rietveld refinement. For both the AS and VA samples, the lattice parameter is slightly bigger than the 2.97838 (6) Å of TiFe measured by Jung et al. [32].

Table 3. Rietveld refinement results of AS (as-atomized) and VA (vacuum-annealed) alloys. The error is shown in parentheses.

Sample	Phase	Phase Fraction (wt.%)	Lattice Parameter (Å)	Crystallite Size (nm)	Strain (%)
AS	TiFe	100	2.9828 (4)	82 (11)	0.65 (3)
VA	TiFe	77 (7)	2.9884 (6)	214 (14)	0.08 (3)
	Ti_2Fe	23 (7)	11.2362 (8)	140 (30)	0.2 (1)

From the Rietveld refinement, we evaluated the crystallite size and microstrain. The crystallite size is the coherent domain of the crystal structure. When the crystallite size is less than around 100 nm, this broadening is important enough to be seen on the Bragg peaks. The microstrain is due to a distribution of both tensile and compressive forces, which results in a broadening of the Bragg peak. This type of broadening depends on the diffraction angle and thus could be distinguished from the broadening due to crystallite size. The microstrain thus represents the variation in lattice parameters due to strain and is expressed as a % with respect to the average lattice parameter.

The annealing process also led to a noticeable increase in crystallite size and a reduction in the microstrain for the TiFe phase. This growth is easily explained by recrystallization because of the annealing temperature (1200 °C), which is close to the TiFe melting point (1317 °C). In addition to the increase in crystallite size, a reduction in the microstrain was observed. Microstrain is typically reduced during annealing, as the material's internal stresses decrease due to the reduction in defects.

3.2. First Hydrogenation

The hydrogenation was performed under two different conditions: at room temperature (21 °C) and 2000 kPa of hydrogen pressure and at 90 °C under 4500 kPa of hydrogen. For both conditions, the experiment ran for a period of 24 h. For both AS and VA samples, no hydrogen uptake was registered under these conditions. This could be due to the long air exposure before hydrogenation. In order to 'regenerate' the samples, they were subjected to five passes of cold rolling in the air. Previous studies have shown that this technique is effective in enabling the first hydrogenation of TiFe alloys. Ulate-Kolitsky et al. reported that five passes of cold rolling is efficient for the activation of TiFe alloys synthesized by gas atomization [21]. Manna et al. investigated the effect of air exposure on the $TiFe^{+4}$ wt.% Zr alloy and found that the seven-day air-exposed alloy did not absorb hydrogen, but cold rolling successfully led to the recovery of the alloy [33].

Figure 5 shows the curves of the first hydrogenation at RT/2000 kPa after five passes of cold rolling. The AS-5CR sample started to absorb hydrogen after about 1000 s, and it reached the capacity of 1.56 wt.% in 24 h. However, the VA-5CR sample did not absorb hydrogen in 24 h. The fast activation of the AS-5CR sample even at RT has shown that five passes of cold rolling is efficient for the regeneration of atomized TiFe(Mn) alloys.

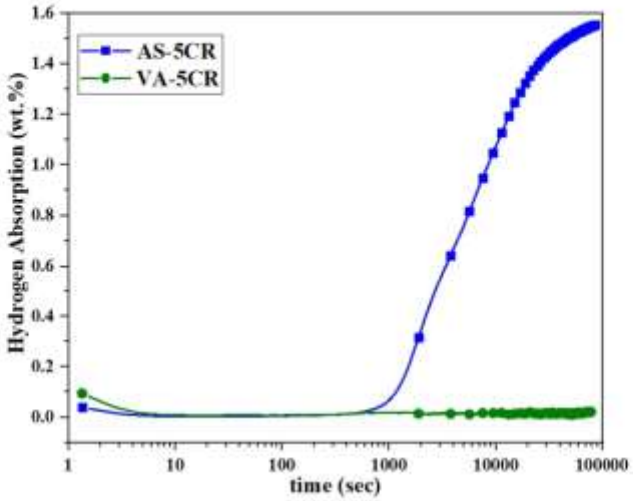

Figure 5. Activation curves of AS and VA samples after 5 CR at room temperature and a hydrogen pressure of 2000 kPa.

Since the VA-5CR sample did not activate at RT and 2000 kPa, the temperature was increased to 90 °C and the hydrogen pressure to 4500 kPa to investigate the effect of elevated pressure and temperature on its activation behavior. As seen in Figure 6, under these conditions, both samples absorbed hydrogen. The AS-5CR sample exhibited rapid kinetics, starting hydrogen absorption within 40 s and reaching a capacity of 1.42 wt.% after 24 h. In contrast, the annealed sample demonstrated a longer incubation time of 7200 s and finally achieved a capacity of 1.2 wt.% after 24 h.

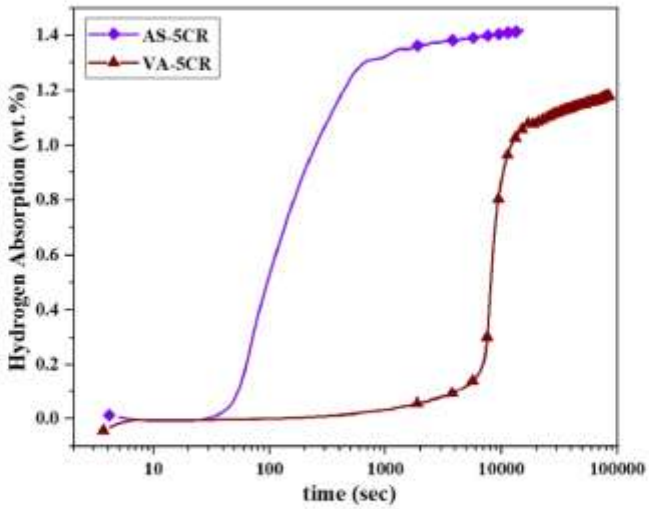

Figure 6. Activation curves of AS and VA samples after 5 CR at 90 °C and a hydrogen pressure of 4500 kPa.

Based on these results, it was determined that annealing is not appropriate for the TiFe alloy studied in this work. It seems that the hydrogenation behavior of the TiFe alloy is strongly influenced by the chemical composition and morphology of the secondary phase. After heat treatment, the phases' chemical compositions are marginally changed, but the morphology has been drastically changed from filamentous to globular. These changes may be responsible for the longer incubation time of the VA sample. The presence of a filamentous secondary phase seems to facilitate the hydrogen uptake by providing nucleation points for the hydride phase and a diffusion pathway for the hydrogen. After annealing, the secondary phase becomes more spheroidized, resulting in the reduction of pathways available for hydrogen within the alloy. This decrease in the interfacial region ultimately leads to a reduction in hydrogenation kinetics. In addition, SEM studies (Figures 2 and 3) revealed the presence of two distinct secondary regions within the TiFe matrix of the as-atomized alloy. However, after heat treatment, a dark secondary phase was observed in the matrix. EDS analysis (Tables 1 and 2) further confirmed the compositional changes following heat treatment. These compositional changes could potentially influence the hydrogen absorption behavior of the alloy.

Additionally, annealing also induced recrystallization in the primary TiFe phase, as evidenced by an increase in crystallite size and a reduction in microstrain determined from the Rietveld refinement of the XRD patterns (Table 3). While recrystallization reduces internal stresses, it also eliminates some of the grain boundaries that act as key diffusion pathways for hydrogen. Grain boundaries enhance hydrogen diffusion by serving as low-energy sites for hydrogen absorption and movement. The combination of a reduced interfacial area in the secondary phase and a decrease in the grain boundary density in the matrix likely explains the observed decline in hydrogenation performance [34,35].

Figure 7 presents the X-ray diffraction (XRD) patterns of the samples after cold rolling, and Table 4 shows the Rietveld refinement results. Comparing the results before and after cold rolling reveals that the cold rolling process reduced the crystallite size and increased the microstrain. Decreasing the crystallite size leads to more grain boundaries. Therefore, the reduction in crystallite size and formation of a fresh surface due to crushing during cold

rolling could lead to faster hydrogen absorption. The effectiveness of highly strained grain boundaries as effective trapping sites for hydrogen has been shown by Emami et al. [34]. Similarly, Lv et al. have shown that the grain boundaries formed by cold rolling could act as diffusion points for hydrogen [14].

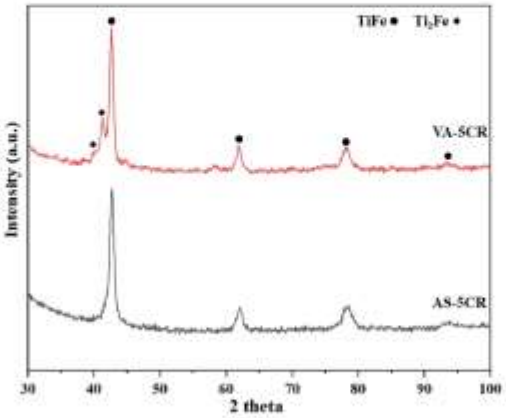

Figure 7. X-ray diffraction patterns of AS (as-atomized) and VA (vacuum-annealed) alloys after 5 passes of cold rolling.

Table 4. Rietveld refinement results of AS-5CR and VA-5CR. The error is shown in parentheses.

Sample	Phase	Phase Fraction Wt.%	Lattice Parameter (Å)	Crystallite Size (nm)	Strain (%)
AS-5CR	TiFe	100	2.991 (2)	17 (3)	1.0 (6)
VA-5CR	TiFe	70 (6)	2.9900 (1)	19 (6)	0.81 (8)
	Ti_2Fe	30 (6)	11.3330 (6)	10 (3)	0.10 (1)

Figure 8 shows the X-ray diffraction (XRD) patterns of AS and VA samples after activation at 90 °C and 4500 kPa. The corresponding phase fractions, lattice parameters, and crystallite sizes are presented in Table 5. In order to preserve the hydride state, after hydrogenation at 90° C, the sample was cooled to room temperature under hydrogen pressure. The diffraction pattern was registered in the air shortly after removing the sample from the sample holder. Upon analysis of the activated samples, XRD reveals the presence of the TiFe, $TiFeH_{0.94}$, and Ti_2FeH_X phases. The presence of the TiFe peak after activation in the XRD pattern indicates that the sample starts desorbing at room temperature and atmospheric pressure. The TiFe phase fraction was reduced due to the presence of the orthorhombic $TiFeH_{0.94}$ phase. This phase was identified by Reidinger et al. on the desorption of TiFe hydride [36]. The lattice parameters of the $TiFeH_{0.94}$ phase presented in Table 5 are close to the lattice parameters reported by Reidinger et al.

For the VA sample, the unit cell volume of Ti_2Fe before hydrogenation is 1456 $Å^3$, which expands to 1803 $Å^3$ after hydrogenation. This corresponds to a volume expansion of 24%. This is consistent with previous investigations by Ulate-Kolitsky et al. [20], who reported a volume expansion of 21%. The stoichiometry of the Ti_2FeH_X phase can be determined by analyzing the increase in unit cell volume resulting from hydrogen uptake. The volume increase is 347 $Å^3$, and there are 32 formula units per unit cell. Therefore, the volume variation per formula unit is estimated to be about 11 $Å^3$. Based on the assumption that the volume of a single hydrogen atom is around 2.9 $Å^3$ [37], the resulting stoichiometry

is approximately Ti_2FeH_3 (~1.9 wt.%). As this sample is made up of 20% Ti_2FeH_3, the contribution to the total hydrogen capacity is 0.38 wt.%. The $TiFeH_{0.94}$ phase makes up 40% of the sample and contains 1 wt.% hydrogen. Therefore, its contribution to the total capacity is 0.4 wt.% hydrogen. Consequently, the overall hydrogen content is about 0.8 wt.%. Given the hydrogen absorption capacity of 1.2 wt.%, this shows that the sample partially desorbed before the X-ray diffraction measurement.

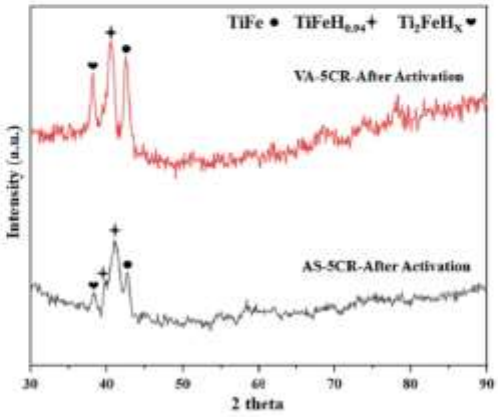

Figure 8. X-ray diffraction patterns of AS (as-atomized) and VA (vacuum-annealed) alloys after activation.

Table 5. Rietveld refinement results of AS (as-atomized) and VA (vacuum-annealed) alloys after activation. The error is shown in parentheses.

Sample	Phase	Phase Fraction (%)	Lattice Parameter (Å)	Crystallite Size (nm)
AS-5CR-After Activation	$TiFeH_{0.94}$	73 (11)	a = 4.37 (1) b = 3.08 (1) c = 4.52 (1)	11 (2)
	Ti_2FeHx	11 (5)	12.23 (2)	17 (5)
	TiFe	16 (8)	2.994 (4)	20 (3)
VA-5CR-After Activation	$TiFeH_{0.94}$	40 (13)	a = 4.51 (1) b = 3.11 (1) c = 4.40 (3)	15 (4)
	Ti_2FeH_x	20 (6)	12.17 (2)	22 (7)
	TiFe	40 (13)	2.986 (5)	16 (5)

In the activated AS sample, assuming the Ti_2FeH_X phase has a stoichiometry of approximately Ti_2FeH_3, the 11 wt.% of this phase contributes about 0.2 wt.% hydrogen. The sample also contains 73% $TiFeH_{0.94}$, which contributes to 0.7 wt.% hydrogen. Consequently, the total hydrogen content in the sample is 0.9 wt.%. Considering the hydrogen absorption capacity of 1.4 wt.% (Figure 6), the amount of desorbed hydrogen is 0.5 wt.%. It should be pointed out that the desorbed capacities of the VA and AS samples are almost the same, at 0.4 wt% and 0.5 wt.%, respectively.

4. Conclusions

- The microstructure and first hydrogenation of $Ti_{48.8}Fe_{46.0}Mn_{5.2}$ alloy prepared by gas atomization, before and after vacuum annealing, have been investigated.
- The microstructure of the alloy before and after annealing consists of a TiFe matrix and a secondary Ti_2Fe-like phase. The secondary Ti_2Fe phase exhibited a filamentous microstructure in the atomized alloy, whereas it appeared more globular in the annealed sample.
- Both the atomized and annealed alloys needed prior mechanical processing by cold rolling to absorb hydrogen. After five cold rolling passes, the atomized sample absorbed 1.56 wt.% hydrogen at room temperature and a hydrogen pressure of 2000 kPa. However, the annealed sample could not be activated in 24 h under the same conditions.
- Both the atomized and annealed samples absorbed hydrogen at 90 °C and a hydrogen pressure of 4500 kPa, but the atomized sample had faster kinetics and a higher capacity.
- Annealing after atomization had a negative effect on the activation process, probably due to recrystallization and changes in the microstructure.
- X-ray analysis identified the main phases as TiFe, $TiFeH_{0.94}$, and Ti_2FeH_x after activation. Considering the volume expansion of the Ti_2Fe phase upon hydrogenation, the resulting stoichiometry is approximately Ti_2FeH_3.

Author Contributions: Conceptualization, J.H and C.S.; validation, S.H. and J.H.; formal analysis, S.H.; investigation, S.H.; writing—original draft preparation, S.H.; writing—review and editing, S.H., C.S., and J.H.; supervision, J.H.; project administration, J.H and C.S. All authors have read and agreed to the published version of the manuscript.

Funding: This research was funded by GKN Hoeganaes Innovation Centre and Advanced Materials and MITACS.

Data Availability Statement: The original contributions presented in this study are included in the article. Further inquiries can be directed to the corresponding author.

Acknowledgments: Seyedehfaranak Hosseinigourajoubi acknowledges GKN Hoeganaes Innovation Centre and Advanced Materials and MITACS for a fellowship.

Conflicts of Interest: Author Chris Schade was employed by GKN Hoeganaes Innovation Centre & Advanced Materials. The remaining authors declare that the research was conducted in the absence of any commercial or financial relationships that could be construed as a potential conflict of interest. Besides, the authors declare that this study received funding from GKN Hoeganaes Innovation Centre and Advanced Materials. The funder was not involved in the study design, collection, analysis, interpretation of data, the writing of this article or the decision to submit it for publication.

References

1. Greene, D.L.; Ogden, J.M.; Lin, Z. Challenges in the designing, planning and deployment of hydrogen refueling infrastructure for fuel cell electric vehicles. *eTransportation* **2020**, *6*, 100086. [CrossRef]
2. Bosu, S.; Rajamohan, N. Recent advancements in hydrogen storage—Comparative review on methods, operating conditions and challenges. *Int. J. Hydrog. Energy* **2024**, *52*, 352–370. [CrossRef]
3. Edalati, K.; Matsuo, M.; Emami, H.; Itano, S.; Alhamidi, A.; Staykov, A.; Smith, D.J.; Orimo, S.-i.; Akiba, E.; Horita, Z. Impact of severe plastic deformation on microstructure and hydrogen storage of titanium-iron-manganese intermetallics. *Scr. Mater.* **2016**, *124*, 108–111. [CrossRef]
4. Liu, H.; Zhang, J.; Sun, P.; Zhou, C.; Liu, Y.; Fang, Z.Z. An overview of TiFe alloys for hydrogen storage: Structure, processes, properties, and applications. *J. Energy Storage* **2023**, *68*, 107772. [CrossRef]
5. Dematteis, E.; Berti, N.; Cuevas, F.; Latroche, M.; Baricco, M. Substitutional effects in TiFe for hydrogen storage: A comprehensive review. *Mater. Adv.* **2021**, *2*, 2524–2560. [CrossRef]

6. Dematteis, E.M.; Dreistadt, D.M.; Capurso, G.; Jepsen, J.; Cuevas, F.; Latroche, M. Fundamental hydrogen storage properties of TiFe-alloy with partial substitution of Fe by Ti and Mn. *J. Alloys Compd.* **2021**, *874*, 159925. [CrossRef]
7. Reilly, J.J.; Wiswall, R.H. Formation and properties of iron titanium hydride. *Inorg. Chem.* **1974**, *13*, 218–222. [CrossRef]
8. Zhu, H.Y.; Wu, J.; Wang, Q.D. Reactivation behaviour of TiFe hydride. *J. Alloys Compd.* **1994**, *215*, 91–95. [CrossRef]
9. Lee, S.M.; Perng, T.P. Microstructural correlations with the hydrogenation kinetics of FeTi1+*ξ* alloys. *J. Alloys Compd.* **1991**, *177*, 107–118. [CrossRef]
10. Schober, T.; Westlake, D.G. The activation of FeTi for hydrogen storage: A different view. *Scr. Metall.* **1981**, *15*, 913–918. [CrossRef]
11. Padhee, S.P.; Roy, A.; Pati, S. Role of Mn-substitution towards the enhanced hydrogen storage performance in FeTi. *Int. J. Hydrog. Energy* **2022**, *47*, 9357–9371. [CrossRef]
12. Miller, H.L.; Murray, J.; Laury, E.; Reinhardt, J.; Goudy, A.J. The hydriding and dehydriding kinetics of FeTi and Fe0.9TiMn0.1. *J. Alloys Compd.* **1995**, *231*, 670–674. [CrossRef]
13. Li, C.; Gao, X.; Liu, B.; Wei, X.; Zhang, W.; Lan, Y.; Wang, H.; Yuan, Z. Effects of Zr doping on activation capability and hydrogen storage performances of TiFe-based alloy. *Int. J. Hydrog. Energy* **2023**, *48*, 2256–2270. [CrossRef]
14. Lv, P.; Liu, Z.; Dixit, V. Improved hydrogen storage properties of TiFe alloy by doping (Zr + 2V) additive and using mechanical deformation. *Int. J. Hydrog. Energy* **2019**, *44*, 27843–27852. [CrossRef]
15. Chen, Z.; Guo, F.; Sunamoto, R.; Yin, C.; Miyaoka, H.; Ichikawa, T. Anti-oxidation effect of chromium addition for TiFe hydrogen storage alloys. *J. Alloys Compd.* **2024**, *1008*, 176634. [CrossRef]
16. Kumar, S.; Tiwari, G.P.; Sonak, S.; Jain, U.; Krishnamurthy, N. High performance FeTi—3.1 mass % V alloy for on board hydrogen storage solution. *Energy* **2014**, *75*, 520–524. [CrossRef]
17. Guéguen, A.; Latroche, M. Influence of the addition of vanadium on the hydrogenation properties of the compounds TiFe0.9Vx and TiFe0.8Mn0.1Vx (x = 0, 0.05 and 0.1). *J. Alloys Compd.* **2011**, *509*, 5562–5566. [CrossRef]
18. Han, Z.; Yuan, Z.; Zhai, T.; Feng, D.; Sun, H.; Zhang, Y. Effect of yttrium content on microstructure and hydrogen storage properties of TiFe-based alloy. *Int. J. Hydrog. Energy* **2023**, *48*, 676–695. [CrossRef]
19. Li, C.; Lan, Y.; Wei, X.; Zhang, W.; Liu, B.; Gao, X.; Yuan, Z. Improvement of hydrogen absorption and desorption properties of TiFe-based alloys by adding yttrium. *J. Alloys Compd.* **2022**, *927*, 166992. [CrossRef]
20. Ulate-Kolitsky, E.; Tougas, B.; Huot, J. First Hydrogenation of TiFe with Addition of 20 wt.% Ti. *Hydrogen* **2022**, *3*, 379–388. [CrossRef]
21. Ulate-Kolitsky, E.; Tougas, B.; Neumann, B.; Schade, C.; Huot, J. First hydrogenation of mechanically processed TiFe-based alloy synthesized by gas atomization. *Int. J. Hydrog. Energy* **2021**, *46*, 7381–7389. [CrossRef]
22. Patel, A.K.; Siemiaszko, D.; Dworecka-Wójcik, J.; Polański, M. Just shake or stir. About the simplest solution for the activation and hydrogenation of an FeTi hydrogen storage alloy. *Int. J. Hydrog. Energy* **2022**, *47*, 5361–5371. [CrossRef]
23. Edalati, K.; Matsuda, J.; Yanagida, A.; Akiba, E.; Horita, Z. Activation of TiFe for hydrogen storage by plastic deformation using groove rolling and high-pressure torsion: Similarities and differences. *Int. J. Hydrog. Energy* **2014**, *39*, 15589–15594. [CrossRef]
24. Patel, A.K.; Duguay, A.; Tougas, B.; Schade, C.; Sharma, P.; Huot, J. Microstructure and first hydrogenation properties of TiFe alloy with Zr and Mn as additives. *Int. J. Hydrog. Energy* **2020**, *45*, 787–797. [CrossRef]
25. Neikov, O.D. Chapter 4—Atomization and Granulation. In *Handbook of Non-Ferrous Metal Powders*, 2nd ed.; Neikov, O.D., Naboychenko, S.S., Yefimov, N.A., Eds.; Elsevier: Oxford, UK, 2019; pp. 125–185.
26. Abe, M.; Kuji, T. Hydrogen absorption of TiFe alloy synthesized by ball milling and post-annealing. *J. Alloys Compd.* **2007**, *446–447*, 200–203. [CrossRef]
27. Lee, S.M.; Perng, T.P. Effect of the second phase on the initiation of hydrogenation of TiFe1−xMx (M = Cr,Mn) alloys. *Int. J. Hydrog. Energy* **1994**, *19*, 259–263. [CrossRef]
28. Evans, J.S.O. Advanced Input Files & Parametric Quantitative Analysis Using Topas. *Mater. Sci. Forum* **2010**, *651*, 1–9. [CrossRef]
29. Okamoto, H.; Schlesinger, M.E.; Mueller, E.M. *Alloy Phase Diagrams;* ASM International: Detroit, MI, USA, 2016. [CrossRef]
30. Dong, C.; Hei, Z.K.; Wang, L.B.; Song, Q.H.; Wu, Y.K.; Kuo, K.H. A new icosahedral quasicrystal in rapidly solidified $FeTi_2$. *Scr. Metall.* **1986**, *20*, 1155–1158. [CrossRef]
31. Fruchart, D.; Commandré, M.; Sauvage, D.; Rouault, A.; Tellgren, R. Structural and activation process studies of FeTi-like hydride compounds. *J. Less Common Met.* **1980**, *74*, 55–63. [CrossRef]
32. Jung, J.Y.; Lee, Y.-S.; Suh, J.-Y.; Huh, J.-Y.; Cho, Y.W. Tailoring the equilibrium hydrogen pressure of TiFe via vanadium substitution. *J. Alloys Compd.* **2021**, *854*, 157263. [CrossRef]
33. Manna, J.; Tougas, B.; Huot, J. Mechanical activation of air exposed TiFe + 4 wt% Zr alloy for hydrogenation by cold rolling and ball milling. *Int. J. Hydrog. Energy* **2018**, *43*, 20795–20800. [CrossRef]
34. Emami, H.; Edalati, K.; Matsuda, J.; Akiba, E.; Horita, Z. Hydrogen storage performance of TiFe after processing by ball milling. *Acta Mater.* **2015**, *88*, 190–195. [CrossRef]
35. Lv, P.; Guzik, M.N.; Sartori, S.; Huot, J. Effect of ball milling and cryomilling on the microstructure and first hydrogenation properties of TiFe + 4wt.% Zr alloy. *J. Mater. Res. Technol.* **2019**, *8*, 1828–1834. [CrossRef]

36. Reidinger, F.; Lynch, J.F.; Reilly, J.J. An X-ray diffraction examination of the FeTi-H2 system. *J. Phys. F Met. Phys.* **1982**, *12*, L49. [CrossRef]
37. Kirchheim, R.; Pundt, A. 25—Hydrogen in Metals. In *Physical Metallurgy*, 5th ed.; Laughlin, D.E., Hono, K., Eds.; Elsevier: Oxford, UK, 2014; pp. 2597–2705.

Article 3

inorganics

MDPI

Article

Activation Energy and Kinetics of First Hydrogenation in $Ti_{48.8}Fe_{46.0}Mn_{5.2}$ Alloy Produced by Gas Atomization

Seyedehfaranak Hosseinigourajoubi [1], Chris Schade [2] and Jacques Huot [1,*]

[1] Hydrogen Research Institute, Université du Québec à Trois-Rivières, Trois-Rivières, QC G9A5H7, Canada
[2] GKN Hoeganaes Innovation Centre & Advanced Materials, 1001 Taylors Lane, Cinnaminson, NJ 08077, USA
* Correspondence: jacques.huot@uqtr.ca; Tel.: +1-819-376-5011 (ext. 3576); Fax: +1-819-376-5164

Abstract

The first hydrogenation behavior of the gas atomized $Ti_{48.8}Fe_{46.0}Mn_{5.2}$ alloy was systemically investigated. The as-received powder showed no hydrogen absorption due to the long air exposure before the hydrogenation tests. To overcome this, 5 passes of cold rolling were employed as an activation strategy. Cold rolling introduced cracks and defects that facilitated hydrogen diffusion, enabling the alloy to successfully absorb hydrogen. The influences of temperature, constant driving force, and hydrogen pressure on the first hydrogenation were evaluated. The results indicated that the first hydrogenation follows an Arrhenius behavior ($k = Ae^{-\frac{Ea}{RT}}$), and average activation energy was calculated as 71 kJ/mol H_2. The pre-exponential factor (A) was found to be pressure-dependent, following the equation $A = A_0 (P/P_0)^{1.8}$, where $A_0 = 2.6 \times 10^6\ s^{-1}$.

Keywords: TiFe alloy; metal hydride; first hydrogenation; activation energy; Arrhenius mechanism

1. Introduction

Hydrogen, as an energy vector, offers a sustainable alternative to fossil fuels, addressing global challenges like climate change and rising energy demand [1]. Its high gravimetric energy density, significantly higher than that of conventional fuels, makes it an attractive option for many practical applications. However, developing efficient storage systems remains critical for the widespread usage of hydrogen [2–4].

Hydrogen is mainly stored in three primary forms: as a compressed gas, cryogenic liquid, or solid-state material. Compressed and liquid hydrogen storage face challenges such as high pressure, cryogenic temperature, and high costs. Solid-state storage in the form of metal hydrides could potentially provide safe storage with high volumetric density under relatively mild temperature and pressure conditions [2,5,6]. Solid-state storage involves the storage of hydrogen, either on the surface of solids through Van der Waals interactions or within solids, by forming chemical bonds with the metal atoms to form metal hydrides [7,8].

Among metal hydrides, TiFe-based alloys are promising materials for hydrogen storage due to their abundance, low cost, and good reversibility during hydrogen absorption and desorption [9–12]. The TiFe alloy is a well-known AB-type intermetallic compound capable of storing approximately 1.86 wt% of hydrogen, first reported by Reilly and Wiswall in 1974 [13].

A major limitation of TiFe alloys is the sluggish kinetics during the first hydrogenation. During air exposure, a surface oxide layer is naturally formed which acts as a barrier for

Academic Editor: Duncan H. Gregory

Received: 18 January 2026
Revised: 10 February 2026
Accepted: 13 February 2026
Published: 17 February 2026

hydrogen diffusion into the alloy. As a result, when TiFe alloy is exposed to hydrogen, a certain time is needed for penetration of hydrogen into the alloy and reaction with metal atoms. This period is known as the incubation time. Once this barrier is overcome, the hydrogenation can proceed [14,15].

To break the oxide layer, and start the hydrogen absorption reaction, Reilly and Wiswall used the method of heating the alloy to 400 °C, followed by cooling and applying a high hydrogen pressure of approximately 60 bars [13]. This process had to be repeated several times until the alloy could be fully hydrided. This method has since been widely used in numerous studies on TiFe alloys [16,17].

Adding transition elements such as Zr [18,19], Mn [20–22], Cr [10,20], and Y [23] can significantly improve the first hydrogenation kinetics by promoting the formation of secondary phases that facilitate hydrogen diffusion. Mechanical deformation techniques like ball milling [24,25], cold rolling [26,27], and high-pressure torsion [28] are also beneficial for improving first hydrogenation kinetics by creating grain boundaries and cracks, which act as pathways for hydrogen to penetrate the oxide layer. Furthermore, several studies have shown that powder processing methods like gas atomization could enhance the first hydrogenation properties of TiFe-based alloys by producing a finer microstructure [27,29,30]. Ulate-Kolitsky et al. compared alloys synthesized by gas atomization and induction melting, concluding that gas atomization resulted in a much finer microstructure and a TiFe matrix with a more refined distribution of secondary phases [27].

Previous research has indicated that the hydrogen absorption process generally follows an Arrhenius-type mechanism, and there have been attempts to calculate the activation energy of metal hydride formation in these alloys [22,31–34]. Bowman and Tadlock [33] investigated the hydrogen diffusion rate in TiFeH phase using nuclear magnetic resonance (NMR) techniques, and the temperature dependence of the proton relaxation rate suggested Arrhenius behavior, leading to the calculation of activation energy as 31.8 kJ/mol. Chung and Lee [34] demonstrated that hydrogen absorption kinetics of TiFe alloys improve with partial substitution of Mn and Ni for Fe. They found that the hydriding rate depends on the difference between the applied pressure and the equilibrium pressure, and from Arrhenius plots of the rate constants versus 1/T, they calculated the activation energies to be 33.5 kJ/mol for TiFe, 32.6 kJ/mol for $TiFe_{0.85}Mn_{0.15}$, and 31.8 kJ/mol for $TiFe_{0.9}Ni_{0.1}$.

The above-mentioned studies calculated the activation energy associated with hydrogen absorption after the alloy had already been hydrogenated, and the incubation stage caused by the surface oxide layer was no longer present. However, the first hydrogenation, where the oxide is broken, is critical as it can significantly influence the cost and efficiency of metal hydride formation. In the present study, we systematically investigate the first hydrogenation behavior of a TiFe-based alloy ($Ti_{48.8}Fe_{46.0}Mn_{5.2}$) produced by gas atomization. This composition was selected because Mn substitution could promote the formation of secondary phases that facilitate hydrogen diffusion [20–22]. Unlike previous works, which focused only on alloys that were already subjected to a few hydrogenation/dehydrogenation steps, this study focuses specifically on the first hydrogenation. The effects of temperature, constant driving force, and hydrogen pressure on the incubation time of the first hydrogenation were investigated. To our knowledge, this is the first systematic investigation of how working conditions influence the first hydrogenation of a TiFe-based alloy.

2. Results and Discussion

The microstructure, crystal structure, and first hydrogenation of $Ti_{48.8}Fe_{46.0}Mn_{5.2}$ alloy were reported in our earlier paper [35]. It was found that the microstructure consisted of a

main TiFe matrix and a filamentous Ti_2Fe-like phase. The main TiFe phase exhibited a BCC crystal structure with a lattice parameter of 2.9828 ± 0.0004 Å.

As reported in our previous study, the as-received atomized $Ti_{48.8}Fe_{46.0}Mn_{5.2}$ alloy was unable to absorb hydrogen under two different test conditions: (i) at room temperature under 20 bars H_2 pressure, and (ii) at 363 K under 45 bars H_2. To activate the alloy, it was subjected to five passes of cold rolling (5CR) in the air. After cold rolling, the obtained flakes and powders were manually crushed in air into powder using a hardened steel mortar and pestle. The resulting powder had a particle size distribution ranging from 45 to 212 µm. This obtained powder was subsequently used for the hydrogenation tests. The 5CR alloy successfully absorbed hydrogen under both above-mentioned testing conditions. Given that cold rolling in air successfully activated the material, and considering the industrial collaboration of the research and the practical convenience of cold rolling in air, all further cold rolling steps were conducted in air.

Figure 1 presents the morphology of the as-received and cold-rolled powders. A reduction in particle size is evident after cold rolling, along with the formation of cracks on the powder surfaces. As shown in Figure 1a, a combination of spherical and non-spherical particles was observed in the atomized powder. The spherical particles have a size distribution from 20 µm up to 300 µm, while non-spherical particles fall within the 100–400 µm range. Figure 1c shows that after five passes of cold rolling, the average particle size decreased significantly. Most particles were reduced to below 20 µm, although some larger particles (~100 µm) remained. In addition to the decrease in particle size, cold rolling introduced numerous cracks and surface defects which are clearly visible under the higher magnification of Figure 1d. These morphological changes, including particle size reduction and the formation of cracks and defects, enhance hydrogen diffusion and facilitate hydrogen absorption. This effect has been observed in other alloys such as TiFe [26,27], $LaNi_5$ [36], and Mg [37,38].

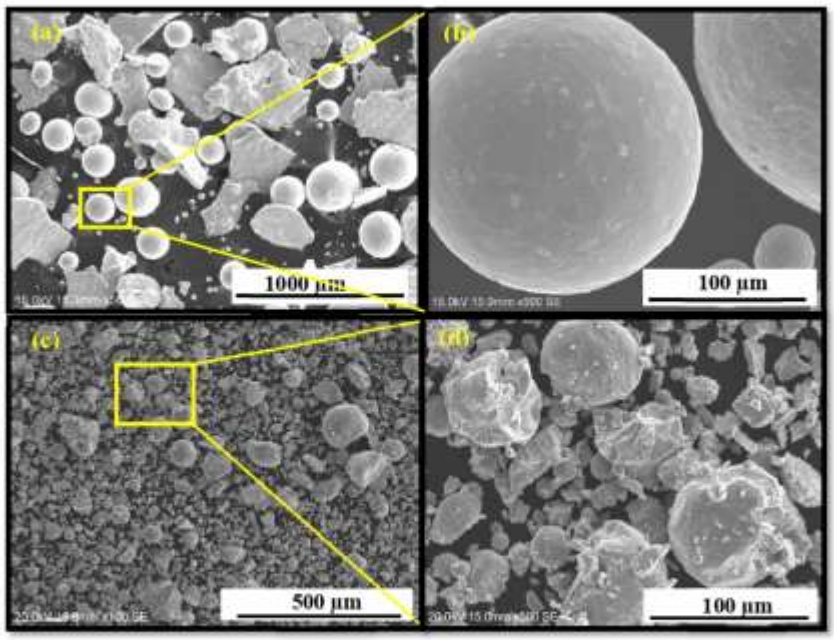

Figure 1. Morphology of gas atomized $Ti_{48.8}Fe_{46.0}Mn_{5.2}$ (**a**,**b**), and after 5 cold rolling passes (**c**,**d**).

https://doi.org/10.3390/inorganics14020062

After finding that five passes of cold rolling effectively regenerate the $Ti_{48.8}Fe_{46.0}Mn_{5.2}$ alloy for hydrogen absorption, the next step was to evaluate the first hydrogenation parameters systematically. In the following sections, we investigate the effects of temperature, constant driving force, and hydrogen pressure on the first hydrogenation behavior. To prepare the alloy for hydrogen absorption, all kinetic experiments were conducted on samples subjected to 5 cold rolling passes prior to each test.

2.1. Effect of Temperature on First Hydrogenation of $Ti_{48.8}Fe_{46.0}Mn_{5.2}$-5CR

The effect of temperature on the first hydrogenation was investigated by measuring the incubation time at 298 K, 308 K, 318 K, and 328 K under a hydrogen pressure of 40 bars. Figure 2 shows the first hydrogenation kinetics of the of $Ti_{48.8}Fe_{46.0}Mn_{5.2}$-5CR alloy at different temperatures under a hydrogen pressure of 40 bars. We see that the incubation time decreases with increasing temperature from approximately 3000 s at 298 K to 330 s at 328 K.

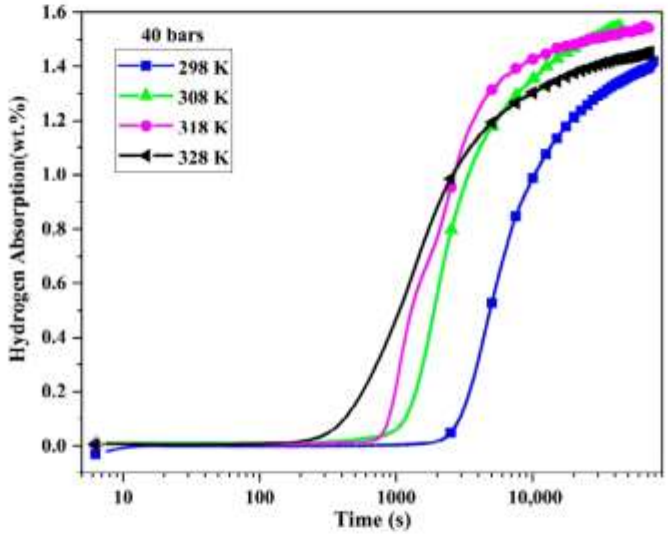

Figure 2. First hydrogenation curves of $Ti_{48.8}Fe_{46.0}Mn_{5.2}$-5CR alloy at 298 K, 308 K, 318 K, and 328 K under a hydrogen pressure of 40 bars.

The fact that incubation time varies with temperature indicates that the process may follow an Arrhenius-type behavior. The Arrhenius equation describes the relationship between the rate of a chemical reaction and temperature, and is expressed as

$$k = Ae^{-\frac{E_a}{RT}} \quad (1)$$

where

k is the rate constant of the chemical reaction,
A is the pre-exponential factor or Arrhenius factor, a constant related to the frequency of collisions of reacting molecules (s^{-1}),
E_a is the activation energy for the reaction (J/mol),
R is the universal gas constant (8.314 J/(mol K)),
T is the absolute temperature (K).

Since incubation time (t) is inversely proportional to the rate constant:

$$t \sim \frac{1}{k} \tag{2}$$

Then, Equation (1) could be written as

$$\ln t = -\ln A + \frac{E_a}{RT} \tag{3}$$

In Figure 3, ln t is plotted as a function of 1000/T. From the slope of the fitted line, the activation energy is calculated to be E_a = 69 ± 1 kJ/mol H_2. Additionally, from the intercept, A is 2.7 × 10^8 s^{-1} with a range from 1.6 × 10^8 to 4.2 × 10^8 s^{-1}.

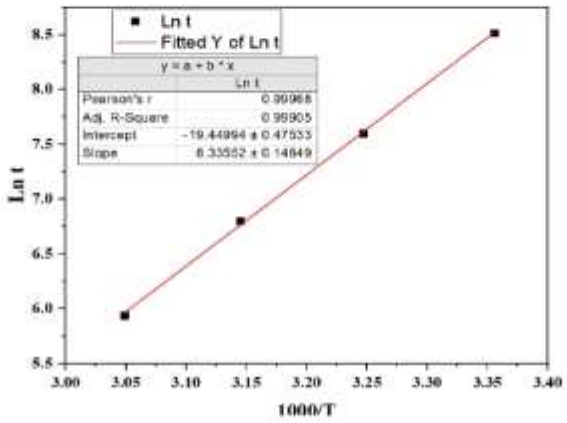

Figure 3. Plot of ln t (incubation time) as a function of 1000/T (T: temperature) for activation of $Ti_{48.8}Fe_{46.0}Mn_{5.2}$-5CR at 298 K, 308 K, 318 K and 328 K under hydrogen pressure of 40 bars.

2.2. First Hydrogenation Behavior Under a Constant Driving Force

In hydrogen absorption reactions, the difference between the applied pressure and the hydrogenation equilibrium pressure is defined as the driving force, which controls the reaction rate. Driving force can be characterized using the Rudman's expression [39]:

$$c = T\left(1 - \sqrt{P/P_e}\right) \tag{4}$$

where c is the driving force, T is the temperature, P is the applied pressure, and P_e is the equilibrium pressure of the reaction. For the calculation, we used the literature thermodynamic values of the closely related composition $Ti_1Fe_{0.9}Mn_{0.1}$ [40].

A higher C value indicates a stronger driving force for the hydrogen absorption reaction. In these experiments, the driving force was maintained constant as C = 175, and the hydrogen absorption tests were carried out at 298, 308, 318, and 328 K. The corresponding pressures were calculated as 15, 20, 27 and 35 bars, respectively. The results are shown in Figure 4.

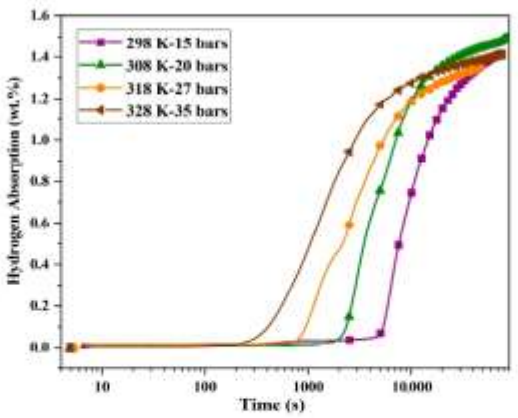

Figure 4. Activation curves under constant driving force for $Ti_{48.8}Fe_{46.0}Mn_{5.2}$-5CR alloy.

The incubation time is plotted as a function of 1000/T in Figure 5 to determine whether the Arrhenius mechanism is still applicable. The linear fit demonstrates that the incubation time still obeys an Arrhenius law. The fitted slope yields an activation energy of $E_a = 72 \pm 4$ kJ/mol H_2. The intercept reveals the pre-exponential factor (A) as 1.3×10^9 s^{-1}, with a range from 3.2×10^8 to 5.8×10^9 s^{-1}.

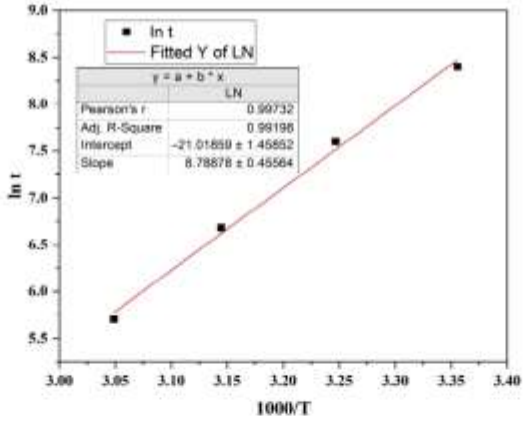

Figure 5. Plot of ln t (incubation time) as a function of 1000/T (T: temperature) for activation under constant driving force.

The activation energies obtained under constant pressure and constant driving force conditions overlap and fall within the same range. This observation suggests that the activation energy is an intrinsic property of the alloy and essentially constant across different testing conditions.

Regarding the pre-exponential factor (A), it represents the number of interactions per second, and obviously, this is pressure-dependent. For practical applications, it is important to have the pressure dependence of this factor because it will give the range of pressures required to have a reasonable incubation time. In a previous investigation on $LaNi_5$ alloy, it was also reported that the pre-exponential factor is pressure-dependent [41].

https://doi.org/10.3390/inorganics14020062

The dependency of A on pressure can be expressed as

$$A = A_0(P/P_0)^x \quad (5)$$

Here, A_0 and x are constants, P represents the applied hydrogen pressure, and $P_0 = 1$ bar.

2.3. Effect of Pressure on First Hydrogenation Behavior

To study the effect of pressure on the pre-exponential factor, the first hydrogenation was performed at 298 K under 20, 30, 40, and 50 bars of hydrogen pressure. The hydrogenation curves are shown in Figure 6. With increasing pressure, the incubation time decreased. The variation of ln t as a function of ln P/P_0 is shown in Figure 7.

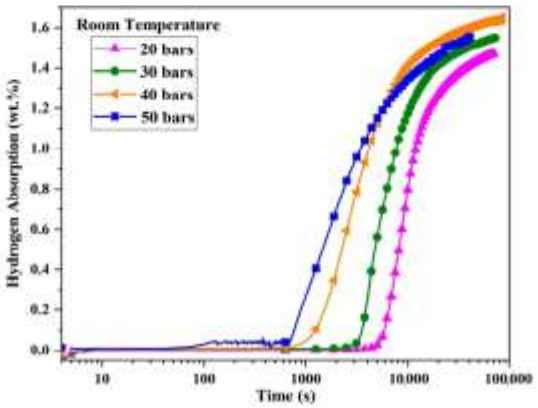

Figure 6. First hydrogenation curves at room temperature under 20, 30, 40, and 50 bars of hydrogen pressure.

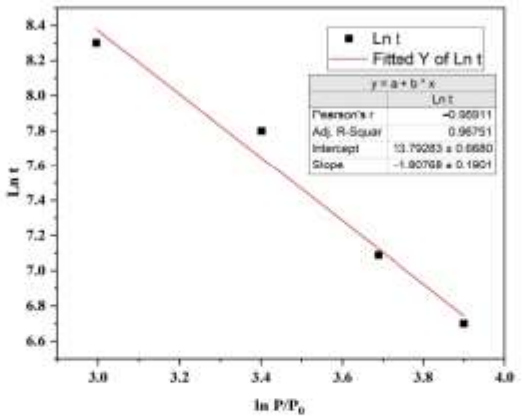

Figure 7. Plot of ln t as a function of ln P/P_0, where t is the incubation time and P is the pressure.

Considering Equation (5), Equation (3) can be written as:

$$\ln t = \frac{E_a}{RT} - \ln A_0 - x\ln(P/P_0) \quad (6)$$

https://doi.org/10.3390/inorganics14020062

From the fitted slope of Figure 7, x = 1.8 ± 0.2, therefore, the dependence of pre-exponential factor (A) to applied pressure can be expressed as:

$$A = A_0(P/P_0)^{1.8} \quad (7)$$

In summary, the activation energy for the first hydrogen absorption, calculated under both constant pressure and constant driving force conditions, remains essentially constant within the experimental error, with an average value of 71 kJ/mol. The pre-exponential factor (A) shows the dependence of the incubation time on the pressure, which follows the relationship $A = A_0(P/P_0)^{1.8}$, where $A_0 = 2.6 \times 10^6\ s^{-1}$.

The activation energy reported in the literature has been on samples that were subjected to several hydrogenation/dehydrogenation cycles. Bowman and Tadlock [33] prepared TiFeH by performing several hydriding–dehydriding cycles between room temperature and 400 °C. By using nuclear magnetic resonance (NMR) techniques, they observed that the proton relaxation rate exhibited Arrhenius-type temperature dependence. From the slope of their plot, they determined an activation energy of 31.8 kJ/mol, which is less than the activation energy found in our study. The activation energy reported by Bowman and Tadlock refers to the hydrogenation cycles after the material had been fully activated. Our study specifically focuses on the first hydrogenation process, which includes both the activation energy for hydrogen absorption and the additional activation energy required for the incubation process. Furthermore, Bowman and Tadlock's study [33] measured the activation energy of TiFe alloys without elemental substitution, whereas manganese (Mn) was partially substituted for iron (Fe) in the present study.

On the other hand, several studies have shown that Mn substitution facilitates hydrogen absorption kinetics but does not significantly affect the activation energy [22,34]. Chung and Lee [34] prepared TiFe and $TiFe_{0.85}Mn_{0.15}$ alloys by arc melting and activated them through heat treatment at 400 °C under hydrogen atmosphere, followed by hydrogen absorption–desorption cycles at room temperature. They found that, for both alloys, the hydrogenation rate was proportional to the difference between the applied pressure and the equilibrium pressure, and it also followed an Arrhenius relationship. From their analysis, they measured activation energies of 33.5 kJ/mol for TiFe and 32.6 kJ/mol for $TiFe_{0.85}Mn_{0.15}$. Similarly, Padhee et al. [22] employed Density Functional Theory (DFT) calculations to estimate the activation energy of TiFe and $TiFe_{0.875}Mn_{0.125}$, reporting values of 32.6 kJ/mol and 33.3 kJ/mol, respectively. These results also show that Mn substitution causes minimal changes in the activation energy.

Zeaiter et al. [42] reported an activation energy of 19.43 ± 2.52 kJ/mol for $TiFe_{0.9}Mn_{0.1}$ after 12 absorption/desorption cycles, which is significantly lower than most values reported in the literature. This low activation energy may be attributed to the thermochemical treatment applied prior to the activation process, which involved heating the sample at 400 °C under 32 bar of hydrogen for 24 h in a reactor cell. Compared with the as-received powder, which exhibited an incubation time of approximately 6000 min, the thermochemically treated powder showed a much shorter incubation time of 1595 min. Unfortunately, the activation energy of the as-received powder was not reported, so a direct comparison between the two states is not possible.

Bakulin et al. [43] calculated an activation energy of 59 kJ/mol for TiFe using density functional theory (DFT). They reported that the addition of dopant elements slightly reduces the activation energy; for example, the substitution of 5 at.% Mn decreased the activation energy to 58 kJ/mol.

Overall, the literature consistently reports activation energies lower than those in our study. The reason is that they evaluated the activation energy of the hydrogen absorption reaction after the first hydrogenation had occurred, without considering incubation time in

first hydrogen absorption cycle. In contrast, our study measured the activation energy for both the incubation stage and hydrogen absorption. It is thus reasonable that the activation energy measured here is bigger than the activation energy reported in the literature, as it includes the activation energy needed to break the oxide layer on the particle's surface, plus the hydrogenation activation energy.

3. Materials and Methods

The gas-atomized alloy, with an atomic composition of 48.8 Ti, 46.0 Fe, and 5.2 Mn, was provided by GKN Hoeganaes Innovation Centre and Advanced Materials. Gas atomization was carried out by GKN under pure argon using a VIGA-type furnace equipped with a free-fall atomization ring set-up. Following synthesis, the powder was stored in the air.

The atomized powder was subjected to five cold rolling passes before hydrogenation. Cold rolling was performed vertically in the air using a modified Durston DRM 130 rolling mill (High Wycombe, Buckinghamshire, UK). The powder was inserted between two 316 stainless steel plates to prevent contamination of the powder by the rollers.

The powder morphology before and after cold rolling was examined using a Hitachi SU1510 scanning electron microscope (SEM) (Hitachi High-Tech Canada, Toronto, ON, Canada).

The hydrogenation tests were carried out using a homemade Sievert's apparatus. The measurements were conducted under various pressures ranging from 15 bars to 50 bars at temperatures of 298 K, 308 K, 318 K, and 328 K. Each hydrogenation test was conducted on about one gram of fresh sample. The samples were evacuated for 15 min at room temperature prior to kinetic measurements.

4. Conclusions

In this study, the first hydrogenation behavior of $Ti_{48.8}Fe_{46.0}Mn_{5.2}$ alloy, synthesized via gas atomization, was investigated. It was found that the as-atomized alloy could not absorb hydrogen due to air exposure; however, after five passes of cold rolling in air, the alloy was successfully regenerated.

The effects of temperature, constant driving force, and hydrogen pressure on the first hydrogenation were studied. It was observed that increasing the temperature and pressure reduced the incubation time required for hydrogen absorption. Analysis of the kinetics data confirmed that the first hydrogenation follows an Arrhenius-type mechanism, with an average activation energy of 71 kJ/mol H_2. This value reflects the activation energy for both the incubation stage, associated with breaking the oxide layer, and the hydrogen absorption process, and is higher than the average activation energies reported in previous studies, which were determined after the alloys had already undergone the first hydrogenation.

The effect of pressure on the pre-exponential factor (A) was found to vary as $A = A_0 (P/P_0)^{1.8}$, where A_0 equals 2.6×10^6 s^{-1}. These findings provide important insights for optimizing the first hydrogenation of TiFe-based alloys for hydrogen storage applications.

Author Contributions: Conceptualization, S.H. and J.H.; validation, S.H. and J.H.; formal analysis, S.H.; investigation, S.H.; writing—original draft preparation, S.H.; writing—review and editing, S.H., C.S. and J.H.; supervision, J.H.; project administration, J.H. and C.S. All authors have read and agreed to the published version of the manuscript.

Funding: This research was funded by GKN Hoeganaes Innovation Centre and Advanced Materials and MITACS.

Data Availability Statement: The original contributions presented in this study are included in the article. Further inquiries can be directed to the corresponding author.

https://doi.org/10.3390/inorganics14020062

Acknowledgments: Seyedehfaranak Hosseinigourajoubi acknowledges GKN Hoeganaes Innovation Centre and Advanced Materials and MITACS for the fellowship.

Conflicts of Interest: The authors declare no conflicts of interest.

References

1. Lu, X.; Krutoff, A.-C.; Wappler, M.; Fischer, A. Key influencing factors on hydrogen storage and transportation costs: A systematic literature review. *Int. J. Hydrogen Energy* **2025**, *105*, 308–325. [CrossRef]
2. Bosu, S.; Rajamohan, N. Recent advancements in hydrogen storage-Comparative review on methods, operating conditions and challenges. *Int. J. Hydrogen Energy* **2024**, *52*, 352–370. [CrossRef]
3. Dincer, I. Renewable energy and sustainable development: A crucial review. *Renew. Sustain. Energy Rev.* **2000**, *4*, 157–175. [CrossRef]
4. Umar, A.A.; Hossain, M.M. Hydrogen storage via adsorption: A review of recent advances and challenges. *Fuel* **2025**, *387*, 134273. [CrossRef]
5. Von Colbe, J.B.; Ares, J.-R.; Barale, J.; Baricco, M.; Buckley, C.; Capurso, G.; Gallandat, N.; Grant, D.M.; Guzik, M.N.; Jacob, I. Application of hydrides in hydrogen storage and compression: Achievements, outlook and perspectives. *Int. J. Hydrogen Energy* **2019**, *44*, 7780–7808. [CrossRef]
6. Greene, D.L.; Ogden, J.M.; Lin, Z. Challenges in the designing, planning and deployment of hydrogen refueling infrastructure for fuel cell electric vehicles. *eTransportation* **2020**, *6*, 100086. [CrossRef]
7. Abe, J.O.; Popoola, A.P.I.; Ajenifuja, E.; Popoola, O.M. Hydrogen energy, economy and storage: Review and recommendation. *Int. J. Hydrogen Energy* **2019**, *44*, 15072–15086. [CrossRef]
8. Schlapbach, L. Technology: Hydrogen-fuelled vehicles. *Nature* **2009**, *460*, 809–811. [CrossRef]
9. Rachidi, S.; El Kassaoui, M.; Tahiri, N.; Mounkachi, O.; Ez-Zahraouy, H. Understanding degradation mechanisms and hydrogenation kinetics of intrinsic γ-$FeTiH_2$. *J. Energy Storage* **2024**, *104*, 114571. [CrossRef]
10. Chen, Z.; Guo, F.; Sunamoto, R.; Yin, C.; Miyaoka, H.; Ichikawa, T. Anti-oxidation effect of chromium addition for TiFe hydrogen storage alloys. *J. Alloys Compd.* **2024**, *1008*, 176634. [CrossRef]
11. Schober, T.; Westlake, D.G. The activation of FeTi for hydrogen storage: A different view. *Scr. Metall.* **1981**, *15*, 913–918. [CrossRef]
12. Lototsky, M.V.; Davids, M.W.; Fokin, V.N.; Fokina, E.E.; Tarasov, B.P. Hydrogen-Accumulating Materials Based on Titanium and Iron Alloys (Review). *Therm. Eng.* **2024**, *71*, 264–279. [CrossRef]
13. Reilly, J.J.; Wiswall, R.H. Formation and properties of iron titanium hydride. *Inorg. Chem.* **1974**, *13*, 218–222. [CrossRef]
14. Sartori, S.; Amati, M.; Gregoratti, L.; Jensen, E.H.; Kudriashova, N.; Huot, J. Study of Phase Composition in TiFe+ 4 wt.% Zr Alloys by Scanning Photoemission Microscopy. *Inorganics* **2023**, *11*, 26. [CrossRef]
15. Miller, H.I.; Murray, J.; Laury, E.; Reinhardt, J.; Goudy, A.J. The hydriding and dehydriding kinetics of FeTi and $Fe_{0.9}TiMn_{0.1}$. *J. Alloys Compd.* **1995**, *231*, 670–674. [CrossRef]
16. Zhu, H.; Wu, J.; Wang, Q. Reactivation behaviour of TiFe hydride. *J. Alloys Compd.* **1994**, *215*, 91–95. [CrossRef]
17. Liu, H.; Zhang, J.; Sun, P.; Zhou, C.; Liu, Y.; Fang, Z.Z. The mechanistic role of $Ti_4Fe_2O_1$-x phases in the activation of TiFe alloys for hydrogen storage. *Int. J. Hydrogen Energy* **2023**, *48*, 32011–32024. [CrossRef]
18. Li, C.; Gao, X.; Liu, B.; Wei, X.; Zhang, W.; Lan, Y.; Wang, H.; Yuan, Z. Effects of Zr doping on activation capability and hydrogen storage performances of TiFe-based alloy. *Int. J. Hydrogen Energy* **2023**, *48*, 2256–2270. [CrossRef]
19. Lv, P.; Liu, Z.; Dixit, V. Improved hydrogen storage properties of TiFe alloy by doping (Zr+2V) additive and using mechanical deformation. *Int. J. Hydrogen Energy* **2019**, *44*, 27843–27852. [CrossRef]
20. Park, K.B.; Ko, W.-S.; Fadonougbo, J.O.; Na, T.-W.; Im, H.-T.; Park, J.-Y.; Kang, J.-W.; Kang, H.-S.; Park, C.-S.; Park, H.-K. Effect of Fe substitution by Mn and Cr on first hydrogenation kinetics of air-exposed TiFe-based hydrogen storage alloy. *Mater. Charact.* **2021**, *178*, 111246. [CrossRef]
21. Dematteis, E.M.; Dreistadt, D.M.; Capurso, G.; Jepsen, J.; Cuevas, F.; Latroche, M. Fundamental hydrogen storage properties of TiFe-alloy with partial substitution of Fe by Ti and Mn. *J. Alloys Compd.* **2021**, *874*, 159925. [CrossRef]
22. Padhee, S.P.; Roy, A.; Pati, S. Role of Mn-substitution towards the enhanced hydrogen storage performance in FeTi. *Int. J. Hydrogen Energy* **2022**, *47*, 9357–9371. [CrossRef]
23. Han, Z.; Yuan, Z.; Zhai, T.; Feng, D.; Sun, H.; Zhang, Y. Effect of yttrium content on microstructure and hydrogen storage properties of TiFe-based alloy. *Int. J. Hydrogen Energy* **2023**, *48*, 676–695. [CrossRef]
24. Emami, H.; Edalati, K.; Matsuda, J.; Akiba, E.; Horita, Z. Hydrogen storage performance of TiFe after processing by ball milling. *Acta Mater.* **2015**, *88*, 190–195. [CrossRef]
25. Falcão, R.B.; Dammann, E.D.C.C.; Rocha, C.J.; Durazzo, M.; Ichikawa, R.U.; Martinez, L.G.; Botta, W.J.; Leal Neto, R.M. An alternative route to produce easily activated nanocrystalline TiFe powder. *Int. J. Hydrogen Energy* **2018**, *43*, 16107–16116. [CrossRef]

26. Vega, L.; Leiva, D.; Neto, R.L.; Silva, W.; Silva, R.; Ishikawa, T.; Kiminami, C.; Botta, W. Mechanical activation of TiFe for hydrogen storage by cold rolling under inert atmosphere. *Int. J. Hydrogen Energy* **2018**, *43*, 2913–2918. [CrossRef]
27. Ulate-Kolitsky, E.; Tougas, B.; Neumann, B.; Schade, C.; Huot, J. First hydrogenation of mechanically processed TiFe-based alloy synthesized by gas atomization. *Int. J. Hydrogen Energy* **2021**, *46*, 7381–7389. [CrossRef]
28. Edalati, K.; Matsuda, J.; Iwaoka, H.; Toh, S.; Akiba, E.; Horita, Z. High-pressure torsion of TiFe intermetallics for activation of hydrogen storage at room temperature with heterogeneous nanostructure. *Int. J. Hydrogen Energy* **2013**, *38*, 4622–4627. [CrossRef]
29. Park, K.B.; Fadonougbo, J.O.; Na, T.-W.; Lee, T.W.; Kim, M.; Lee, D.H.; Kwon, H.G.; Park, C.-S.; Do Kim, Y.; Park, H.-K. On the first hydrogenation kinetics and mechanisms of a $TiFe_{0.85}Cr_{0.15}$ alloy produced by gas atomization. *Mater. Charact.* **2022**, *192*, 112188. [CrossRef]
30. Lee, D.H.; Kwon, H.G.; Park, K.B.; Im, H.-T.; Kwak, R.H.; Sohn, S.S.; Park, H.-K.; Fadonougbo, J.O. Phase formation behavior and hydrogen sorption characteristics of $TiFe_{0.8}Mn_{0.2}$ powders prepared by gas atomization. *Int. J. Hydrogen Energy* **2023**, *48*, 27697–27709. [CrossRef]
31. Nong, Z.-S.; Zhu, J.-C.; Yang, X.-W.; Cao, Y.; Lai, Z.-H.; Liu, Y. First-principles study of hydrogen storage and diffusion in B2 FeTi alloy. *Comput. Mater. Sci.* **2014**, *81*, 517–523. [CrossRef]
32. Lebsanft, E.; Richter, D.; Topler, J. Investigation of the hydrogen diffusion in FeTiHx by means of quasielastic neutron scattering. *J. Phys. F Met. Phys.* **1979**, *9*, 1057. [CrossRef]
33. Bowman, R.C., Jr.; Tadlock, W.E. Hydrogen diffusion in β-phase titanium iron hydride. *Solid State Commun.* **1979**, *32*, 313–318. [CrossRef]
34. Chung, H.; Lee, J.-Y. Effect of partial substitution of Mn and Ni for Fe in FeTi on hydriding kinetics. *Int. J. Hydrogen Energy* **1986**, *11*, 335–339. [CrossRef]
35. Hosseinigourajoubi, S.; Schade, C.; Huot, J. The Effect of Annealing on the First Hydrogenation Behavior of Atomized $Ti_{48.8}Fe_{46.0}Mn_{5.2}$ Alloy. *Metals* **2025**, *15*, 251. [CrossRef]
36. Liu, Y.; Chabane, D.; Elkedim, O. Optimization of $LaNi_5$ hydrogen storage properties by the combination of mechanical alloying and element substitution. *Int. J. Hydrogen Energy* **2024**, *53*, 394–402. [CrossRef]
37. Lima, G.F.; Triques, M.R.M.; Kiminami, C.S.; Botta, W.J.; Jorge, A.M. Hydrogen storage properties of pure Mg after the combined processes of ECAP and cold-rolling. *J. Alloys Compd.* **2014**, *586*, S405–S408. [CrossRef]
38. Floriano, R.; Leiva, D.R.; Carvalho, J.A.; Ishikawa, T.T.; Botta, W.J. Cold rolling under inert atmosphere: A powerful tool for Mg activation. *Int. J. Hydrogen Energy* **2014**, *39*, 4959–4965. [CrossRef]
39. Rudman, P. Hydrogen-diffusion-rate-limited hydriding and dehydriding kinetics. *J. Appl. Phys.* **1979**, *50*, 7195–7199. [CrossRef]
40. Huston, E.L.; Sandrock, G.D. Engineering properties of metal hydrides. *J. Less Common Met.* **1980**, *74*, 435–443. [CrossRef]
41. Sleiman, S.; Shahgaldi, S.; Huot, J. Investigation of the First Hydrogenation of $LaNi_5$. *Reactions* **2024**, *5*, 419–428. [CrossRef]
42. Zeaiter, A.; Nardin, P.; Pour Yazdi, M.A.; Billard, A. Outstanding shortening of the activation process stage for a TiFe-based hydrogen storage alloy. *Mater. Res. Bull.* **2019**, *112*, 132–141. [CrossRef]
43. Bakulin, A.V.; Kulkov, A.S.; Kulkova, S.E. Impurity influence on the hydrogen diffusivity in B2–TiFe. *Int. J. Hydrogen Energy* **2023**, *48*, 232–242. [CrossRef]

https://doi.org/10.3390/inorganics14020062